

# Accumulation of macrophages in adipose tissue

5 Chronic, low grade adipose tissue inflammation contributes to the development of metabolic complications in obesity. The underlying mechanisms are not fully understood but involve the accumulation of pro-inflammatory macrophages in the adipose tissue. Now, a new study shows that inflammatory signalling in a subset of perivascular mesenchymal cells drives this increase of pro-inflammatory macrophages in the adipose tissue during obesity.

10 “We previously utilized single-cell RNA sequencing to explore the cellular heterogeneity of mesenchymal cells residing in the adipose tissue vasculature,” explains Rana Gupta, corresponding author of the study. “We identified a population of ... cells [that] are uniquely capable of expressing ... pro-inflammatory cytokines in response to pro-inflammatory signals.”

15 To explore the pathophysiologic role of these cells, the researchers induced the genetic inactivation of inflammatory signalling in perivascular mesenchymal cells of obese mice. They observed that blocking inflammatory signalling did not affect body weight, but attenuated the accumulation of pro-inflammatory adipose tissue macrophages, and improved glucose tolerance as well as insulin sensitivity. “Perivascular mesenchymal cells of adipose tissue are critical ‘gatekeepers’ of macrophage accumulation in obesity,” says Gupta. “[To date] these cells have been largely overlooked.”

20 The team also report that the transcriptional regulator ZFP423 controls the inflammatory response of perivascular mesenchymal cells. Using in vitro studies and mouse genetic models they determined that ZFP423 modulates the composition of the NF- $\kappa$ B complex to suppresses NF- $\kappa$ B transcriptional activity, and that expression of ZFP423 in perivascular mesenchymal cells attenuates metabolic inflammation.

25 Going forward the authors plan to further research the signalling mechanisms that lead to perivascular mesenchymal cell activation in obesity. “The next step in this work is to identify the initial triggers of [perivascular mesenchymal cell activation in obesity],” concludes Gupta. This research might inform the development of treatments for metabolic inflammation.

*Anna Kriebs, Senior Editor, Nature Communications*

45 **ORIGINAL ARTICLE** Shan, B et al. Perivascular mesenchymal cells control adipose-tissue macrophage accrual in obesity. *Nat. Metab.* <https://doi.org/10.1038/s42255-020-00301-7> (2020)



# Perivascular mesenchymal cells control adipose-tissue macrophage accrual in obesity

Bo Shan<sup>1,6</sup>, Mengle Shao<sup>1,6</sup>, Qianbin Zhang<sup>1</sup>, Chelsea Hepler<sup>1</sup>, Vivian A. Paschoal<sup>1</sup>, Spencer D. Barnes<sup>2</sup>, Lavanya Vishvanath<sup>1</sup>, Yu A. An<sup>1</sup>, Lin Jia<sup>3</sup>, Venkat S. Malladi<sup>1,2</sup>, Douglas W. Strand<sup>4</sup>, Olga T. Gupta<sup>1,5</sup>, Joel K. Elmquist<sup>3</sup>, Dayoung Oh<sup>1</sup> and Rana K. Gupta<sup>1</sup>✉

**Chronic low-grade white adipose tissue (WAT) inflammation is a hallmark of metabolic syndrome in obesity. Here, we demonstrate that a subpopulation of mouse WAT perivascular (PDGFR $\beta$ <sup>+</sup>) cells, termed fibro-inflammatory progenitors (FIPs), activate proinflammatory signalling cascades shortly after the onset of high-fat diet feeding and regulate proinflammatory macrophage accumulation in WAT in a TLR4-dependent manner. FIPs activation in obesity is mediated by the downregulation of zinc-finger protein 423 (ZFP423), identified here as a transcriptional corepressor of NF- $\kappa$ B. ZFP423 suppresses the DNA-binding capacity of the p65 subunit of NF- $\kappa$ B by inducing a p300-to-NuRD coregulator switch. Doxycycline-inducible expression of *Zfp423* in PDGFR $\beta$ <sup>+</sup> cells suppresses inflammatory signalling in FIPs and attenuates metabolic inflammation of visceral WAT in obesity. Inducible inactivation of *Zfp423* in PDGFR $\beta$ <sup>+</sup> cells increases FIP activity, exacerbates adipose macrophage accrual and promotes WAT dysfunction. These studies implicate perivascular mesenchymal cells as important regulators of chronic adipose-tissue inflammation in obesity and identify ZFP423 as a transcriptional break on NF- $\kappa$ B signalling.**

In the setting of chronic caloric excess, the expansion of visceral white adipose tissue (WAT) mass is often accompanied by the accumulation of proinflammatory macrophages. Adipose tissue macrophage (ATM) accrual is mediated by mechanisms promoting both macrophage recruitment<sup>1,2</sup> and macrophage proliferation<sup>3</sup>. This unresolved low-grade meta-inflammatory state of visceral WAT is a defining feature of metabolic syndrome in obesity, and a contributor to the development of insulin resistance and vascular complications observed in type 2 diabetes<sup>4</sup>.

Current efforts focus primarily on the role of adipocytes and classical immune cells in the development of metabolic WAT inflammation; however, the contributions of resident mesenchymal stromal cells in this regard have remained poorly defined. Our single-cell RNA-sequencing (RNA-seq) efforts to define resident adipocyte precursor cells (APCs) have revealed the existence of functionally distinct subpopulations of PDGFR $\beta$ <sup>+</sup> perivascular cells in visceral WAT of adult mice<sup>5</sup>. PDGFR $\beta$ <sup>+</sup> marks the expression of mural cells (pericytes and vascular smooth muscle) as well as perivascular adventitial cells. PDGFR $\beta$ <sup>+</sup>LY6C<sup>-</sup>CD9<sup>-</sup> cells are highly committed perivascular APCs and represent <20% of all PDGFR $\beta$ <sup>+</sup> cells within murine visceral WAT. PDGFR $\beta$ <sup>+</sup>LY6C<sup>+</sup> cells are a distinct population of PDGFR $\beta$ <sup>+</sup> cells that we refer to as FIPs. FIPs display a fibrogenic, collagen-producing phenotype, lack adipogenic capacity and can exert an antiadipogenic effect on APCs through the production of secreted factors. Approximately 60–80% of all PDGFR $\beta$ <sup>+</sup> cells within intra-abdominal WAT depots are FIPs. Profiling of global gene-expression and unbiased pathway analysis of FIPs and APCs has revealed that FIPs are enriched in the expression of genes related to classical proinflammatory signalling cascades, including genes encoding notable regulators of macrophage activation and

accumulation in WAT. These data suggest the hypothesis that FIPs can modulate macrophage homeostasis in WAT in vivo.

Here, we demonstrate that WAT FIPs are acutely activated under physiological conditions associated with metabolic inflammation. We present multiple inducible gain- and loss-of-function mouse models that indicate that the activation of inflammatory signalling pathways in FIPs is sufficient and necessary to drive sustained visceral adipose-tissue macrophage accrual in obesity. Mechanistically, the activation of FIPs is mediated, at least in part, by the downregulation of the C2H2 zinc-finger transcriptional regulator, ZFP423, which we identify as a repressor of p65–nuclear factor kappa-light-chain-enhancer of activated B cells (NF- $\kappa$ B) activity in perivascular cells. These studies highlight an important role for perivascular mesenchymal cells in the regulation of chronic adipose-tissue inflammation in obesity, and suggest that proinflammatory stromal cells are possible targets for therapeutic interventions designed to promote healthy energy storage in adipose tissue.

## Results

**FIPs are physiologically activated in association with metabolic inflammation.** Given their abundance in the WAT stromal vascular fraction (SVF), we hypothesized that FIPs can sense proinflammatory stimuli and subsequently modulate WAT macrophage homeostasis in vivo. To begin to test this hypothesis, we examined the relative frequencies and gene-expression profiles of FIPs and APCs in settings associated with metabolic inflammation of WAT. First, we quantified and isolated FIPs and APCs by FACS from epididymal WAT depots of 10-week-old mice maintained on either a chow diet or a high-fat diet (HFD) for 1, 3 or 7 d (Fig. 1a and Supplementary Fig. 1). Short-term HFD feeding

<sup>1</sup>Touchstone Diabetes Center, Department of Internal Medicine, University of Texas Southwestern Medical Center, Dallas, TX, USA. <sup>2</sup>Lyda Hill Department of Bioinformatics, University of Texas Southwestern Medical Center, Dallas, TX, USA. <sup>3</sup>Center for Hypothalamic Research, Department of Internal Medicine, University of Texas Southwestern Medical Center, Dallas, USA. <sup>4</sup>Department of Urology, University of Texas Southwestern Medical Center, Dallas, TX, USA. <sup>5</sup>Department of Pediatrics, University of Texas Southwestern Medical Center, Dallas, TX, USA. <sup>6</sup>These authors contributed equally: Bo Shan, Mengle Shao. ✉e-mail: [Rana.Gupta@UTSouthwestern.edu](mailto:Rana.Gupta@UTSouthwestern.edu)

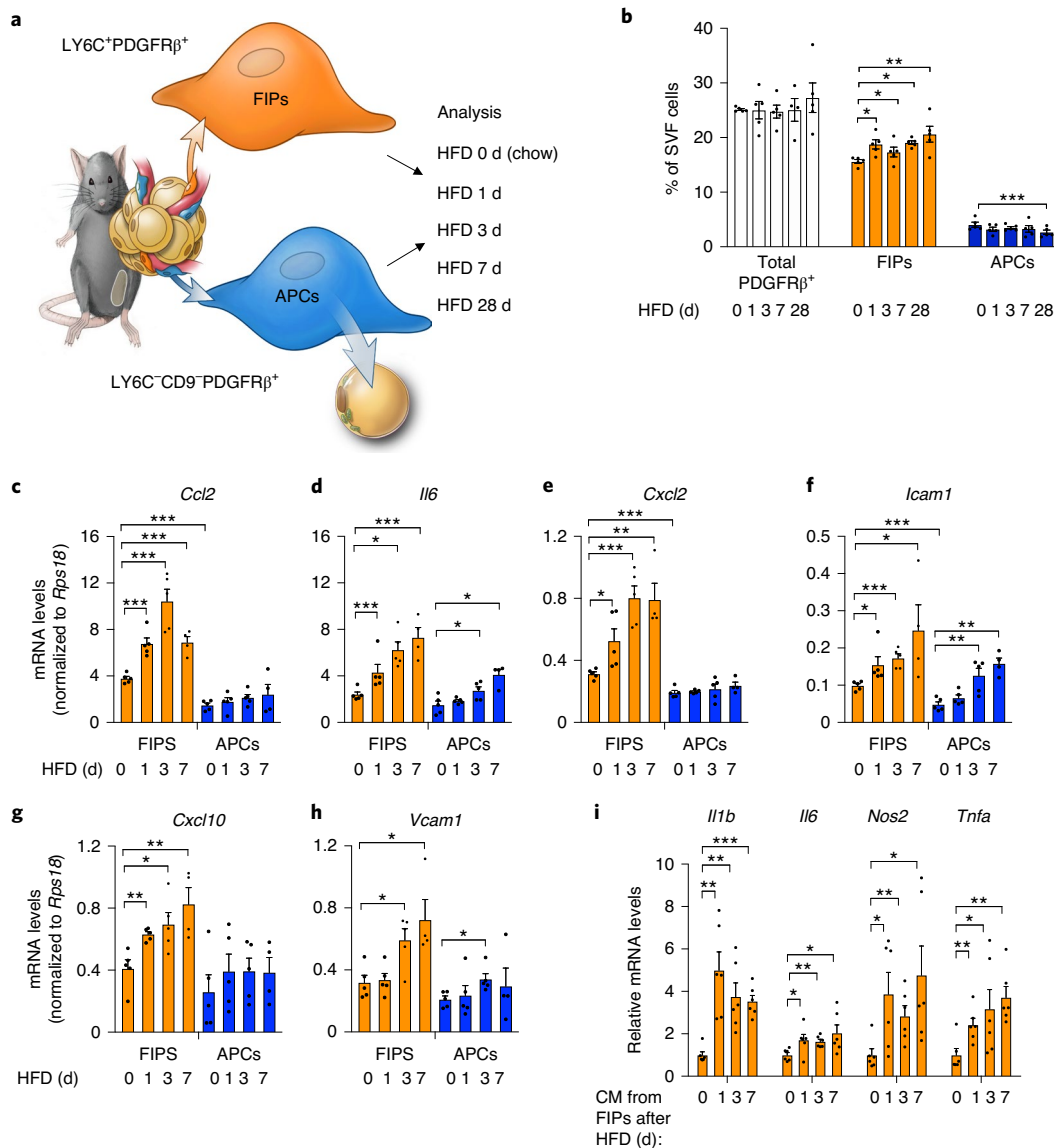


**Fig. 1 | FIPs are activated in association with adipose-tissue inflammation.** **a**, Experimental design. APCs (LY6C<sup>-</sup>CD9<sup>-</sup>PDGFRβ<sup>+</sup>) and FIPs (LY6C<sup>+</sup>PDGFRβ<sup>+</sup>) were isolated by FACS from gonadal WAT obtained from 10-week-old male C57BL/6 mice fed a standard chow diet (0 days HFD) or HFD for 1 d (HFD 1 d), 3 d (HFD 3 d) or 7 d (HFD 7 d) at 22 °C. Illustration is reproduced from Hepler et al.<sup>5</sup> **b**, Frequency of total PDGFRβ<sup>+</sup> cells and PDGFRβ<sup>+</sup> subpopulations in gonadal WAT at the indicated time points (d) following the onset of HFD feeding. Data are presented as a percentage of all live SVF cells obtained from gonadal WAT. **c–h**, Gene-expression analysis of FIPs and APCs: mRNA levels of *Ccl2* (**c**), *Il6* (**d**), *Cxcl2* (**e**), *Icam1* (**f**), *Cxcl10* (**g**) and *Vcam1* (**h**) in FIPs and APCs isolated at the indicated time points. Representative data from a single experiment are shown. Data in panels **b–h** were reproduced in three independent experiments. For the representative experiment shown,  $n=5$  samples for HFD 0 days (chow).  $n=5$  for HFD 1 d.  $n=5$  for HFD 3 d.  $n=4$  for HFD 7 d.  $n=5$  for HFD 28 d. Each sample ( $n$ ) represents  $\sim 3 \times 10^4$  cells sorted from a pool of two fat depots from one mouse.  $*P < 0.05$ ,  $**P < 0.01$  and  $***P < 0.001$  by one-way analysis of variance (ANOVA). **i**, Macrophage activation following exposure to FIP conditioned medium. mRNA levels of genes associated with macrophage activation in cultured BMDMs following exposure to the indicated FIP conditioned medium for 1.5 h.  $n=6$  independent wells of macrophages examined per experiment. Experiments in **i** were independently repeated two times. Representative data from two experiments are shown.  $*P < 0.05$ ,  $**P < 0.01$ , and  $***P < 0.001$  by one-way ANOVA. In all panels, bars represent mean  $\pm$  s.e.m. Each dot represents value of individual measurement ( $n$ ).

led to only slight fluctuations in the relative proportions of FIPs and APCs; FIPs remained much more abundant than APCs during this time (Fig. 1b). Twenty-eight days of HFD feeding led to a statistically significant increase in the ratio of FIPs to APCs, with greater than 80% of PDGFRβ<sup>+</sup> cells expressing markers of FIPs (Fig. 1b). Notably, short-term exposure to HFD led to a rapid and robust induction in messenger RNA levels of well-described proinflammatory chemokines (*Ccl2*, *Cxcl2*, *Cxcl10*), cytokines

(*Il6*) and adhesion molecules (*Icam1*, *Vcam1*) in FIPs (Fig. 1c–h). On the contrary, mRNA levels of only some of the examined genes increased in the APCs during this time, and this occurred to a much-lesser degree than was observed in FIPs. We then asked whether the induction of these genes in FIPs following HFD feeding reflected a heightened functional proinflammatory phenotype. To test this, we exposed primary cultures of bone-marrow-derived macrophages (BMDMs) to conditioned medium collected from

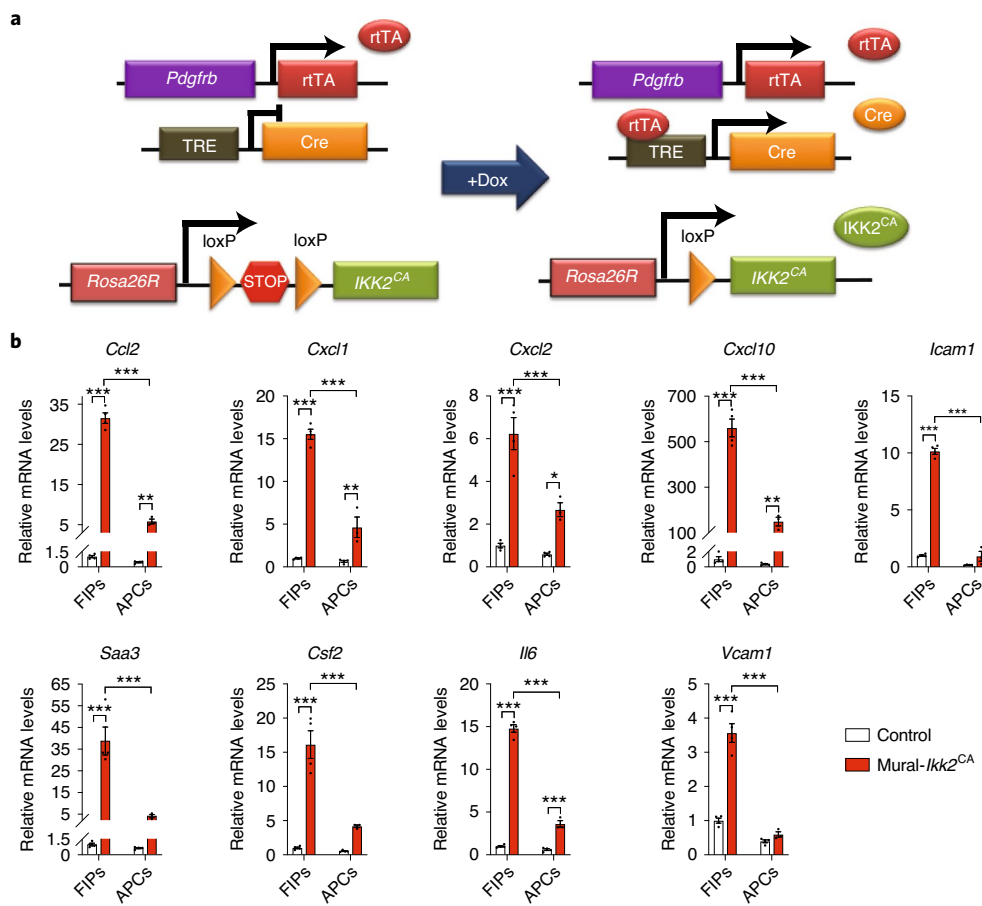


**Fig. 2 | FIPs are more responsive than APCs to the activation of NF- $\kappa$ B signalling.** **a**, Mural-*Ikk2<sup>CA</sup>* mice were derived by breeding *Pdgfrb<sup>rtTA</sup>* transgenic mice to animals expressing Cre recombinase under the control of the tetracycline-response element (*TRE-Cre*) and carrying the *Rosa26R<sup>Ikk2<sup>CA</sup></sup>* allele. Littermates carrying only *Pdgfrb<sup>rtTA</sup>* and *Rosa26R<sup>Ikk2<sup>CA</sup></sup>* alleles (that is, Cre<sup>-</sup>) were used as the control animals. The addition of doxycycline leads to activation of the *Rosa26R<sup>Ikk2<sup>CA</sup></sup>* allele and constitutively active (CA) IKK2 in *Pdgfrb*-expressing cells. CA IKK2 expression leads to activation of NF- $\kappa$ B signalling. **b**, mRNA levels of indicated proinflammatory genes in cultured FIPs and APCs 1 d following the addition of doxycycline ( $1 \mu\text{g ml}^{-1}$ ) to culture medium. Data presented were reproduced in two independent experiments. Bars represent mean  $\pm$  s.e.m. \**P* < 0.05, \*\**P* < 0.01 and \*\*\**P* < 0.001 by two-way ANOVA.

cultured FIPs obtained following HFD feeding. The expression levels of *Il1b*, *Il6*, *Nos2* and *Tnfa* (indicators of activated macrophages) were elevated in the macrophages exposed to the conditioned medium from FIPs collected from HFD-fed mice (Fig. 1i). The activation of BMDMs is less robust when exposed to conditioned medium from FIPs obtained from chow-fed mice. Collectively, these data provide evidence that FIPs exert a proinflammatory phenotype that is activated acutely following HFD feeding.

Thermoneutral (30 °C) housing conditions accelerate the development of metabolic WAT inflammation in obesity<sup>6,7</sup>. As such, we explored the effect of thermoneutrality on the inflammatory responses of FIPs (Extended Data Fig. 1a). mRNA levels of all of the inflammatory cytokines examined were higher in FIPs than in APCs under both housing conditions; however, FIPs isolated from animals maintained at TN expressed higher levels of inflammatory genes when than did FIPs isolated from animals maintained at room temperature (Extended Data Fig. 1b). These data indicate that thermoneutral housing amplifies the activation of the proinflammatory phenotype of FIPs by HFD feeding, and provide further evidence that the proinflammatory phenotype of these cells is regulated physiologically.

We also performed unbiased bulk RNA-seq and gene set enrichment analysis of FIPs and APCs isolated from mice maintained on HFD at 30 °C for 28 d. FIPs were enriched in a number of gene

signatures associated with heightened proinflammatory signalling (Supplementary Tables 1 and 2). These data, along with our prior single-cell gene-expression analysis, suggested that FIPs activate a number of classical proinflammatory signalling cascades that are implicated in the development of metabolic inflammation, including tumour necrosis factor- $\alpha$  (TNF- $\alpha$ ) signalling, interleukin-6 (IL-6) signalling and TLR (toll-like receptor) signalling<sup>5</sup> (Supplementary Table 1). Quantitative PCR (qPCR) analysis of FIPs and APCs isolated from HFD-diet fed mice validated the observed expression differences in the 15 most differentially expressed genes among the identified ‘HALLMARK\_TNFA\_SIGNALING\_VIA\_NFKB’ signature. All 15 signature genes reflective of heightened TNF- $\alpha$  signalling were significantly and robustly enriched in FIPs compared with their levels in APCs (Extended Data Fig. 1c).

The NF- $\kappa$ B signalling cascade is a classical signalling pathway that integrates many of the aforementioned pathways and is robustly activated within WAT after HFD feeding<sup>8,9</sup>. We asked whether the differential gene-expression response of FIPs and APCs in proinflammatory settings might reflect an intrinsic difference in their potential to respond to NF- $\kappa$ B activation. We derived a genetic ‘Tet-On’ system in which the addition of doxycycline results in expression of a constitutively active form of IKK2 (*IKK2<sup>CA</sup>*) in PDGFR $\beta$ <sup>+</sup> cells (Mural-*Ikk2<sup>CA</sup>* mice) (Fig. 2a). *IKK2<sup>CA</sup>* expression leads to activation of NF- $\kappa$ B signalling and is sufficient to drive the activation

of several known NF- $\kappa$ B transcriptional targets; however, genetic NF- $\kappa$ B activation differentially impacts FIPs and APCs (Fig. 2b). mRNA levels of all of the genes encoding proinflammatory cytokines or adhesion molecules are induced much more robustly in FIPs than in APCs. These data provide additional evidence that FIPs are inherently more proinflammatory than are APCs.

**TLR4 signalling in PDGFR $\beta$ <sup>+</sup> cells regulates WAT macrophage accrual in obesity.** Whether the activation of proinflammatory signalling pathways in PDGFR $\beta$ <sup>+</sup> cells impacts the development of metabolic WAT inflammation associated with obesity has remained unclear. To address this, we derived a loss-of-function model in which *Tlr4* can be inactivated in PDGFR $\beta$ <sup>+</sup> cells in a doxycycline-inducible manner (*Pdgfrb*<sup>Cre/TA</sup>; *TRE-Cre*; *Tlr4*<sup>loxP/loxP</sup>, herein, Mural-*Tlr4*<sup>KO</sup> mice) (Extended Data Fig. 2a). Eight-week-old male control (*Pdgfrb*<sup>Cre/TA</sup>; *Tlr4*<sup>loxP/loxP</sup> mice (that is, Cre<sup>-</sup>) and Mural-*Tlr4*<sup>KO</sup> mice were switched to a doxycycline-containing HFD (Dox-HFD) diet for up to 5 months and maintained at room temperature. Thus, Cre expression was initiated at the onset of HFD feeding and maintained for the duration of the experiment. Over the 5-month period, body weights and WAT mass remained indistinguishable between the two groups (Fig. 3a,b). One month after the onset of Dox-HFD feeding, the frequencies of FIPs, APCs and total PDGFR $\beta$ <sup>+</sup> cells were not impacted by the inactivation of *Tlr4* (Fig. 3c). Gene-expression analysis of freshly isolated FIPs and APCs confirmed the suppression of *Tlr4* mRNA levels in both PDGFR $\beta$ <sup>+</sup> subpopulations (Fig. 3d). The loss of *Tlr4* specifically in PDGFR $\beta$ <sup>+</sup> cells was associated with a statistically significant reduction in mRNA levels of many of the proinflammatory genes assayed within isolated FIPs, but not in APCs (Fig. 3e). Notably, levels of the proinflammatory transcripts analysed with *Tlr4*-deficient FIPs were reduced to levels normally found in APCs. Moreover, loss of proinflammatory-gene expression in FIPs is associated with reduced levels of notable proinflammatory cytokines and macrophage markers measured across adipose tissue as a whole (Fig. 3f,g).

Differences in the degree of systemic glucose homeostasis and gonadal adipose inflammation between the two genotypes were even more readily apparent after long-term HFD feeding. Mural-*Tlr4*<sup>KO</sup> mice were relatively more glucose tolerant and insulin sensitive than were control animals (Extended Data Fig. 2b,c). We observed fewer MAC-2<sup>+</sup> immune cells and crown-like structures within gonadal WAT of Mural-*Tlr4*<sup>KO</sup> mice compared with control animals (Fig. 3h,i). In addition, mRNA levels of all proinflammatory cytokine/chemokines and macrophage-selective genes that we examined were markedly lower in WAT of Mural-*Tlr4*<sup>KO</sup> mice (Fig. 3j,k). We analysed the frequency of ATMs directly by flow cytometry, using multiple cell-labelling strategies for ATM subtypes

(Supplementary Fig. 2)<sup>10,11</sup>. The total number of ATMs in *Tlr4*-deficient gonadal WAT was significantly lower than observed in gonadal WAT of control mice (Fig. 3l). In particular, the numbers of proinflammatory ATMs within transgenic gonadal WAT were ~50% lower than observed in controls (Fig. 3m). Notably, frequencies of proinflammatory CD9<sup>+</sup> ATMs, which typically reside in crown-like structures of metabolically inflamed WAT<sup>11</sup>, were strongly reduced within the gonadal WAT of transgenic mice. Importantly, levels of total and proinflammatory monocytes in the blood, bone marrow and spleen were not impacted by the loss of *Tlr4* in PDGFR $\beta$ <sup>+</sup> cells (Extended Data Fig. 2d–f). This strongly suggests that the reduction in WAT macrophage accumulation in Mural-*Tlr4*<sup>KO</sup> mice is not secondary consequence to an altered monocyte/macrophage pool in another tissue. To confirm this, we assayed immune-cell migration into WAT depots of obese mice following injection of labelled monocytes. Injected tdTomato<sup>+</sup> monocytes migrate into WAT depots of HFD-fed control animals and adopt an adipose-tissue macrophage phenotype<sup>2</sup>. In the Mural-*Tlr4*<sup>KO</sup> mice, the amount of monocyte migration into WAT is significantly lower than that observed in controls (Fig. 3n). These data highlight an important role for TLR4 signalling in mediating the proinflammatory response of FIPs, and provide evidence that proinflammatory signalling in PDGFR $\beta$ <sup>+</sup> cells is necessary to drive sustained ATM accrual in obesity.

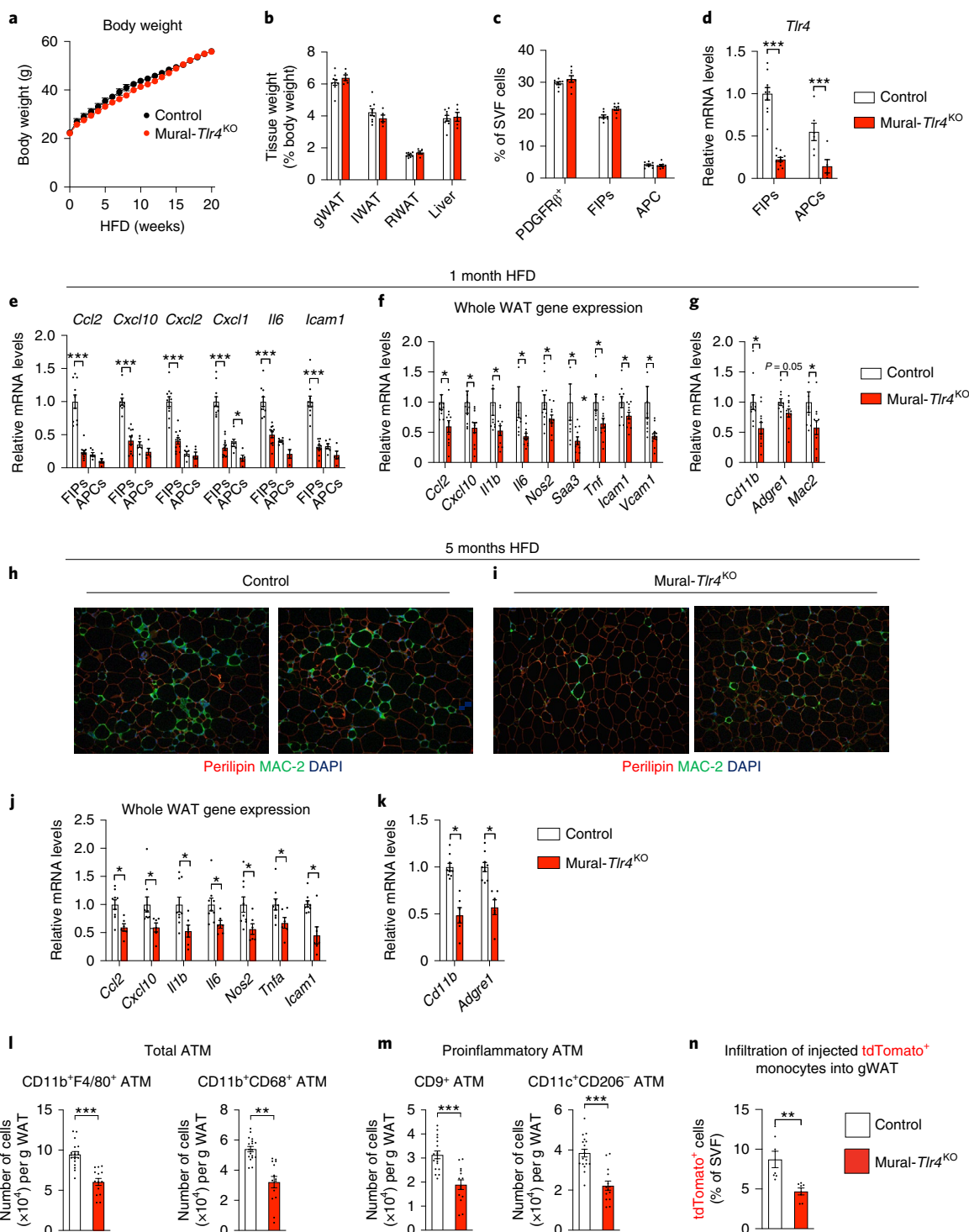
**ZFP423 suppresses the proinflammatory phenotype of FIPs.** *Zfp423* expression is one defining feature of committed preadipocytes in the perigonadal WAT of mice<sup>5,12,13</sup>. *Zfp423* encodes a multi-C2H2 zinc-finger transcriptional regulator that has multiple roles in the establishment and maintenance of the adipocyte lineage<sup>12,14–17</sup>. Using transgenic *Zfp423*<sup>GFP</sup> reporter mice, we previously determined that PDGFR $\beta$ <sup>+</sup> cells expressing high mRNA levels of *Zfp423* were enriched in markers of APCs, whereas cells expressing relatively lower levels of *Zfp423* were enriched in markers of FIPs and gene signatures associated with inflammatory signalling<sup>13</sup>. Our RNA-seq analysis described above was unable to confirm the enrichment of *Zfp423* in APCs; however, qPCR analysis with normalization to several housekeeping genes established that *Zfp423* expression is enriched in APCs of mice maintained on a HFD at thermoneutrality for 28 d (Supplementary Fig. 3). FIPs express detectable levels of *Zfp423*; however, mRNA levels in these cells are quantitatively lower than those observed in APCs. Notably, mRNA levels of *Zfp423* were further reduced in association with the activation of the proinflammatory signalling pathways in FIPs. Within 1–3 d of HFD feeding, expression of *Zfp423* declines in FIPs (Fig. 4a), in association with the aforementioned induction in mRNA levels of proinflammatory cytokines (see Fig. 1c–h). FIPs treated directly with lipopolysaccharide (LPS) or palmitate expressed lower levels

**Fig. 3 | Loss of *Tlr4* in PDGFR $\beta$ <sup>+</sup> cells attenuates WAT macrophage accumulation in obesity.** **a**, Control ( $n = 7$ ; black) and Mural-*Tlr4*<sup>KO</sup> ( $n = 9$ ; red) body weights following the onset of HFD feeding at room temperature. **b**, Gonadal WAT (gWAT), inguinal WAT (IWAT), retroperitoneal WAT (RWAT) and liver mass of control ( $n = 9$ ) and Mural-*Tlr4*<sup>KO</sup> ( $n = 5$ ) mice after 5 months of HFD feeding. **c**, Frequency of total PDGFR $\beta$ <sup>+</sup> cells, FIPs and APCs, within gonadal WAT of control ( $n = 8$ ) and Mural-*Tlr4*<sup>KO</sup> ( $n = 8$ ) mice after 1 month of HFD feeding. **d**, *Tlr4* mRNA levels within FIPs and APCs of control ( $n = 10$ ) and Mural-*Tlr4*<sup>KO</sup> ( $n = 11$ ) mice after 1 month of HFD feeding. For controls: FIPs  $n = 10$ ; APCs  $n = 6$ . For Mural-*Tlr4*<sup>KO</sup>: FIPs  $n = 11$ ; APCs  $n = 5$ . **e**, Proinflammatory-gene expression within gonadal WAT FIPs and APCs of control ( $n = 10$ ) and Mural-*Tlr4*<sup>KO</sup> ( $n = 11$ ) mice after 1 month of HFD feeding. For controls: FIPs  $n = 10$ ; APCs  $n = 6$ . For Mural-*Tlr4*<sup>KO</sup>: FIPs  $n = 11$ ; APCs  $n = 5$ . **f**, Proinflammatory-gene expression in gonadal WAT of control ( $n = 10$ ) and Mural-*Tlr4*<sup>KO</sup> ( $n = 11$ ) mice after 1 month of HFD feeding. **g**, mRNA levels of macrophage-selective genes in gonadal WAT of control ( $n = 10$ ) and Mural-*Tlr4*<sup>KO</sup> ( $n = 11$ ) mice after 1 month of HFD feeding. **h,i**, Magnified ( $\times 10$ ) images of perilipin (red) and MAC-2 (green) expression in gonadal WAT section from control mice (**h**) and Mural-*Tlr4*<sup>KO</sup> mice (**i**) maintained on HFD for 5 months. **j**, Proinflammatory-gene expression in gonadal WAT of control ( $n = 9$ ) and Mural-*Tlr4*<sup>KO</sup> ( $n = 6$ ) mice after 5 months of HFD feeding. **k**, mRNA levels of macrophage-selective genes in gonadal WAT of control ( $n = 9$ ) and Mural-*Tlr4*<sup>KO</sup> ( $n = 6$ ) mice after 5 months of HFD feeding. **l**, Frequency of total ATMs in gonadal WAT of control ( $n = 18$ ) and Mural-*Tlr4*<sup>KO</sup> ( $n = 14$ ) mice after 5 months of HFD feeding. **m**, Frequency of proinflammatory ATMs within gonadal WAT of control ( $n = 18$ ) and Mural-*Tlr4*<sup>KO</sup> ( $n = 14$ ) mice after 5 months of HFD feeding. **n**, Frequency of tdTomato<sup>+</sup> macrophages within gonadal WAT SVF of obese mice following injection of tdTomato<sup>+</sup> monocytes.  $n = 7$  for control and  $n = 7$  for Mural-*Tlr4*<sup>KO</sup> mice. Bars represent mean  $\pm$  s.e.m. \* $P < 0.05$ , \*\* $P < 0.01$  or \*\*\* $P < 0.001$  by unpaired two-tailed Student's *t*-test (**f,g,j–n**) or one-way ANOVA (**d,e**).

of *Zfp423* than did vehicle-treated cells (Fig. 4b,c). These data raise the hypothesis that ZFP423 exerts an anti-inflammatory effect in perivascular cells, with the downregulation of *Zfp423* expression serving as a mechanism to activate the proinflammatory phenotype of these cells.

We derived a genetic gain-of-function model in which *Zfp423* expression can be induced in PDGFR $\beta$ <sup>+</sup> cells in a doxycycline-inducible manner (*Pdgfrb*<sup>rtTA</sup>;TRE-*Zfp423*; Mural-*Zfp423*<sup>TG</sup> mice) (Fig. 4d). We first explored the functional consequences of *Zfp423* overexpression in vitro, using cultured FIPs isolated from gonadal

WAT of chow-fed control mice (mice carrying the *Pdgfrb*<sup>rtTA</sup> allele) and Mural-*Zfp423*<sup>TG</sup> mice. The addition of doxycycline to cultured FIPs led to a two- to threefold induction in overall *Zfp423* mRNA levels (Fig. 4e). This modest induction was sufficient to attenuate LPS-driven activation of proinflammatory-gene expression (Fig. 4f). *Zfp423* overexpression also diminished the capacity of FIPs to promote macrophage activation and migration. BMDMs exposed to conditioned medium from LPS-treated Mural-*Zfp423*<sup>TG</sup> FIPs expressed relatively lower levels of *Ccl2*, *Il1b*, *Il6*, *Nos2* and *Tnfa* than did BMDMs exposed to conditioned medium from LPS-treated control



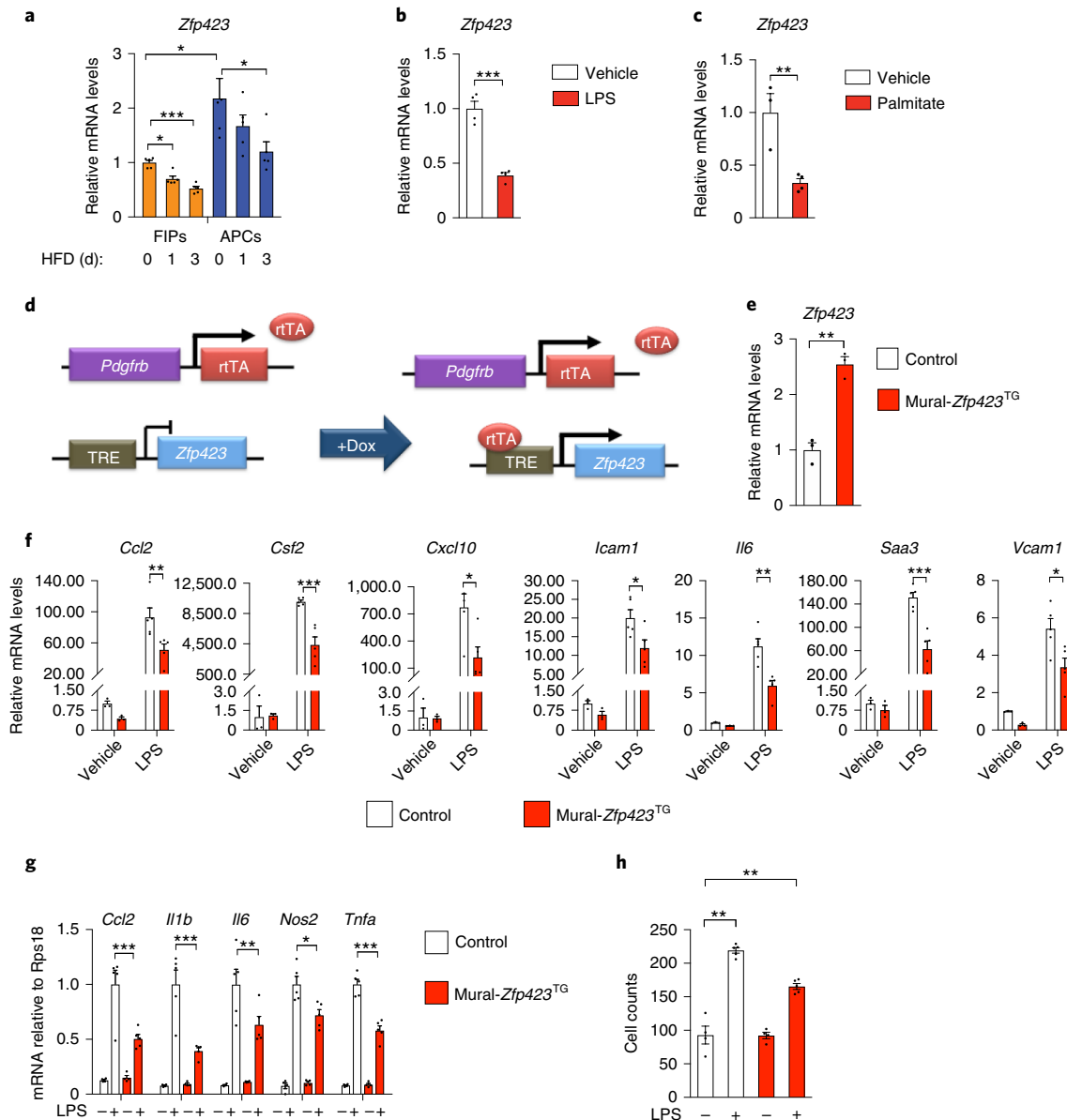


**Fig. 4 | *Zfp423* suppresses the proinflammatory phenotype of FIPs.** **a**, mRNA levels of *Zfp423* in FIPs and APCs from gonadal WAT of mice after HFD feeding for 0 d (chow) ( $n=5$ ), 1 d ( $n=5$ ) and 3 d ( $n=5$ ). **b**, mRNA levels of *Zfp423* in primary FIP cultures treated with vehicle (PBS) ( $n=4$ ) or 100 ng ml<sup>-1</sup> LPS ( $n=4$ ) for 6 h. **c**, mRNA levels of *Zfp423* in primary FIPs cultures treated with vehicle (BSA) ( $n=3$ ) or 500 nmol l<sup>-1</sup> palmitate ( $n=5$ ) for 3 h. **d**, Mural-*Zfp423*<sup>TG</sup> (*Pdgfrb*<sup>rtTA</sup>; *TRE-Zfp423*) mice were generated by breeding the *Pdgfrb*<sup>rtTA</sup> transgenics to animals expressing *Zfp423* under the control of the tetracycline-response element (*TRE-Zfp423*). Littermates carrying only *Pdgfrb*<sup>rtTA</sup> were used as the controls. In the presence of doxycycline, rtTA activates *Zfp423* expression in *Pdgfrb*-expressing cells. **e**, mRNA levels of *Zfp423* within primary gonadal WAT FIPs cultures from lean control and Mural-*Zfp423*<sup>TG</sup> mice 24 h after the addition of doxycycline (1 μg ml<sup>-1</sup>) to culture medium. FIPs were isolated from pooled depots from 5 mice and then plated immediately into triplicate wells for analysis ( $n=3$  per group). **f**, mRNA levels of indicated genes in primary FIPs cultures treated with vehicle ( $n=3$ ) or 100 ng ml<sup>-1</sup> LPS ( $n=5$ ) for 2 h. **g**, mRNA levels of genes associated with macrophage activation in cultured BMDMs following exposure to indicated FIP conditioned medium for 1.5 h. **h**, Macrophage migration following exposure to FIP conditioned medium: cell counts of migrated macrophages following exposure to indicated CM for 3 h. For **g** and **h**, FIPs (isolated from pooled depots of 6–8 mice per genotype) were treated with vehicle or LPS (100 ng ml<sup>-1</sup>) for 2 h and then incubated in serum-free medium for an additional 24 h to produce conditioned medium.  $n=4$  (for groups with vehicle treatment) or  $n=5$  (for groups with LPS treatment) independent wells of macrophages were examined per experiment. Experiments were independently repeated three times (**a–c, e, f**) or twice (**g, h**). Data in this figure are shown as the mean ± s.e.m. \* $P < 0.05$ , \*\* $P < 0.01$  or \*\*\* $P < 0.001$  by two-tailed unpaired Student's *t*-test (**b, c**), one-way ANOVA (**a**) or two-way ANOVA (**f–h**).

FIPs (Fig. 4g). Moreover, the migratory response of BMDMs to conditioned medium from LPS-treated Mural-*Zfp423*<sup>TG</sup> FIPs was attenuated in comparison to the response elicited by conditioned medium from LPS-treated control FIPs (Fig. 4h). Thus, ZFP423 overexpression leads to a suppression of the FIPs proinflammatory phenotype.

We also examined whether inactivation of *Zfp423* might amplify the proinflammatory phenotype of FIPs. We utilized our previously reported model of doxycycline-inducible *Zfp423* ablation in *Pdgfrb*-expressing cells (*Pdgfrb*<sup>rtTA</sup>; *TRE-Cre*; *Zfp423*<sup>loxP/loxP</sup>; Mural-*Zfp423*<sup>KO</sup> mice) (Extended Data Fig. 3a)<sup>15</sup>. After 7 d of

doxycycline-containing chow-diet feeding, mRNA levels of *Zfp423* were reduced by ~75% in isolated FIPs from Mural-*Zfp423*<sup>KO</sup> mice (Extended Data Fig. 3b). *Zfp423* inactivation in FIPs led to a heightened proinflammatory phenotype in vitro. In response to LPS, *Zfp423*-deficient FIPs expressed higher mRNA levels of notable proinflammatory genes than did LPS-treated control FIPs (Extended Data Fig. 3c). BMDMs exposed to conditioned medium from LPS-treated Mural-*Zfp423*<sup>KO</sup> FIPs exhibited a more 'activated' gene-expression profile in comparison with BMDMs exposed to conditioned medium from LPS-treated control FIPs (Extended Data Fig. 3d). The migratory response of BMDMs to conditioned medium from LPS-treated control FIPs is already fairly robust; however, the response to conditioned medium from LPS-treated Mural-*Zfp423*<sup>KO</sup> FIPs was slightly, but reproducibly, elevated (Extended Data Fig. 3e). Taken together, these *Zfp423* gain- and loss-of-function studies indicate that *Zfp423* suppresses the proinflammatory phenotype of FIPs in a cell-autonomous manner.

***Zfp423* overexpression in PDGFRβ<sup>+</sup> cells attenuates LPS-driven WAT inflammation.** Next, we sought to determine whether *ZFP423* regulates the proinflammatory phenotype of native FIPs in vivo, and whether modulating *Zfp423* expression can impact the development of WAT inflammation. To this end, we utilized mice that were maintained at thermoneutrality owing to the heightened inflammatory response FIPs exhibit under these housing conditions. Control and Mural-*Zfp423*<sup>TG</sup> male mice were switched to a doxycycline-containing chow diet for 4 weeks before they were administered a single dose of LPS (Fig. 5a). LPS-induced proinflammatory-gene expression within gonadal WAT FIPs of control mice. The overall response was more robust in FIPs than in APCs, providing additional evidence that FIPs exert a stronger transcriptional response to proinflammatory signals than do APCs (Fig. 5b). Four weeks of doxycycline treatment led to an increase in overall *Zfp423* mRNA levels within both FIPs and APCs of gonadal WAT of Mural-*Zfp423*<sup>TG</sup> mice (Fig. 5b). Importantly, transgene activation increased *Zfp423* mRNA levels in FIPs to levels typically observed in APCs of control mice. This modest level of *Zfp423* induction was sufficient to significantly blunt the transcriptional response to LPS within FIPs, whole gonadal WAT and whole retroperitoneal WAT from Mural-*Zfp423*<sup>TG</sup> mice (Fig. 5b and Supplementary Fig. 4a,c). On the contrary, the expression levels of assayed proinflammatory genes in the liver were not impacted by transgenic expression of *Zfp423* in PDGFRβ<sup>+</sup> cells (Supplementary Fig. 4e). At 24h following LPS injection, the expression of macrophage-selective genes was elevated in WAT depots and livers of control animals (Supplementary Fig. 4b,d,f); however, the induction of these same genes was less robust in the WAT depots, but not in the livers, of Mural-*Zfp423*<sup>TG</sup> mice (Supplementary Fig. 4b,d,f). Flow-cytometry analysis revealed that the numbers of CD45<sup>+</sup>CD11b<sup>+</sup>F4/80<sup>+</sup> ATMs were lower in the gonadal WAT depot of Mural-*Zfp423*<sup>TG</sup> mice than was observed in the control tissues (Fig. 5c). These changes occurred in the absence of changes in circulating blood monocytes, resident bone marrow monocytes or splenic monocytes (Fig. 5d–f). These results confirm the anti-inflammatory function of *Zfp423* in native FIPs in vivo, and provide evidence that inflammatory signalling in PDGFRβ<sup>+</sup> cells contributes to the overall response of WAT to proinflammatory stimuli.

***Zfp423* overexpression in PDGFRβ<sup>+</sup> cells attenuates metabolic WAT inflammation.** We also examined whether overexpression of *Zfp423* in PDGFRβ<sup>+</sup> cells can suppress the proinflammatory response of FIPs associated with HFD feeding, and elicit a phenotype similar to that of obese Mural-*Tlr4*<sup>KO</sup> mice. Control and Mural-*Zfp423*<sup>TG</sup> male mice were switched to a Dox-HFD diet for up to 5 months. Over this period, body weights remained indistinguishable between the two groups (Fig. 6a). One month after the

onset of HFD feeding, adipose-tissue mass and the frequencies of the PDGFRβ<sup>+</sup> subpopulations did not significantly differ between Control and Mural-*Zfp423*<sup>TG</sup> mice (Fig. 6b,c). Total levels of *Zfp423* mRNA were increased by three- to fourfold in both FIPs and APCs, with *Zfp423* in FIPs reaching levels observed normally in APCs (Fig. 6d). This modest, yet physiological, level of *Zfp423* overexpression for 4 weeks of HFD feeding led to a significant reduction in expression of many of the proinflammatory genes assayed in FIPs. The mRNA levels of these transcripts were now reduced to levels observed naturally in APCs. The effects on gene expression in transgenic APCs were much more modest (Fig. 6e). Unbiased bulk RNA-seq analysis of control and *Zfp423*-transgenic FIPs confirmed and extended these findings. Among the most differentially expressed gene signatures in *Zfp423*-overexpressing FIPs after 1 month of HFD feeding were several of those related to proinflammatory signalling (Fig. 6f and Supplementary Tables 3 and 4).

Mural-*Zfp423*<sup>TG</sup> mice maintained long-term on HFD indeed exhibited a phenotype very similar to that of Mural-*Tlr4*<sup>KO</sup> mice. After 5 months of HFD feeding, adipose-tissue mass remained comparable between obese control and Mural-*Zfp423*<sup>TG</sup> mice (Fig. 6b); however, differences in the degree of adipose inflammation were readily apparent. The gonadal WAT depot of Mural-*Zfp423*<sup>TG</sup> mice exhibited less metabolic inflammation than was observed in control mice, evidenced by fewer MAC-2<sup>+</sup> immune cells and crown-like structures (Fig. 6g–n) and lower mRNA and protein levels of key proinflammatory cytokine/chemokines (Fig. 6o,p). The numbers of total and proinflammatory ATMs in transgenic gonadal WAT were ~50% lower than those observed in controls (Fig. 6q,r). Notably, in vivo cell-migration assays indicated that ~50% fewer injected tdTomato<sup>+</sup> monocytes infiltrate the gonadal WAT depot of Mural-*Zfp423*<sup>TG</sup> mice than that of controls (Fig. 6s). These data indicate that transgenic expression of *Zfp423* in PDGFRβ<sup>+</sup> cells, much like the inactivation of TLR4 signalling in PDGFRβ<sup>+</sup> cells, suppress ATM accumulation in obesity.

Our prior studies of inducible *Pparg* expression in progenitors demonstrated that increased de novo adipogenesis can drive healthy WAT remodelling in the setting of diet-induced obesity<sup>18</sup>. In vitro, *Zfp423* overexpression can drive *Pparg* expression and adipogenesis<sup>14</sup>; therefore, we evaluated whether the fourfold increase in *Zfp423* expression in APCs is similarly sufficient to drive adipocyte differentiation and improve other aspects of adipose-tissue health in Mural-*Zfp423*<sup>TG</sup> mice. We did not observe in the in vitro setting any substantial increase in the extent to which APCs undergo adipogenesis when *Zfp423* is expressed (Extended Data Fig. 4a). In vivo, mRNA levels of proadipogenic transcription factors in FIPs and APCs were comparable between obese control and Mural-*Zfp423*<sup>TG</sup> mice after 1 month of HFD feeding (Extended Data Fig. 4b). After 5 months of HFD feeding, mean adipocyte size, and whole adipose-tissue mRNA levels of adipocyte-selective genes and of genes associated with WAT were also comparable between the two groups (Extended Data Fig. 4c,d). We assessed de novo adipogenesis directly using our previously described pulse-chase lineage-tracing system, termed the MuralChaser model (*Pdgfrb*<sup>Cre</sup>; *TRE-Cre*; *Rosa26R*<sup>mT/mG</sup>)<sup>13</sup>. The addition of doxycycline to these transgenic animals triggers permanent activation of membrane-bound green fluorescent protein (mGFP) expression in *Pdgfrb*-expressing cells. This system can be used to quantitatively track the formation of new gonadal adipocytes (that is, mGFP<sup>+</sup> adipocytes) that emerge from PDGFRβ<sup>+</sup> cells in association with HFD feeding. We bred the *TRE-Zfp423* allele into the MuralChaser background to derive animals in which the addition of doxycycline drives *Zfp423* overexpression and indelible mGFP labelling of PDGFRβ<sup>+</sup> cells (herein MuralChaser-*Zfp423*<sup>TG</sup> mice) (Extended Data Fig. 4e). Following Dox-HFD feeding, we did not observe any significant difference in the numbers of mGFP<sup>+</sup> adipocytes in gonadal WAT between control and MuralChaser-*Zfp423*<sup>TG</sup> mice (Extended Data Fig. 4f,g). Therefore, *Zfp423* overexpression,

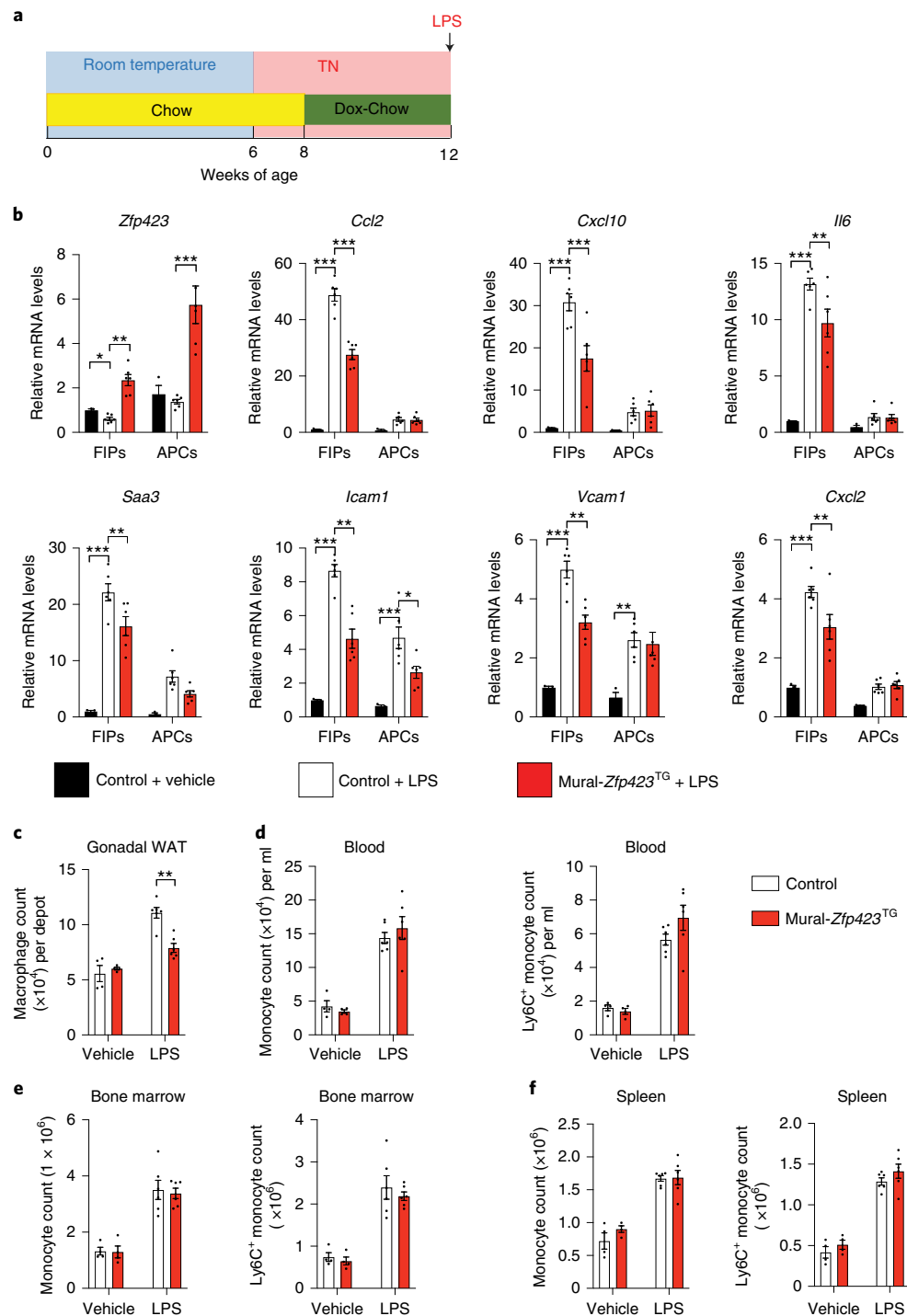


**Fig. 5 | *Zfp423* overexpression in PDGFR $\beta$ <sup>+</sup> cells limits LPS-induced WAT inflammation.** **a**, Experimental design. Mural-*Zfp423*<sup>TG</sup> or control mice were maintained at room temperature and then switched to thermoneutrality at the age of 6 weeks. Eight-week-old mice were given a doxycycline-containing chow diet (Dox-Chow) for another 4 weeks before being intraperitoneally injected with LPS (0.5 mg per kg (body weight)) or vehicle (PBS). Gonadal WAT was collected either 2 h (in **b**) or 24 h (in **c-f**) postinjection. **b**, mRNA levels of *Zfp423* and indicated proinflammatory genes in freshly isolated FIPs and APCs.  $n=3$  individual mice for control + vehicle group;  $n=6$  for control + LPS group;  $n=6$  for Mural-*Zfp423*<sup>TG</sup> + LPS group. **c**, Results of flow-cytometry analyses of CD45<sup>+</sup>CD11b<sup>+</sup>F4/80<sup>+</sup> macrophages in gonadal WAT. **d**, Frequency of total monocytes (CD45<sup>+</sup>CD11b<sup>+</sup>CD115<sup>+</sup>) and proinflammatory monocytes (CD45<sup>+</sup>CD11b<sup>+</sup>CD115<sup>+</sup>Ly6C<sup>+</sup>) in blood. **e**, Frequency of total monocytes and proinflammatory monocytes in bone marrow. **f**, Frequency of total monocytes and proinflammatory monocytes in spleen. For **c-f**,  $n=4$  individual mice for control + vehicle group;  $n=4$  individual mice for Mural-*Zfp423*<sup>TG</sup> + vehicle group;  $n=6$  for control + LPS group; and  $n=6$  for Mural-*Zfp423*<sup>TG</sup> + LPS group. All data are shown as the mean  $\pm$  s.e.m. For **b,c**, \* $P < 0.05$ , \*\* $P < 0.01$  or \*\*\* $P < 0.001$  by two-way ANOVA. All data presented were reproduced in two independent animal cohorts.

at least to the modest levels induced in this model, is not driving appreciable levels of de novo adipogenesis under these conditions. As such, the reduction in WAT inflammation occurring in this

setting is mostly probably driven by the anti-inflammatory function of ZFP423 in PDGFR $\beta$ <sup>+</sup> cells, rather than any direct proadipogenic function or influence on *Pparg* expression.

Chronic WAT inflammation, defined by the presence of proinflammatory macrophages, is tightly linked to insulin resistance in mice. We assessed the response of gonadal WAT in obese control and Mural-*Zfp423*<sup>TG</sup> mice to the actions of insulin, as reflected by the phosphorylation of its downstream signal transducer, Akt (pAKT). Indeed, levels of pAKT were significantly higher in the gonadal WAT of obese Mural-*Zfp423*<sup>TG</sup> mice following insulin stimulation than were pAKT levels in gonadal WAT from obese control mice (Extended Data Fig. 5a). Obese Mural-*Zfp423*<sup>TG</sup> mice exhibited relatively better glucose tolerance and systemic insulin sensitivity than did obese control animals (Extended Data Fig. 5b,c). Serum protein analysis supported these observations. Levels of the adipokine adiponectin are often indicative of adipose-tissue health and insulin sensitivity in obesity<sup>19</sup>. Adiponectin levels progressively declined as control animals became obese over the 5-month period of HFD feeding. This decline occurred to a lower extent in Mural-*Zfp423*<sup>TG</sup> mice (Extended Data Fig. 5d). Moreover, after 5 months of HFD feeding, serum insulin levels in the transgenic mice were nearly 50% of the levels observed in control mice (Extended Data Fig. 5d). Correlating with these phenotypes was a slight reduction in circulating protein levels of CCL2, IL-6 and TNF- $\alpha$  (Extended Data Fig. 5e). Importantly, most of the anti-inflammatory effects observed were limited to the adipose tissue, despite the overexpression of *Zfp423* in PDGFR $\beta$ <sup>+</sup> cells of other tissues. Levels of the expression of macrophage-selective genes (*Cd11b*, *Adgre1*) and most proinflammatory genes assayed within skeletal muscle and liver were not substantially impacted by *Zfp423* overexpression in PDGFR $\beta$ <sup>+</sup> cells, suggesting that the anti-inflammatory effects in this model were largely restricted to adipose tissue (Extended Data Fig. 5f,g). In fact, levels of total and proinflammatory monocytes in the blood, bone marrow and spleen were comparable between control and transgenic animals (Extended Data Fig. 5h–j). Collectively, these data are highly consistent with the notion that adipose-tissue inflammation is linked to systemic insulin sensitivity.

***Zfp423* inactivation in PDGFR $\beta$ <sup>+</sup> cells exacerbates metabolic WAT inflammation.** On the basis of the data above, it would be predicted that loss of *Zfp423* in PDGFR $\beta$ <sup>+</sup> cells would lead to elevated proinflammatory signalling and exacerbated adipose-tissue inflammation following HFD feeding. We previously examined adipose depots of Mural-*Zfp423*<sup>KO</sup> mice undergoing HFD feeding, with a strict focus on the impact of *Zfp423*-deficiency on adipocyte differentiation<sup>15</sup>. We found that visceral WAT PDGFR $\beta$ <sup>+</sup> cells lacking *Zfp423* are able to undergo adipogenesis in response to HFD feeding, indicating that *Zfp423* is dispensable for visceral adipocyte differentiation in adulthood. We did not examine adipose-tissue inflammation directly in this prior study; however, obese Mural-*Zfp423*<sup>KO</sup> mice did not appear to exhibit any impairment in glucose tolerance when compared with obese control animals.

Our prior study relied on Mural-*Zfp423*<sup>KO</sup> mice housed at 22 °C and maintained on HFD for only 8 weeks (ref. <sup>15</sup>). As described above, the proinflammatory phenotype of FIPs is significantly heightened under thermoneutral housing conditions. Therefore, we reassessed the impact of mural *Zfp423* inactivation on adipose-tissue health in animals maintained at 30 °C for the duration of HFD feeding. For these experiments, we followed the same experimental paradigm utilized for the study of *Zfp423* transgenic animals (Extended Data Fig. 6a). Inactivation of *Zfp423* in these cells did not appear to significantly impact body or adiposity over the course of HFD feeding (Extended Data Fig. 6b,c); however, the local adipose-tissue phenotype and systemic consequences were almost perfectly symmetrical to those observed in the corresponding *Zfp423* gain of function model. After 1 month of HFD feeding, the frequencies of gonadal WAT PDGFR $\beta$ <sup>+</sup> subpopulations were comparable between control and Mural-*Zfp423*<sup>KO</sup> mice (Extended Data Fig. 6d). Gene-expression analysis of isolated FIPs and APCs indicated that *Zfp423* expression was significantly diminished in both PDGFR $\beta$ <sup>+</sup> subpopulations in the gonadal WAT from Mural-*Zfp423*<sup>KO</sup> mice (Extended Data Fig. 6e). The reduction in *Zfp423* levels in FIPs led to increased proinflammatory-gene expression in these cells, consistent with the *in vitro* results (Extended Data Fig. 6f). Importantly, inactivation of *Zfp423* in APCs did not lead to increased proinflammatory-gene expression. This might suggest that APCs utilize additional factors to suppress proinflammatory signalling in these cells and/or require the presence of additional molecules to drive the activation of these pathways.

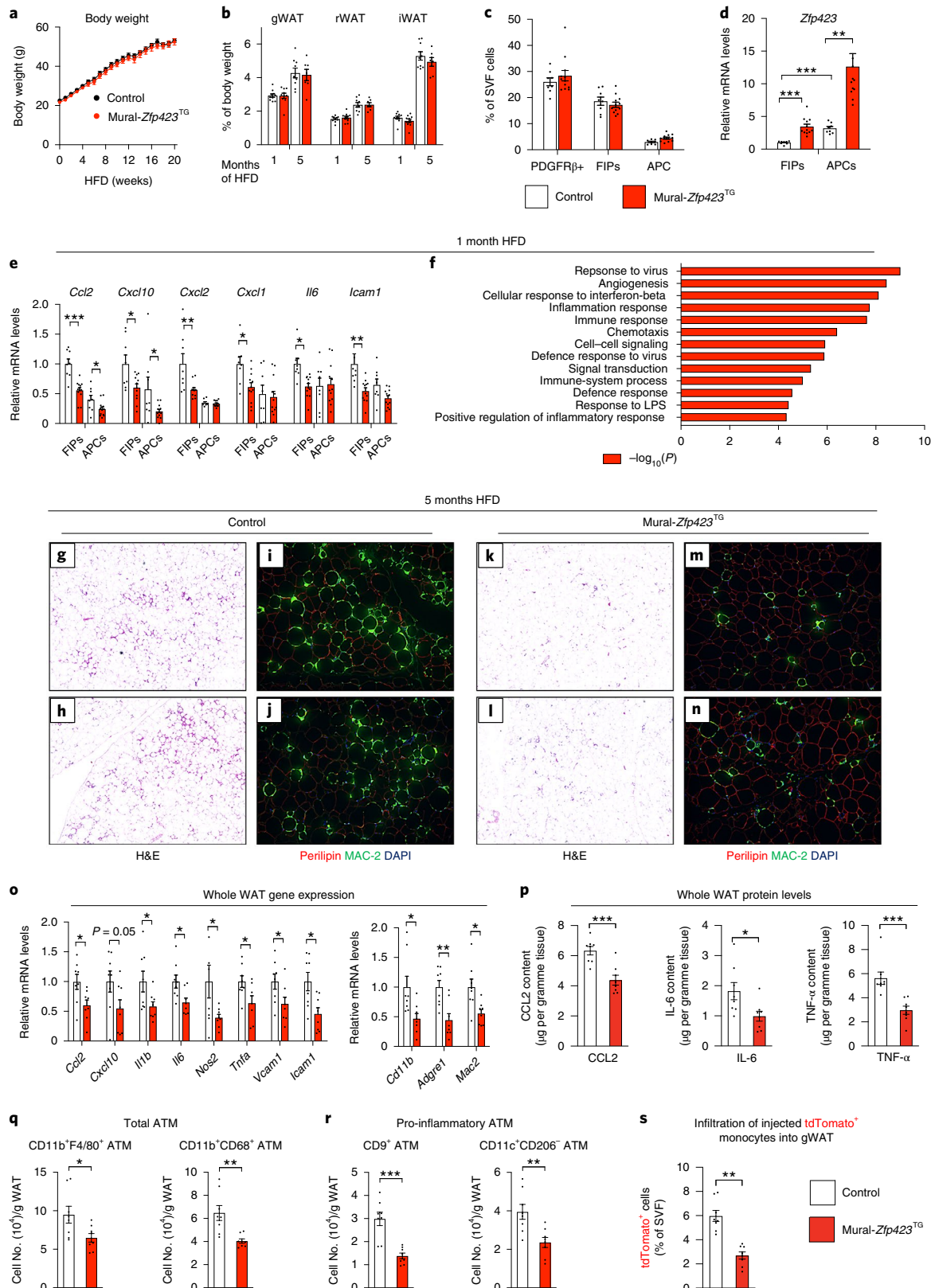
Histological analysis of WAT depots after 5 months of HFD feeding revealed a substantial increase in the degree of inflammation in Mural-*Zfp423*<sup>KO</sup> mice. In comparison with gonadal WAT of control mice, gonadal WAT depots in Mural-*Zfp423*<sup>KO</sup> mice exhibited more MAC-2<sup>+</sup> cells and crown-like structures (Extended Data Fig. 6g–n), higher tissue mRNA levels of several proinflammatory cytokines and adhesion molecules and higher tissue protein levels of CCL2, IL-6 and TNF- $\alpha$  (Extended Data Fig. 6o,p). Moreover, numbers of total and proinflammatory ATMs were approximately twofold higher in gonadal WAT of Mural-*Zfp423*<sup>KO</sup> mice in comparison with controls (Extended Data Fig. 6q,r). Importantly, injected tdTomato<sup>+</sup> monocytes migrate and adopt a macrophage phenotype more readily in obese Mural-*Zfp423*<sup>KO</sup> mice in comparison with obese controls (Extended Data Fig. 6s).

A potential explanation for the pathologic WAT expansion observed in Mural-*Zfp423*<sup>KO</sup> mice could be the development of vascular instability in face of mural cell *Zfp423* inactivation. To test this possibility, we performed Evans blue staining of gonadal and inguinal WAT depots from control and Mural-*Zfp423*<sup>KO</sup> mice that were maintained for 2 months on HFD diet under thermoneutral housing conditions. We chose this 2-month timepoint in order to

**Fig. 6 | *Zfp423* overexpression in PDGFR $\beta$ <sup>+</sup> cells attenuates WAT inflammation in obesity.** **a**, Control ( $n=9$ ; black) and Mural-*Zfp423*<sup>TG</sup> ( $n=7$ ; red) body weights following the onset of HFD feeding at TN. **b**, WAT mass of control and Mural-*Zfp423*<sup>TG</sup> mice after 1 month ( $n=10$  control;  $n=9$  Mural-*Zfp423*<sup>TG</sup>) and 5 months ( $n=9$  control;  $n=7$  for Mural-*Zfp423*<sup>TG</sup>) of HFD feeding. **c**, Frequency of total PDGFR $\beta$ <sup>+</sup> cells, FIPs, and APCs in gonadal WAT of control ( $n=8$ ) and Mural-*Zfp423*<sup>TG</sup> ( $n=12$ ) mice after 1 month of HFD feeding. **d**, *Zfp423* mRNA levels in gonadal WAT FIPs and APCs from control ( $n=8$ ) and Mural-*Zfp423*<sup>TG</sup> ( $n=12$ ) mice after 1 month of HFD feeding. **e**, Proinflammatory-gene expression in gWAT FIPs and APCs from control ( $n=8$ ) and Mural-*Zfp423*<sup>TG</sup> ( $n=12$ ) mice after 1 month of HFD feeding. **f**, Pathway analysis of genes with differential expression (false-discovery rate  $q < 0.05$  and  $\log_2$ (fold change)  $> 0.5$ ) between control and Mural-*Zfp423*<sup>TG</sup> FIPs after 1 month of HFD feeding. **g,h**, Magnified ( $\times 4$ ) images of haematoxylin and eosin (H&E)-stained gonadal WAT from control mice maintained on HFD for 5 months. **i,j**, Magnified ( $\times 10$ ) images of perilipin (red) and MAC-2 (green) expression in gonadal WAT of control mice maintained on HFD for 5 months. **k,l**, Magnified ( $\times 4$ ) images of H&E-stained gonadal WAT from Mural-*Zfp423*<sup>TG</sup> mice maintained on HFD for 5 months. **m,n**, Magnified ( $\times 10$ ) images of perilipin (red) and MAC-2 (green) expression in gonadal WAT of Mural-*Zfp423*<sup>TG</sup> mice maintained on HFD for 5 months. **o**, Proinflammatory- and macrophage-selective-gene expression in gonadal WAT of control ( $n=8$ ) and Mural-*Zfp423*<sup>TG</sup> ( $n=8$ ) mice after 5 months of HFD feeding. **p**, Cytokine protein levels in gonadal WAT of control ( $n=8$ ) and Mural-*Zfp423*<sup>TG</sup> ( $n=8$ ) mice after 5 months of HFD feeding. **q**, Frequency of total ATMs in gonadal WAT of control ( $n=8$ ) and Mural-*Zfp423*<sup>TG</sup> ( $n=8$ ) mice after 5 months of HFD feeding. **r**, Frequency of proinflammatory ATM in gonadal WAT of control ( $n=8$ ) and Mural-*Zfp423*<sup>TG</sup> ( $n=8$ ) mice after 5 months of HFD feeding. **s**, Frequency of tdTomato<sup>+</sup> macrophages in the gonadal WAT SVF of obese mice following injection of tdTomato<sup>+</sup> monocytes.  $n=8$  control and  $n=8$  Mural-*Zfp423*<sup>TG</sup>. Bars represent mean  $\pm$  s.e.m. \* $P < 0.05$ , \*\* $P < 0.01$  and \*\*\* $P < 0.001$  by unpaired two-tailed Student's *t*-test (**o–s**) or one-way ANOVA (**d,e**).

determine whether any changes in vascular permeability precede the overt inflammation that is observed at the 5-month timepoint. Under these conditions, we did not observe any differences in Evans-blue incorporation between the two genotypes (Extended Data Fig. 7a); this suggests that there is no gross difference in the

degree of vascular permeability. We also reassessed the requirement of *Zfp423* in adipocyte differentiation from mural cells in these thermoneutral-housed animals. Consistent with our previous studies, we did not observe any substantial change in the adipogenic potential or levels of *Cebpa* and *Pparg* within APCs when *Zfp423* is



inactivated (Extended Data Fig. 7b,c). After 5 months of HFD feeding, mean adipocyte size and whole-adipose-tissue mRNA levels of adipocyte-selective genes and genes associated with WAT fibrosis were also comparable between obese control and Mural-*Zfp423*<sup>KO</sup> mice (Extended Data Fig. 7d,e). Using lineage tracing, we confirmed that *Zfp423* inactivation did not influence de novo adipogenesis in these depots of obese Mural-*Zfp423*<sup>KO</sup> mice (Extended Data Fig. 7f–h). Altogether, these data support the notion that the increased adipose-tissue inflammation in Mural-*Zfp423*<sup>KO</sup> mice is probably mediated by the loss of the anti-inflammatory function of ZFP423 in PDGFR $\beta$ <sup>+</sup> cells, rather than by detrimental effects on vascular integrity or the perivascular progenitor-cell compartment.

The local and systemic effects of inactivating *Zfp423* in PDGFR $\beta$ <sup>+</sup> cells at the onset of HFD feeding were also perfectly symmetrical to the effects observed in the *Zfp423*-transgenic model. Increased pro-inflammatory macrophage accrual in WAT of Mural-*Zfp423*<sup>KO</sup> mice was associated with impairments in insulin-stimulated AKT phosphorylation in WAT (Extended Data Fig. 8a). Moreover, in comparison with control animals, Mural-*Zfp423*<sup>KO</sup> mice were more glucose intolerant and insulin resistant (Extended Data Fig. 8b,c). Consistent with these observations, levels of adiponectin were lower, and serum insulin and CCL2 levels were higher, in Mural-*Zfp423*<sup>KO</sup> mice than in controls (Extended Data Fig. 8d,e). Similar to what was observed in the *Zfp423*-transgenic mice, these phenotypes occurred without any substantial impact on the expression of macrophage-selective genes within the skeletal muscle and liver (Extended Data Fig. 8f,g), or changes in the amount of monocytes in the blood, bone marrow or spleen (Extended Data Fig. 8h–j). These loss-of-function data provide additional evidence that *Zfp423* exerts an anti-inflammatory function in adipose PDGFR $\beta$ <sup>+</sup> cells, and further suggest that the activation of proinflammatory signalling cascades in mural cells can heavily influence adipose-tissue health in obesity.

**ZFP423 represses the transcriptional activity of NF- $\kappa$ B.** As described above, cultured FIPs and APCs differ in their ability to respond to the genetic activation of NF- $\kappa$ B signalling. This prompted us to ask whether the molecular mechanism by which ZFP423 exerted its anti-inflammatory effect involved modulation of this pathway. We reconstituted the TRE-*Zfp423* transgene into the Mural-*Ikk2*<sup>CA</sup> background to derive animals in which the addition of doxycycline leads to the expression of both IKK2<sup>CA</sup> and ZFP423 (Mural-*Ikk2*<sup>CA</sup>/*Zfp423*<sup>TG</sup> mice) (Extended Data Fig. 9a). Remarkably, a modest two- to threefold increase in the mRNA levels of *Zfp423* in isolated FIPs was sufficient to almost fully suppress all of IKK2<sup>CA</sup>-induced NF- $\kappa$ B transcriptional targets examined (Extended Data Fig. 9b,c). We also derived an additional model in which the floxed *Zfp423* alleles were incorporated into the Mural-*Ikk2*<sup>CA</sup> background. The addition of doxycycline thus led to the simultaneous expression of IKK2<sup>CA</sup> and inactivation of *Zfp423* alleles (Mural-*Ikk2*<sup>CA</sup>/*Zfp423*<sup>KO</sup> mice) (Extended Data Fig. 9d, e). Isolated *Zfp423*-deficient FIPs from this model show an exaggerated transcriptional response to the activation of NF- $\kappa$ B signalling by IKK2<sup>CA</sup> expression (Extended Data Fig. 9f). These data suggest that ZFP423 suppresses the transcriptional activity of NF- $\kappa$ B. We performed NF- $\kappa$ B-dependent gene reporter assays in commercially available HEK 293 cells engineered to stably express TLR signalling components, which mediate LPS-induced proinflammatory responses (herein 293-TLR4 cells). The 293-TLR4 cells responded to LPS with a robust activation of the NF- $\kappa$ B-dependent reporter gene (Fig. 7a). Overexpression of *Zfp423* in these cells diminished the activation of the NF- $\kappa$ B-dependent gene reporter by more than twofold, providing evidence that ZFP423 indeed regulates the activity of NF- $\kappa$ B (Fig. 7a).

NF- $\kappa$ B, consisting of the p50 and p65 protein subunits, is highly regulated at the post-translational level<sup>20</sup>. Under basal conditions, I $\kappa$ B $\alpha$  is bound to p50/p65 to mediate cytoplasmic sequestration of

the protein complex. Proinflammatory signals trigger I $\kappa$ B $\alpha$  degradation, allowing p50–p65 to enter the nucleus to activate transcription. This pathway is operative in FIPs from control mice. LPS treatment leads to rapid degradation of I $\kappa$ B $\alpha$  and nuclear localization of p65. Analysis of cultured FIPs from Mural-*Zfp423*<sup>TG</sup> mice indicates that neither I $\kappa$ B $\alpha$  degradation nor nuclear localization of p65 are overtly impacted by *Zfp423* overexpression (Fig. 7b and Supplementary Fig. 5). The p65 subunit of NF- $\kappa$ B is also highly regulated by post-translational modifications, including protein acetylation<sup>21,22</sup>. In response to LPS treatment, p65 acetylation is pronounced in FIPs from control mice; however, under the same conditions, levels of acetylated p65 are strongly reduced in *Zfp423*-overexpressing FIPs (Fig. 7b). These data indicate that the presence of ZFP423 impacts NF- $\kappa$ B signalling at the level of p65 acetylation.

Acetylation of p65 is mediated, at least in part, through interaction with CBP/p300. Acetylation of p65 can impact DNA binding and/or transcriptional activity and enhancer selectivity<sup>20</sup>. As such, we tested whether p65 binding to its target loci would be impacted in cells overexpressing *Zfp423*. We utilized chromatin immunoprecipitation with sequencing (ChIP-seq) to assess genome-wide p65 occupancy in LPS-treated FIPs from control and Mural-*Zfp423*<sup>TG</sup> mice (Supplementary Fig. 6a). Our analysis identified 26,377 regions occupied by p65 in LPS-treated FIPs from control mice (Fig. 7c and Supplementary Table 5). Computational analysis confirmed the enrichment of NF- $\kappa$ B (p65) binding motifs in these regions (Supplementary Fig. 6b). Remarkably, the p65 occupancy at target loci was reduced globally in LPS-treated *Zfp423*-expressing FIPs (Fig. 7c). We validated these data in independent p65 ChIP experiments using PCR primers spanning predicted p65 response elements proximal to key inflammatory cytokine genes (Fig. 7d). ChIP, followed by PCR analysis, confirmed the presence of p65 at these individual loci within control FIPs, with a significant reduction in occupancy within FIPs of Mural-*Zfp423*<sup>TG</sup> mice (Fig. 7e). Thus, ZFP423 expression leads to a disruption of NF- $\kappa$ B binding to target loci in FIPs.

**ZFP423 induces a NF- $\kappa$ B coregulator switch in FIPs.** ZFP423 contains 30 C2H2 zinc-finger motifs that mediate interactions with many notable transcription factors. In an effort to understand how ZFP423 might impact p65 protein acetylation, we sought to identify ZFP423-interacting partners in an unbiased manner by employing affinity purification of ZFP423 complexes and mass-spectrometry analysis (Supplementary Fig. 7a). For the initial experiment, we transiently transfected HEK 293 cells with plasmid encoding FLAG-tagged ZFP423 protein. Liquid chromatography with tandem mass spectrometry analysis revealed the presence of all core components of the nucleosome remodelling deacetylase (NuRD) corepressor complex in association with ZFP423 (Supplementary Fig. 7b,c and Supplementary Table 6). This complex includes several chromatin-remodelling factors, (CHD4, MTA1, MTA2, RBAP46, RBAP48 and MBD3) along with histone deacetylases 1 and 2 (HDAC1 and HDAC2)<sup>23</sup>. Prior studies of NuRD-interacting proteins identified a consensus ‘NuRD-interaction domain (NID)’, which consists of 12 amino acids (aa) that directly interact with the RBAP48 subunit of the NuRD complex<sup>24</sup>. The 12-aa motif is present in a number of C2H2 finger transcription factors, including the amino terminus of ZFP423 (Fig. 8a). All core components of the NuRD complex are readily detected by western-blot analysis of primary FIPs (Supplementary Figs. 7d and 8). Endogenous NuRD components associate with virally expressed FLAG–ZFP423 protein in FIPs, but not with a FLAG-tagged variant of ZFP423 that is expressed but lacks the 12-aa NID (FLAG–ZFP423<sup>ΔNID</sup>) (Supplementary Fig. 7d). These data validate the mass-spectrometry dataset and confirm that the ZFP423–NuRD interaction can occur in FIPs. Interestingly, we found that endogenous p65 protein is physically associated with the NuRD complex in a ZFP423- and LPS-dependent manner (Fig. 8b).

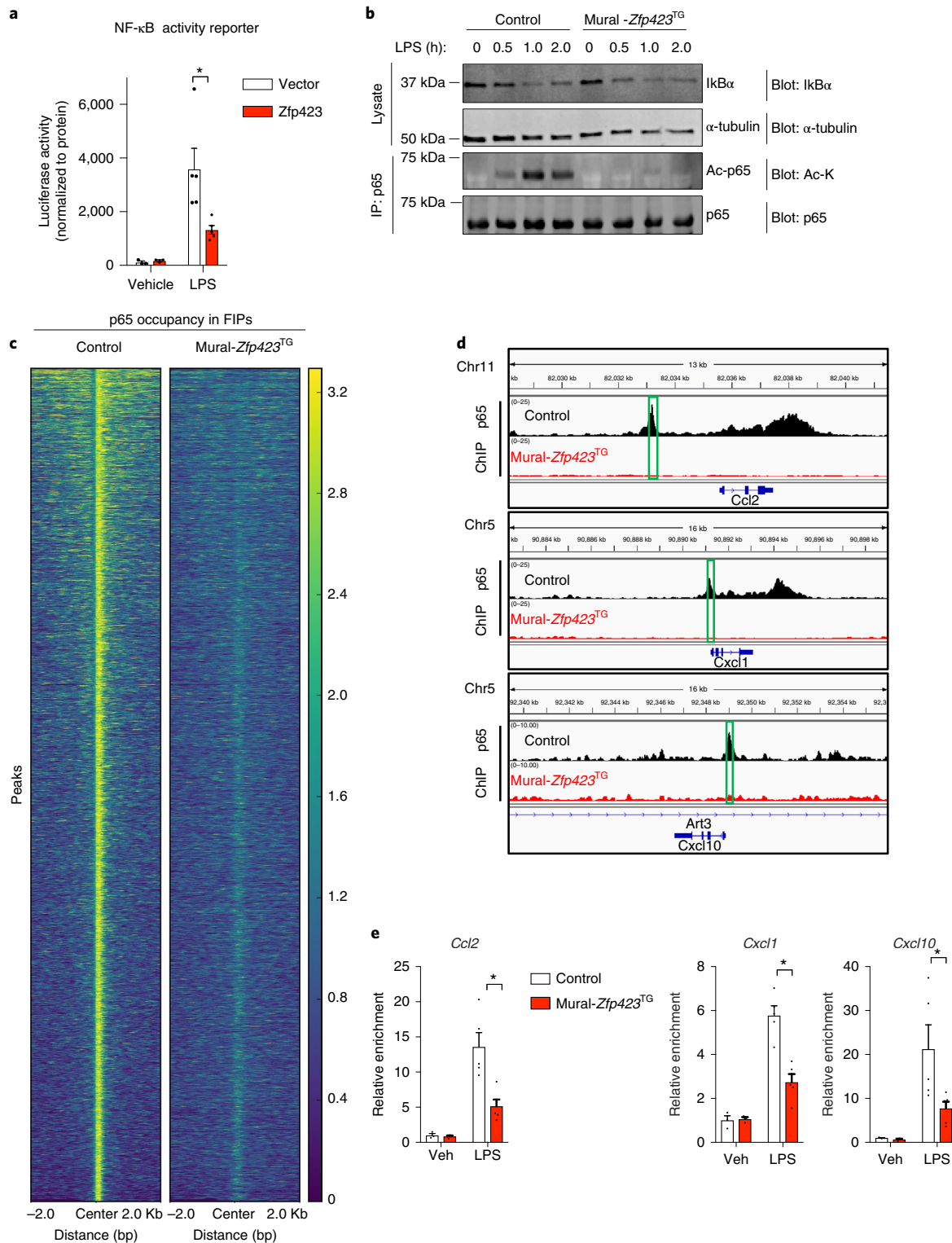


**Fig. 7 | ZFP423 suppresses the DNA-binding capacity and activity of NF- $\kappa$ B in FIPs.** **a**, NF- $\kappa$ B-dependent luciferase gene reporter activity in 293-TLR4 cells cotransfected with *Zfp423*-expressing vector (*Zfp423*) or empty vector (Vector). Cells were treated with LPS (100 ng ml<sup>-1</sup>) ( $n=5$  per group) or vehicle (PBS) ( $n=3$  per group) for 8 h prior to collection. **b**, Western blot analysis of IkB $\alpha$ , acetylated lysine (Ac-K) and total p65 levels in whole-cell lysates or p65 immunoprecipitates from control and Mural-*Zfp423*<sup>TG</sup> FIPs treated with LPS (100 ng ml<sup>-1</sup>) for indicated times.  $\alpha$ -tubulin was used as an internal control for protein loading. **c**, Heat map illustrating p65-occupied regions in control and Mural-*Zfp423*<sup>TG</sup> FIPs following LPS treatment. **d**, p65 enrichment at *Ccl2*, *Cxcl1* and *Cxcl10* loci in control and Mural-*Zfp423*<sup>TG</sup> FIPs treated with 100 ng ml<sup>-1</sup> LPS for 2 h. Green boxes indicate the putative p65 binding motif (GGGRNYYYCC) containing regions targeted by ChIP-qPCR primers. **e**, Confirmation of ChIP-seq data by ChIP-PCR. qPCR analysis of p65 occupancy at indicated loci in control and Mural-*Zfp423*<sup>TG</sup> FIPs treated with 100 ng ml<sup>-1</sup> LPS for 2 h. PCR primers spanning the green boxed regions indicated in **d** were used.  $n=3$  for vehicle group;  $n=5$  for LPS group. Each sample ( $n$ ) represents individual p65 chromatin immunoprecipitation from ~1,000,000 cells of 8 mice. For **a** and **e**, data are shown as the mean  $\pm$  s.e.m., \* $P < 0.05$  by two-way ANOVA.

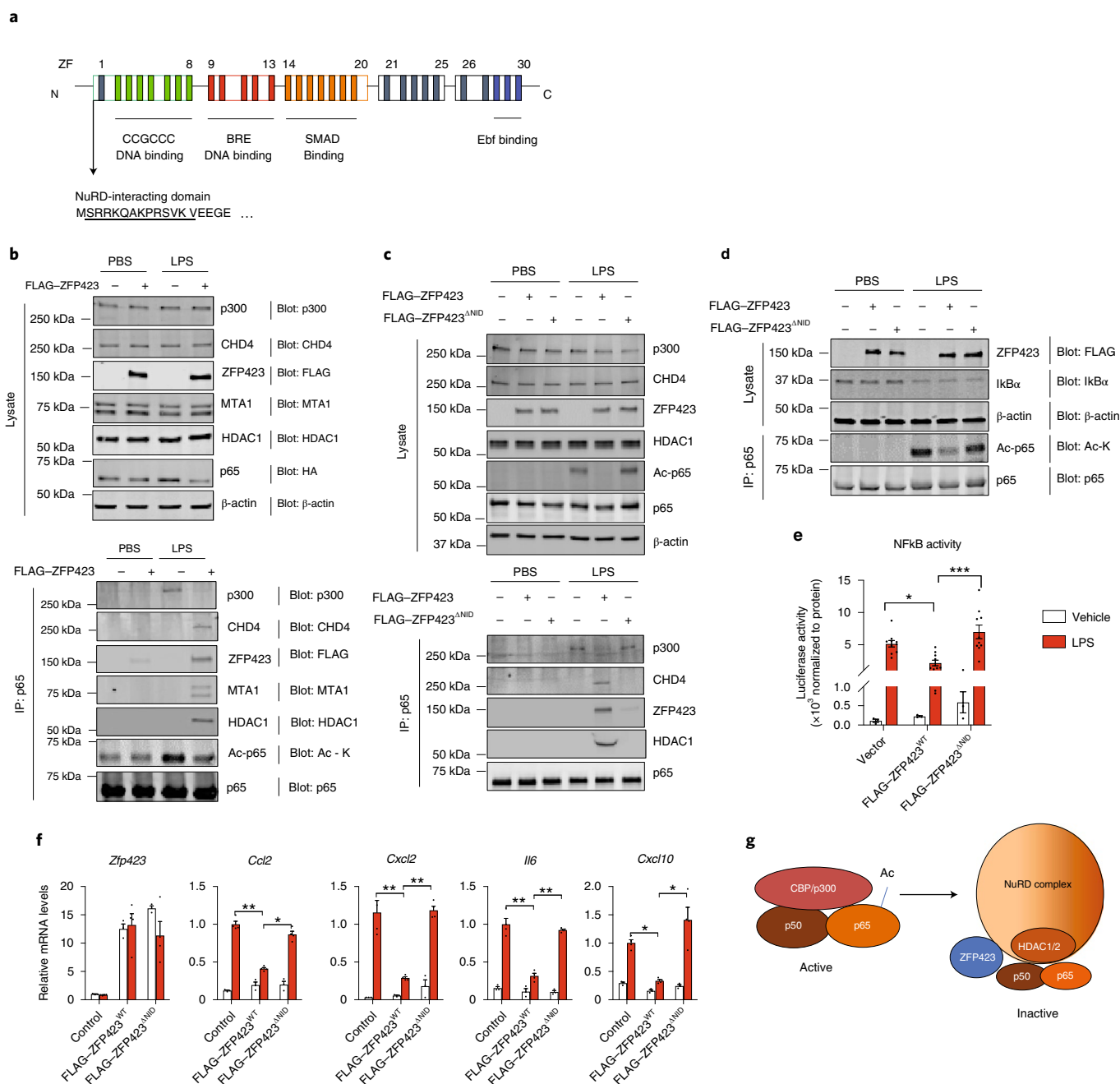


**Fig. 8 | ZFP423 induces a NF- $\kappa$ B p65 coregulator switch.** **a**, Schematic of ZFP423. ZFP423 contains 30 C2H2 zinc-fingers (ZF) clustered into five domains. Amino acids 2–13 represent a defined NuRD-interaction domain that resides within numerous zinc-finger proteins that interact directly with the NuRD corepressor complex. **b**, Western blot of indicated protein expression in FIP whole-cell lysates (left) and p65 immunoprecipitates (right) from primary FIPs transduced with control retrovirus or retrovirus expressing FLAG-ZFP423. Cells were treated with LPS (100 ng ml<sup>-1</sup>) or vehicle for 2 h prior to collection. **c**, Western blot of the indicated protein expression in FIP whole-cell lysates (top) and p65 immunoprecipitates (bottom) from primary FIPs transduced with control retrovirus or retrovirus expressing FLAG-ZFP423 or FLAG-ZFP423<sup>ΔNID</sup>. Cells were treated with LPS (100 ng ml<sup>-1</sup>) or vehicle for 2 h prior to collection. **d**, Western blot of indicated protein expression in whole-cell lysates of FIPs transduced with control retrovirus, wild-type FLAG-tagged ZFP423 (FLAG-ZFP423<sup>WT</sup>) or retrovirus expressing FLAG-ZFP423 lacking the 12-aa NuRD-interaction domain (FLAG-ZFP423<sup>ΔNID</sup>) and treated with LPS (100 ng ml<sup>-1</sup>) or vehicle.  $\beta$ -actin expression was used as loading control. **e**, NF- $\kappa$ B-dependent gene-reporter activity in 293-TLR4 cells cotransfected with control, FLAG-ZFP423<sup>WT</sup> or FLAG-ZFP423<sup>ΔNID</sup> plasmids. Cells were treated with LPS (100 ng ml<sup>-1</sup>) ( $n = 10$  per group) or vehicle (PBS) ( $n = 3$  per group) for 8 h prior to collection. Bars represent mean  $\pm$  s.e.m.  $*P < 0.01$  by two-way ANOVA. **f**, mRNA levels of indicated genes in FIPs transduced with control, FLAG-ZFP423<sup>WT</sup> or FLAG-ZFP423<sup>ΔNID</sup> retroviruses and treated with vehicle (PBS) ( $n = 3$  per group) or 100 ng ml<sup>-1</sup> LPS ( $n = 4$  per group) for 2 h.  $*P < 0.05$ ,  $**P < 0.01$  by two-way ANOVA. **g**, Proposed model. The nuclear p65 subunit of NF- $\kappa$ B is acetylated (Ac) and activated by its interaction with CBP/p300. The presence of ZFP423 triggers a transcriptional coregulator switch; ZFP423 facilitates the recruitment of the NuRD corepressor complex to p65, thereby excluding CBP/p300 association and p65 acetylation.

In cells overexpressing ZFP423, LPS no longer triggers a p65–p300 interaction. Instead, p65 is associated with ZFP423 and the NuRD complex (Fig. 8b). Thus, ZFP423 expression appears to mediate a p65 coregulator switch in FIPs. The NID is essential for the ability of ZFP423 to exert these inhibitory effects on NF- $\kappa$ B signalling. FLAG–ZFP423<sup>ΔNID</sup> does not interact with p65 in FIPs (Fig. 8c), induce a p300–NuRD coregulator switch (Fig. 8c), or block p65 acetylation (Fig. 8d). Moreover, ZFP423<sup>ΔNID</sup> is unable to inhibit NF- $\kappa$ B reporter activity (Fig. 8e) or suppress proinflammatory-gene expression in these cells (Fig. 8f). ChIP-seq analysis of CHD4, an obligate component of the NuRD complex, did not reveal an increased level of occupancy at p65 target loci in ZFP423-expressing cells (Supplementary Fig. 6c,d). Thus, it does not appear that the ZFP423–NuRD complex is necessarily replacing p65/p300 at target loci, but instead might be tethering the active p65 complex away from DNA. Collectively, these data suggest a model in which ZFP423 suppresses NF- $\kappa$ B signalling by triggering a p65 coregulator switch: ZFP423 expression leads to the recruitment of the NuRD corepressor complex to p65, with a concomitant loss of coactivator (p300) recruitment, p65 acetylation and p65 DNA-binding capacity (Fig. 8g).

## Discussion

The data here highlight an important role for perivascular mesenchymal cells in the regulation of adipose-tissue inflammation and health. Our studies identify FIPs as a specialized subpopulation of perivascular cells that are functionally distinct from APCs and differentially regulated in association with physiological settings of metabolic inflammation. We propose a model in which FIPs serve, in part, as critical regulators of macrophage accrual in obesity (Extended Data Fig. 10). In lean mice, FIPs appear to maintain some basal inflammatory signalling. The presence of ZFP423 might serve to moderate NF- $\kappa$ B activity in order to maintain inflammatory balance. In response to HFD feeding, the downregulation of *Zfp423* expression facilitates further activation of NF- $\kappa$ B signalling and the induction of proinflammatory-gene expression. The congruence of the phenotypes of the various mouse models presented here support the underlying hypothesis that proinflammatory signalling events in perivascular mesenchymal cells significantly impact chronic WAT inflammation in obesity.

FIPs exert a proinflammatory response and phenotype within 1–3 d of HFD, likely placing them among the earliest of responders in WAT. Going forward, a tremendous challenge will be in identifying the factors associated with HFD feeding that trigger the activation of FIPs. A number of possible triggers could activate a proinflammatory response in WAT<sup>25</sup>. This includes gut-derived antigens (for example LPS), dietary lipids, hypoxia and even mechanical stress. Furthermore, it will be of interest to understand whether and how other cells types, particularly adipocytes, coordinate this response with FIPs.

The proinflammatory phenotype of FIPs is dependent on TLR4 signalling, a key mediator of proinflammatory responses to LPS and other stimuli. Mice lacking *Tlr4* are protected from diet-induced insulin resistance and inflammation; however, which *Tlr4*-expressing cells mediate this effect have been unknown. Tissue-specific knockout models have highlighted hepatocyte TLR4 signalling as a key mediator of metabolic inflammation and insulin resistance<sup>26</sup>. On the other hand, adipocyte TLR4 signalling is more complex and might even be beneficial for appropriate WAT expansion in obesity<sup>27</sup>. Our studies here highlight TLR4 signalling in perivascular stromal cells as an important mediator of proinflammatory macrophage accumulation in WAT.

ZFP423 appears to be among a select group of transcriptional components that safeguard against hyperinflammatory responses<sup>28–30</sup>. The downregulation of *Zfp423* at the onset of HFD could thus represent a mechanism through which FIPs can activate their proinflammatory phenotype. It is notable that the activation

of NF- $\kappa$ B signalling in FIPs via IKK2<sup>CA</sup> expression led to a downregulation of *Zfp423* expression (Extended Data Fig. 9b,e). This suggests that ZFP423 and NF- $\kappa$ B could be part of a regulatory loop that maintains inflammatory balance in these cells. *Zfp423* is also expressed in various regions of the brain, proliferating muscle satellite cells and endothelial cells<sup>12,31–34</sup>. Whether ZFP423 exerts an anti-inflammatory function in other tissues is unclear. The presence of such tissue-selective modifiers of NF- $\kappa$ B signalling might allow for spatial control of inflammatory responses in the body.

The p65 subunit of NF- $\kappa$ B is heavily regulated by phosphorylation and acetylation. The latter plays an important role in enhancing the DNA-binding capacity and/or transcriptional activity of p65. CBP/p300 is a well-characterized acetyltransferase for p65, whereas HDAC3 and SIRT1 are among the known deacetylases of the protein<sup>20,29,35,36</sup>. Our biochemical data suggest a model in which ZFP423 expression leads to the recruitment of the NuRD corepressor complex to p65. The NuRD repressor complex contains HDAC1 and HDAC2; however, prior studies have suggested that these proteins do not directly mediate p65 deacetylation. As such, it is likely that ZFP423 is mediating a coregulator switch in which the presence of the NuRD complex displaces CBP/p300 from p65 to limit its activation. In accordance with this model, an engineered variant of mouse ZFP423 lacking the NuRD-interaction domain is unable to suppress NF- $\kappa$ B activity and the proinflammatory phenotype of FIPs.

A limitation to our study is the inability to specifically target subpopulations of PDGFR $\beta$ <sup>+</sup> cells in mice. The *Pdgfrb*<sup>rtTA</sup> allele targets both FIPs and APCs; however, it should be noted that FIPs represent a vast majority of all PDGFR $\beta$ <sup>+</sup> cells in WAT. FIPs are naturally more proinflammatory than are APCs, and the most robust changes in proinflammatory-gene expression occur in FIPs rather than APCs following *Tlr4* or *Zfp423* manipulation. Furthermore, visceral WAT APCs retain their normal differentiation capacity following loss or gain of *Zfp423* function in these cells. Importantly, we did not observe substantial changes in proinflammatory responses in non-adipose tissues of our models following LPS treatment or HFD feeding. These data suggest that the manipulation of *Tlr4* or *Zfp423* levels in PDGFR $\beta$ <sup>+</sup> cells did not elicit broad inflammatory effects, but rather local impacts on WAT inflammation. Our work highlights a maladaptive mechanism by which FIPs are activated in adipose tissue to promote chronic metabolic inflammation; however, these data cannot exclude a role for these cells in lean animals, perhaps serving in the homeostatic control of adipose-tissue mass and function. FIPs also express IL-33, a key cytokine important in maintaining an anti-inflammatory state in WAT<sup>37,38</sup>. A deeper understanding of the heterogeneity of adipose stromal cells might identify additional mechanisms controlling both physiological WAT homeostasis and pathophysiological expansion of fat tissue in the face of caloric excess. Deciphering such mechanisms could inform new strategies to improve WAT health and uncouple the development of metabolic disease from obesity.

## Methods

**Animals.** All animal experiments were performed according to procedures approved by the UTSW Institutional Animal Care and Use Committee. *Pdgfrb*<sup>rtTA</sup> transgenic mice (C57BL/6-Tg(Pdgfrb-rtTA)58GptA/J; JAX028570; RRID: IMSR\_JAX:028570), *TRE-Cre* (B6.Cg-Tg(tetO-cre)1Jaw/J; JAX 006234; RRID:IMSR\_JAX:006234), and *Rosa26*<sup>IKK2CA</sup> (B6(Cg)-Gt(ROSA)26Sor<sup>tm4(Ikk2b)Rskj</sup>/J; JAX008242) mice were obtained from Jackson Laboratories. *Zfp423*<sup>oxsp/oxsp</sup> mice have previously been described<sup>15</sup> and were generously provided by S. Warming (Genentech). *Tlr4*<sup>loxP/loxP</sup> mice were generated at UTSW and previously described<sup>426</sup>. *TRE-Zfp423* transgenic mice were derived by the UTSW Transgenic Core Facility and have previously been described<sup>17</sup>. The animals used in this study were all male mice on a pure C57BL/6 background. The mice were maintained on a 12-h light–dark cycle in a temperature-controlled environment (room temperature, 22°C; thermoneutrality, 30°C) and given free access to water and food.

**Rodent diets and drug treatments.** Mice were maintained on a standard rodent chow diet or chow diet containing 600 mg per kg (body weight) doxycycline (Bio-Serv, no. S4107). For thermoneutrality experiments, mice were housed

in a thermoneutral chamber (30 °C) beginning at the age of 6 weeks and were maintained on a standard chow diet for 2 weeks before being switched to the indicated HFDs. For HFD studies, mice (8 weeks old) were fed a standard HFD (HFD; 60% kcal fat; Research Diets no. D12492i) or doxycycline-containing HFD (600 mg per kg (body weight) doxycycline, 60% kcal fat, Bio-Serv, no. S5857) as described in the main text. For lipopolysaccharide administration, mice were intraperitoneally (i.p.) injected with vehicle (PBS) or LPS (0.3 mg per kg body weight; Sigma, no. L3024) and euthanized after 2 h or 24 h as indicated in the main text.

**Serum measurements.** Serum levels of adiponectin and insulin were measured using the mouse adiponectin ELISA (Millipore, no. EZMADP-60K) and mouse insulin ELISA kit (Crystal Chem, no. 90080), respectively. Assays were performed according to manufacturer instructions.

**Histological analysis.** Dissected tissues were fixed in freshly prepared 4% paraformaldehyde for 48 h and then maintained in 50% ethanol solution. Paraffin embedding, sectioning and H&E staining were conducted by the Molecular Pathology Core Facility at UT Southwestern. Brightfield and fluorescent images were acquired using a Keyence BZ-X710 microscope. Adipocyte size was measured as previously described<sup>18</sup>. In brief, brightfield images of H&E-stained paraffin sections were analysed using Keyence BZ-X Analyzer software. More than 200 adipocytes were quantified in each individual animal.

**Indirect immunofluorescence.** Indirect immunofluorescence was performed as previously described<sup>13</sup>. Antigen retrieval of the rehydrated sections was performed using Antigen Retriever 2100 (Electron Microscopy Sciences) and R-Buffer A pH 6.0 solution (Electron Microscopy Sciences, no. 62706). For GFP immunostaining, animals were perfused with 4% PFA before dissection. For quantification of adipocyte hyperplasia, an indirect immunofluorescence assay of perilipin and GFP expression was performed as previously described<sup>15</sup>. Cell numbers of perilipin<sup>+</sup>GFP<sup>+</sup> and perilipin<sup>+</sup>GFP<sup>-</sup> adipocytes were counted on 8 randomly selected magnified (×10) images of stained WAT depots. A total of 3,000–4,000 perilipin<sup>+</sup> adipocytes were counted for each mouse, and each data point represents the percentage of perilipin<sup>+</sup> adipocytes expressing GFP adipocytes. Antibodies and concentrations used for immunofluorescence include: guinea pig anti-perilipin 1:1,000 (Fitzgerald no. 20R-PP004); rabbit anti-MAC-2 1:500 (Cedarlane, Clone M3/38, no. CL8942AP); chicken anti-GFP 1:500 (Abcam, no. ab13970); goat anti-guinea pig Alexa Flour 647 1:200 (Invitrogen, no. A21450); goat anti-rat Alexa Flour 488 1:200 (Invitrogen, no. A11006); goat anti-chicken Alexa Flour 488 1:200 (Invitrogen, no. A11039).

**Evans blue staining.** Vascular permeability of white adipose tissue was determined by Evans-blue injection as previously described<sup>19</sup>. In brief, the mice were injected with 160 mg per kg (body weight) Evans-blue dye (Sigma, no. E2129) via tail vein. Thirty minutes after injection, the mice were anaesthetized and then perfused with PBS. Collected whole gonadal and inguinal-fat depots were fixed in 4% PFA overnight. Rinsed fat pads (PBS) were imaged for Evans-blue autofluorescence at 700 nm using a LI-COR Odyssey infrared imaging system.

**Gene-expression analysis by qPCR.** Total RNA from tissue and cultured cells was extracted and purified using the TRIzol reagent (Invitrogen, no. 15966026). Total RNA from freshly FACS-sorted cells was extracted and purified using the RNAqueous-Micro Total RNA isolation kit (Thermo Fisher Scientific, no. AM1931). Complementary DNA was synthesized using random hexamer primers (Thermo Fisher Scientific, no. N8080127) and M-MLV reverse transcriptase (Thermo Fisher Scientific, no. 28025013). Relative levels of mRNAs were determined by real-time qPCR using SYBR Green PCR system (Applied Biosystems), and *Rps18* was used as an internal control for calculation using the 2<sup>-C<sub>q</sub></sup> method. All primers sequences used in this study are listed in Supplementary Table 7.

**Isolation of adipose SVF and flow-cytometric assays.** The SVF of white adipose tissue was isolated as previously described<sup>18</sup>. Briefly, minced gonadal white-fat depots were incubated for 1 h in digestion buffer (1× HBSS, 1.5% BSA and 1 mg ml<sup>-1</sup> collagenase D (Roche, no. 11088882001)) at 37 °C in a shaking water bath. The digested mixture was sequentially filtered through a 100-µm cell strainer and then a 40-µm cell strainer. The red blood cells in SVFs were lysed by short incubation in 1 ml 1×RBC lysis buffer (eBioscience, no. 00-4300-54), and the SVF cells were then resuspended in blocking buffer (2% FBS/PBS containing anti-mouse CD16/CD32 Fc Block 1:200). For FACS isolation of FIPs and APCs, primary antibodies were added to the cells in blocking buffer for 15 min while being incubated at 4 °C. The cells were then washed once and resuspended in 2% FBS/PBS before sorting. FACS was performed using a BD Biosciences FACSARIA cytometer at the Flow Cytometry Core Facility at UT Southwestern. The primary antibodies and the working concentrations were as following: CD45–PerCP/Cyanine 5.5 1:400 (Biolegend, clone 30-F11, no. 103132), CD31–PerCP/Cyanine 5.5 1:400 (Biolegend, clone 390, no. 102420), PDGFRβ-PE 1:75 (Biolegend, clone APB5, no. 136006), LY6C–APC 1:400 (Biolegend, clone HK1.4, no. 128016), CD9–FITC 1:400 (Biolegend, clone MZ3, no. 124808).

For the analysis of adipose-tissue macrophages, isolated SVF cells were incubated with flow antibodies for 1 h at 4 °C. The primary antibodies and the working concentrations were as following: CD45–PerCP/Cyanine5.5 1:400 (Biolegend, clone 30-F11, no. 103132), CD11b–Pacific Blue 1:200 (Biolegend, clone M1/70, no. 101224), F4/80-PE 1:200 (Biolegend, clone BM8, no. 123110), CD11c–APC 1:200 (Biolegend, clone N418, no. 117310), CD206–FITC 1:200 (Biolegend, clone C068C2, no. 124808), CD68–FITC 1:200 (Biolegend, clone FA-11, no. 137005), CD68–APC 1:200 (Biolegend, clone FA-11, no. 137007), CD9–FITC 1:400 (Biolegend, clone MZ3, no. 124808). For the analyses of monocytes in blood, PBMCs were prepared using Histopaque-1077 (Sigma, no. 10771), according to the manufacturer's instructions. Meanwhile, cells were prepared from bone marrow and spleen for monocytes analysis. The cells were incubated with flow antibodies for 1 h at 4 °C. The primary antibodies and the working concentrations were as following: CD45–PerCP/Cyanine5.5 1:400 (Biolegend, clone 30-F11, no. 103132), CD11b–Pacific Blue 1:200 (Biolegend, clone M1/70, no. 101224), CD115–APC/Cyanine7 1:200 (Biolegend, clone AFS98, no. 135531), LY6C–APC 1:400 (Biolegend, clone HK1.4, no. 128016). After being washed twice with 2% FBS/PBS, cells were fixed by incubation with BD Cytofix (BD Biosciences, no. 554655) for >30 min. Flow-cytometry analysis was performed using a BD Biosciences LSR Fortessa. All the flow-cytometry datasets were analysed and graphed using FlowJo Version 10.6.1. Detailed information of commercial manufacturers and validation of the antibodies can be found in the Reporting Summary.

**Cellular assays. Culture of PDGFRβ<sup>+</sup> subpopulations.** Freshly isolated FIPs and APCs were cultured in previously defined ITS medium, consisting of 60% low-glucose DMEM, 40% MCDB-201 medium, 2% FBS, 1% ITS premix (Insulin–Transferrin–Selenium) (BD Biosciences, no. 354352), 0.1 mM L-ascorbic acid-2-phosphate (Sigma, no. A8960-5G), 10 ng ml<sup>-1</sup> FGF basic (R&D systems, no. 3139-FB-025/CF), penicillin–streptomycin and gentamicin. For gain-of-function cellular studies, cultures from control and Mural-*Zfp423*<sup>tg</sup> mice were incubated with doxycycline (1 µg ml<sup>-1</sup>) in ITS medium for more than 24 h before beginning treatment. For loss-of-function studies in vitro, PDGFRβ<sup>+</sup> cells were isolated from control and Mural-*Zfp423*<sup>ko</sup> mice maintained on doxycycline-containing chow diet for 10 d and then placed in culture.

**Adipocyte differentiation.** For adipogenesis assays, sorted primary cells were plated in 48-well plates at a density of 4 × 10<sup>4</sup> cells per well in ITS medium containing 2% FBS (Millipore, no. TMS-013-B) and incubated at 37 °C in 10% CO<sub>2</sub> for 7 d. Medium was replaced every other day. APCs differentiate spontaneously into adipocytes on reaching confluence.

**LPS and palmitate treatment of cells.** FIPs were plated in 24-well plates at 5 × 10<sup>5</sup> cells per well in ITS medium containing 2% endotoxin-free FBS (GIBICO, no. 16000-044) and were cultured until the cells reached confluence. After overnight incubation with serum-free ITS medium, the cells were treated with 100 ng ml<sup>-1</sup> LPS (PBS was used as vehicle control) or 0.5 mM palmitate (Sigma, no. P9676; BSA was used as vehicle control) for 2 h before collection for RNA isolation.

**Preparation of FIP conditioned medium.** FIPs were isolated from gonadal WAT of wild-type C57BL/6 male mice maintained on HFD for 0 d (chow diet), 1 d, 3 d or 7 d and then plated in 24-well plates (1 × 10<sup>5</sup> cells/well) containing serum-free ITS media. Twenty-four hours after plating, conditioned medium was collected. For conditioned medium derived from LPS-treated cells, FIPs were first maintained in serum-free ITS medium overnight and then treated with 100 ng ml<sup>-1</sup> LPS for 3 h. After 3 washes with PBS (to remove LPS), cells were replaced with fresh serum-free ITS medium and incubated for 24 h. After 24 h, medium was collected and briefly centrifuged (3,000g for 15 min) to remove debris. For all experiments, conditioned medium was mixed 1:1 with fresh serum-free ITS medium before being placed on target cells.

**Macrophage differentiation and assays.** BMDMs used in this study were derived from bone marrow stem cells (BMSCs) isolated from the femurs and tibias of male mice as previously described<sup>40</sup>. To induce the differentiation of mature macrophages, BMSCs were maintained in L929 cell-derived differentiation medium for 7 d. Mature BMDMs were maintained in 2% FBS-containing ITS medium for at least 24 h, and then switched to serum-free ITS medium for more than 6 h before further experiments. For conditioned medium experiments, BMDMs were incubated in conditioned medium for 2 h and then collected for RNA analysis. An in vitro chemotaxis assay was performed using Transwell plate (Corning, no. 3428) as previously described<sup>41</sup>. Briefly, BMDMs (1 × 10<sup>5</sup> cells per 100 µl per well) were added into the upper chamber of an 8-µm polycarbonate filter (24-transwell format), with 600 µl conditioned medium placed in the lower chamber. After 3 h of incubation, migrated cells were fixed with methanol and stained with DAPI. DAPI<sup>+</sup> cells were counted on 4 randomly selected magnified (×20) images of stained membrane.

**In vivo monocyte infiltration assays.** Leukocyte pools from the blood of 10-week-old *Rosa26*<sup>rtm</sup> mice were subjected to erythrocyte lysis prior to staining with flow antibodies. Then, CD45<sup>+</sup>CD11b<sup>+</sup>CD115<sup>+</sup> circulating monocytes were

isolated by FACS. The monocytes were counted, and  $\sim 1 \times 10^6$  viable cells were resuspended in 200  $\mu$ l PBS and injected into each obese mouse (that is, after 5 months of HFD feeding) via tail vein. Two days later, the tdTomato<sup>+</sup> cells in the SVF of gonadal WAT were analysed using flow cytometry.

**Retroviral production and transduction.** Retrovirus was packaged in Phoenix cells as previously described<sup>17</sup>. Briefly, Phoenix packaging cells (ATCC CRL-3213) were cotransfected with 10  $\mu$ g of the pMSCV overexpression plasmids (pMSCV-Zfp423-WT, pMSCV-Zfp423- $\Delta$ NID or empty vector), 5  $\mu$ g gag-pol and 5  $\mu$ g VSV-g plasmids using Lipofectamine LTX (Thermo Fisher Scientific, no. 15338100). Subsequently, FIPs were transduced with diluted virus (1:10 ratio) in ITS medium containing 8  $\mu$ g ml<sup>-1</sup> polybrene (Sigma, no. TR-1003) for 24 h. Following transduction, cells were maintained in ITS medium for  $\geq 48$  h before beginning treatments.

**Coimmunoprecipitation assay.** Coimmunoprecipitation was performed as previously described<sup>17</sup>. In brief, cells were lysed in Pierce IP lysis buffer (Thermo Fisher Scientific, no. 87787) supplemented with 1% protease inhibitor cocktail (Sigma, no. P8340). Following the overnight incubation with the indicated antibodies at 4 °C, the cell lysates were mixed with Protein G Sepharose 4 Fast Flow (GE Healthcare Biosciences, no. 17-0618-01) for 1 h at room temperature to capture immune complexes. After 3 sequential washes with Pierce IP lysis buffer, samples were eluted by boiling in 2 $\times$ SDS loading buffer and resolved by SDS-PAGE and immunoblotting.

**Luciferase gene reporter assay.** 293/hTLR4A-MD2-CD14 cells (Invivogen, no. 293-htlr4md2cd14) were maintained in growth medium consisting of high-glucose DMEM containing 10% FBS, normocin (100  $\mu$ g ml<sup>-1</sup>), blasticidin (10  $\mu$ g ml<sup>-1</sup>) and Hygromycin B Gold (50  $\mu$ g ml<sup>-1</sup>). Cells were transfected in 24-well plates using Lipofectamine LTX with 200 ng NF- $\kappa$ B activity luciferase reporter<sup>45</sup> and 300 ng of expression plasmid (pcDNA3-FLAG-ZFP423-WT, pcDNA3-FLAG-ZFP423- $\Delta$ NID or empty vector (pcDNA3.1)). Forty-eight hours after transfection, cells were replaced with serum-free growth medium and incubated overnight. Following 100 ng ml<sup>-1</sup> LPS treatment for 8 h, cells were collected into 50  $\mu$ l of passive lysis buffer (Promega, no. E1941). Luciferase activity of cell extract was evaluated using Bright-Glo Luciferase Assay System (Promega, no. E2610) with the GluMax Discover Microplate Reader (Promega). Protein concentration of cell lysis was determined by Bradford Reagent (Sigma, no. B6916) and used for internal normalization.

**Affinity purification and proteomics analysis.** HEK 293 cells transfected with pMSCV-GFP or pMSCV-FLAG-ZFP423 plasmids were lysed in Pierce IP lysis buffer (Thermo Fisher Scientific, no. 87787) supplemented with protease inhibitor cocktail (Sigma, no. P8340). Cell lysate was incubated with anti-FLAG (Sigma, no. F1804, 1:100) or anti-ZFP423 (Santa Cruz, no. sc-48785, 1:100) overnight at 4 °C. Lysates were then incubated with Protein G Sepharose 4 Fast Flow (GE Healthcare Biosciences, no. 17-0618-01) for 2 h at 4 °C to capture immune complexes. Purified immune complexes were washed sequentially 3 times with washing buffer (50 mM HEPES (pH 7.4), 10% glycerol, 0.05% NP40, 1 mM DTT, 0.25 mM PMSF, 150 mM KCl) supplemented with protease inhibitor cocktail (Sigma, no. P8340). Proteins were eluted with Pierce IgG Elution Buffer (Thermo Fisher Scientific, no. 21004) and briefly resolved by SDS-PAGE prior to the submission to the UT Southwestern Proteomics Core. For proteomics analysis, gel fragments were reduced and alkylated with DTT (20 mM) and iodoacetamide (27.5 mM). Gel fragments were then incubated on ice with a 0.1  $\mu$ g  $\mu$ l<sup>-1</sup> solution of trypsin in 50 mM triethylammonium bicarbonate (TEAB). Fifty microlitres of 50 mM TEAB were then added to the gel pieces for overnight digestion (Pierce). Following solid-phase extraction with an Oasis MCX elution plate (Waters), the resulting peptides were reconstituted in 10  $\mu$ l of 2% (vol/vol) acetonitrile (ACN) and 0.1% trifluoroacetic acid in water. Two microlitres of this was injected onto an Orbitrap Fusion Lumos mass spectrometer (Thermo Electron) coupled to an Ultimate 3000 RSLC-Nano liquid chromatography systems (Dionex). Samples were injected onto a 75- $\mu$ m i.d., 75-cm-long EasySpray column (Thermo) and eluted with a gradient from 1–28% buffer B over 90 min. Buffer A contained 2% (vol/vol) ACN and 0.1% formic acid in water, and buffer B contained 80% (vol/vol) ACN, 10% (vol/vol) trifluoroethanol and 0.1% formic acid in water. The mass spectrometer operated in positive-ion mode with a source voltage of 2.4 kV and an ion-transfer tube temperature of 275 °C. MS scans were acquired at 120,000 resolution in the Orbitrap and up to 10 MS/MS spectra were obtained in the ion trap for each full spectrum acquired using higher-energy collisional dissociation (HCD) for ions with charges 2–7. Dynamic exclusion was set for 25 s after an ion was selected for fragmentation.

Raw MS data files were analysed using Proteome Discoverer v2.2 (Thermo), with peptide identification performed using Sequest HT searching against the human protein database from UniProt. Fragment and precursor tolerances of 10 ppm and 0.6 Da were specified, and 3 missed cleavages were allowed. Carbamidomethylation of Cys was set as a fixed modification, and oxidation of Met was set as a variable modification. The FDR cut-off was 1% for all peptides.

**Immunoblotting and antibodies.** Cells and tissues were lysed by homogenization in RIPA lysis buffer (Thermo Fisher Scientific, no. 89900). Protein extracts were separated by SDS-PAGE and then transferred onto a PVDF membrane (Millipore,

no. IPVH00010). Following overnight incubation with the indicated primary antibodies at 4 °C, membranes were incubated with IR dye-coupled secondary antibodies (LI-COR) and then visualized by using the LI-COR Odyssey infrared imaging system (LI-COR). The primary antibodies and diluted ratio include: anti-phospho-AKT 1:1,000 (Ser473; Cell Signaling Technology, no. 9271); anti-AKT 1:1,000 (Cell Signaling Technology, no. 2920); anti- $\beta$ -actin 1:5000 (Sigma, no. A1978); anti-I $\kappa$ B $\alpha$  1:1,000 (Cell Signaling Technology, no. 4814); anti- $\alpha$ -tubulin 1:1,000 (Cell Signaling Technology, no. 3873); anti-acetylated lysine 1:1,000 (Cell Signaling Technology, no. 9441); anti-NF- $\kappa$ B p65 1:1,000 (Cell Signaling Technology, no. 8242); anti-p300 1:1,000 (Cell Signaling Technology, no. 86377); anti-FLAG (Sigma, no. F1804); anti-acetyl NF- $\kappa$ B p65 (Lys310) 1:1,000 (Cell Signaling Technology, no. 12629). NuRD complex components (CHD4, MTA1, HDAC1, RbAP46) antibodies were all from NuRD Complex Antibody Sampler Kit (Cell Signaling Technology, no. 8349) and diluted 1:1,000 for primary antibody incubation. Detailed information on commercial manufacturers and validation of the antibodies can be found in the Reporting Summary.

**ChIP.** ChIP was performed as described<sup>39</sup>. FIPs from control or Mural-Zfp423<sup>TG</sup> mice were cross-linked with 1% formaldehyde in PBS for 10 min at 37 °C and quenched in 125 mM glycine in PBS for 5 min at 4 °C. FIPs were then lysed in Farnham lysis buffer (5 mM PIPES pH 8.0, 85 mM KCl, 0.5% NP-40, 1 mM DTT, and protease inhibitor cocktail (Sigma, no. P8340)) to obtain nuclear material. Crude nuclear pellets were collected by centrifugation and then lysed by incubation in lysis buffer containing 5 mM Tris-HCl pH 7.9, 1% SDS, 10 mM EDTA, 1 mM DTT and protease inhibitor cocktail (Sigma, no. P8340). Chromatin fragmentation (200- to 500-bp length) was performed at 4 °C by Bioruptor 300 using the setting of 10 cycles of 30 s on and 60 s off. Soluble chromatin was diluted 1:10 with dilution buffer (20 mM Tris-HCl pH 7.9, 0.5% Triton X-100, 2 mM EDTA, 150 mM NaCl, 1 mM DTT and protease inhibitor cocktail (Sigma, no. P8340)) and precleared using Protein G Sepharose 4 Fast Flow (GE Healthcare Biosciences, no. 17-0618-01) for 1 h at 4 °C. Precleared samples were incubated with anti-p65 antibody (1:100 in dilution, Cell Signaling Technology, no. 8242) or anti-CHD4 antibody (1:100 in dilution, Cell Signaling Technology, no. 12011) overnight at 4 °C. Antibody-protein-DNA complexes were captured by incubation with Protein G Sepharose 4 Fast Flow (GE Healthcare Biosciences, no. 17-0618-01) at 4 °C for 2 hours. Immunoprecipitated material was consecutively washed with low-salt wash buffer (20 mM Tris-HCl pH 7.9, 2 mM EDTA, 125 mM NaCl, 0.05% SDS, 1% Triton X-100, and protease inhibitor cocktail (Sigma, no. P8340)), high-salt wash buffer (20 mM Tris-HCl pH 7.9, 2 mM EDTA, 500 mM NaCl, 0.05% SDS, 1% Triton X-100, and protease inhibitor cocktail (Sigma, no. P8340)), LiCl wash buffer (10 mM Tris-HCl pH 7.9, 1 mM EDTA, 250 mM LiCl, 1% NP-40, 1% sodium deoxycholate and protease inhibitor cocktail (Sigma, no. P8340)), and 1 $\times$  Tris-EDTA (TE). After elution (100 mM NaHCO<sub>3</sub>, 1% SDS), the immunoprecipitated material was digested with RNase (Roche, no. 11119915001) and proteinase K (Thermo Fisher Scientific, no. EO0491) prior to the purification and concentration of the immunoprecipitated genomic DNA by ChIP DNA Clean & Concentrator Kit (Zymo Research, no. D5201). ChIP-isolated DNA was subjected to qPCR (ChIP-qPCR) or library production (ChIP-seq) using Nebnext NGS DNA Library Preparation for Illumina kit (New England BioLabs, no. E7645). Sequencing was performed with Illumina NextSeq 500 Mid Output (130 M) by the UT Southwestern McDermott Center Next Generation Sequencing Core.

**RNA-seq analysis.** Reads with phred quality scores <20 and <35 bp after trimming were removed from further analysis using trimalore version 0.4.1. Quality-filtered reads were then aligned to the mouse reference genome GRCm38 (mm10) using the HISAT (v2.0.1)<sup>43</sup> aligner using default settings and marked duplicates using Sambamba version 0.6.6 (ref. 44). Aligned reads were quantified using 'featurecount' (v1.4.6)<sup>45</sup> per gene ID against mouse Gencode version 20 (ref. 46). Analysis of differential gene expression was done using the R package DESeq2 (v1.6.3)<sup>47</sup>. Cut-off values of absolute fold change >1.0 and FDR  $\leq 0.05$  were then used to select for differentially expressed genes between sample group comparisons. Unadjusted and adjusted *P* values of all comparisons are provided in Supplementary Tables 1–4. All RNA-seq data have been deposited to GEO.

**ChIP-seq analysis.** Trimalore version 0.4.1 was used to remove adapter sequences and to remove reads shorter than 35 bp or with phred quality scores less than 20. Trimmed reads were then aligned to the mouse reference genome (GRCm38/mm10) using default parameters in BWA version 0.7.12 (ref. 48). The aligned reads were subsequently filtered for quality, and uniquely mappable reads were retained for further analysis using Samtools version 1.3 (ref. 49) and Sambamba version 0.6.6 (ref. 44). Library complexity was measured using BEDTools version 2.26.0 (ref. 50) and meets ENCODE data-quality standards<sup>51</sup>. Relaxed peaks were called using MACS version 2.1.0 (ref. 52) with a *P* value of  $1 \times 10^{-2}$ . Gene annotation of the regions bound by p65 were performed by GREAT version 3.0 (ref. 53). For heatmaps and profiles of ChIP-seq intensities, we used deepTools version 2.5.0 (ref. 54) to generate read abundance from all ChIP-seq datasets around peak centre ( $\pm 2.0$  kb), using 'computeMatrix'. These matrices were then used to create heatmaps and profiles, using deepTools commands 'plotHeatmap' and 'plotProfile', respectively. To identify the primary motif present in p65-occupied

peaks, we performed de novo motif discovery using Homer version 4.9 with the 'findMotifsGenome.pl' script using default parameters<sup>55,56</sup>. Additional detail regarding software and analysis can be found in the Reporting Summary.

**In vivo insulin stimulation.** After overnight fasting, anaesthetized animals were injected with insulin (2 U per kg (body weight); Eli Lilly, no. 0002751001) through the portal vein. Gonadal WAT was immediately frozen 5 min after insulin injection. Tissues collected before insulin treatment were used as untreated controls for each mouse.

**Metabolic phenotyping.** For glucose tolerance tests, mice were subjected to an overnight fast and then i.p. injected with glucose (Sigma, no. G7021) at the dosage of 1 g per kg (body weight). For insulin tolerance tests, mice were i.p. administered with insulin (0.75 U per kg (body weight); Eli Lilly, no. 0002751001) after a 6-h fast. Glucose concentrations were determined using Bayer Contour glucometers.

**Statistics and reproducibility.** No statistical method was used to determine sample sizes. We determined sample sizes on the basis of experience and reported experimental designs. No randomization or blinding was performed to allocate the samples. No criteria of inclusion or exclusion of data were used. Statistical analysis was carried out as indicated in the figure legends. All data are presented as the mean  $\pm$  s.e.m. unless otherwise indicated in the figure legends. Data variance was examined by *F* test or Bartlett's test. The data meet the assumptions of the indicated statistical analysis. All tests were performed as two sided. A *P* value less than 0.05 was considered statistically significant. All statistical analyses were performed using Microsoft Excel or GraphPad Prism 8.0 (GraphPad Software). All statistical information, including *P* values, samples sizes and repetitions, are provided in the Source Data associated with each figure.

**Reporting Summary.** Further information on research design is available in the Nature Research Reporting Summary linked to this article.

## Data availability

All animal models, reagents and datasets are freely available to investigators upon reasonable request. ChIP-seq data have been deposited to Gene Expression Omnibus (GEO accession [GSE134868](https://www.ncbi.nlm.nih.gov/geo/query/acc.cgi?acc=GSE134868)). RNA-seq data have been deposited to Gene Expression Omnibus (GEO accession [GSE151092](https://www.ncbi.nlm.nih.gov/geo/query/acc.cgi?acc=GSE151092)). Mass spectrometry data has been deposited to MAssIVE (<http://massive.ucsd.edu/ProteoSAFe/status.jsp?task=af5ccb331b004854ac6c182936148168>). Source data are provided with this paper.

Received: 19 June 2020; Accepted: 16 September 2020;

Published online: 02 November 2020

## References

- Weisberg, S. P. et al. CCR2 modulates inflammatory and metabolic effects of high-fat feeding. *J. Clin. Invest.* **116**, 115–124 (2006).
- Oh, D. Y., Morinaga, H., Talukdar, S., Bae, E. J. & Olefsky, J. M. Increased macrophage migration into adipose tissue in obese mice. *Diabetes* **61**, 346–354 (2012).
- Amano, S. U. et al. Local proliferation of macrophages contributes to obesity-associated adipose tissue inflammation. *Cell Metab.* **19**, 162–171 (2014).
- Saltiel, A. R. & Olefsky, J. M. Inflammatory mechanisms linking obesity and metabolic disease. *J. Clin. Invest.* **127**, 1–4 (2017).
- Hepler, C. et al. Identification of functionally distinct fibro-inflammatory and adipogenic stromal subpopulations in visceral adipose tissue of adult mice. *eLife* **7**, e39636 (2018).
- Giles, D. A. et al. Thermoneutral housing exacerbates nonalcoholic fatty liver disease in mice and allows for sex-independent disease modeling. *Nat. Med.* **23**, 829–838 (2017).
- Tian, X. Y. et al. Thermoneutral housing accelerates metabolic inflammation to potentiate atherosclerosis but not insulin resistance. *Cell Metab.* **23**, 165–178 (2016).
- Hill, A. A. et al. Activation of NF- $\kappa$ B drives the enhanced survival of adipose tissue macrophages in an obesogenic environment. *Mol. Metab.* **4**, 665–677 (2015).
- Chiang, S. H. et al. The protein kinase IKK $\epsilon$  regulates energy balance in obese mice. *Cell* **138**, 961–975 (2009).
- Cho, K. W., Morris, D. L. & Lumeng, C. N. Flow cytometry analyses of adipose tissue macrophages. *Methods Enzymol.* **537**, 297–314 (2014).
- Hill, D. A. et al. Distinct macrophage populations direct inflammatory versus physiological changes in adipose tissue. *Proc. Natl Acad. Sci. USA* **115**, E5096–E5105 (2018).
- Gupta, R. K. et al. Zfp423 expression identifies committed preadipocytes and localizes to adipose endothelial and perivascular cells. *Cell Metab.* **15**, 230–239 (2012).
- Vishvanath, L. et al. Pdgfr $\beta$ <sup>+</sup> mural preadipocytes contribute to adipocyte hyperplasia induced by high-fat-diet feeding and prolonged cold exposure in adult mice. *Cell Metab.* **23**, 350–359 (2016).
- Gupta, R. K. et al. Transcriptional control of preadipocyte determination by Zfp423. *Nature* **464**, 619–623 (2010).
- Hepler, C. et al. Directing visceral white adipocyte precursors to a thermogenic adipocyte fate improves insulin sensitivity in obese mice. *eLife* **6**, e27669 (2017).
- Shao, M. et al. Fetal development of subcutaneous white adipose tissue is dependent on Zfp423. *Mol. Metab.* **6**, 111–124 (2017).
- Shao, M. et al. Zfp423 maintains white adipocyte identity through suppression of the beige cell thermogenic gene program. *Cell Metab.* **23**, 1167–1184 (2016).
- Shao, M. et al. De novo adipocyte differentiation from Pdgfr $\beta$ <sup>+</sup> preadipocytes protects against pathologic visceral adipose expansion in obesity. *Nat. Commun.* **9**, 890 (2018).
- Kloting, N. et al. Insulin-sensitive obesity. *Am. J. Physiol. Endocrinol. Metab.* **299**, E506–E515 (2010).
- Huang, B., Yang, X. D., Lamb, A. & Chen, L. F. Posttranslational modifications of NF- $\kappa$ B: another layer of regulation for NF- $\kappa$ B signaling pathway. *Cell Signal* **22**, 1282–1290 (2010).
- Chen, L. F., Mu, Y. & Greene, W. C. Acetylation of RelA at discrete sites regulates distinct nuclear functions of NF- $\kappa$ B. *EMBO J* **21**, 6539–6548 (2002).
- Chen, L., Fischle, W., Verdin, E. & Greene, W. C. Duration of nuclear NF- $\kappa$ B action regulated by reversible acetylation. *Science* **293**, 1653–1657 (2001).
- Torchy, M. P., Hamiche, A. & Klaholz, B. P. Structure and function insights into the NuRD chromatin remodeling complex. *Cell Mol. Life Sci* **72**, 2491–2507 (2015).
- Lauberth, S. M. & Rauchman, M. A conserved 12-amino acid motif in Sall1 recruits the nucleosome remodeling and deacetylase corepressor complex. *J. Biol. Chem.* **281**, 23922–23931 (2006).
- Reilly, S. M. & Saltiel, A. R. Adapting to obesity with adipose tissue inflammation. *Nat. Rev. Endocrinol.* **13**, 633–643 (2017).
- Jia, L. et al. Hepatocyte Toll-like receptor 4 regulates obesity-induced inflammation and insulin resistance. *Nat. Commun.* **5**, 3878 (2014).
- Tao, C. et al. Short-term versus long-term effects of adipocyte toll-like receptor 4 activation on insulin resistance in male mice. *Endocrinology* **158**, 1260–1270 (2017).
- Cardamone, M. D. et al. A protective strategy against hyperinflammatory responses requiring the nontranscriptional actions of GPS2. *Mol. Cell* **46**, 91–104 (2012).
- Gillum, M. P. et al. SirT1 regulates adipose tissue inflammation. *Diabetes* **60**, 3235–3245 (2011).
- Saijo, K. et al. A Nurrl/CoREST pathway in microglia and astrocytes protects dopaminergic neurons from inflammation-induced death. *Cell* **137**, 47–59 (2009).
- Addison, W. N. et al. Zfp423 regulates skeletal muscle regeneration and proliferation. *Mol. Cell Biol.* **39**, e00447-18 (2019).
- Cheng, L. E., Zhang, J. & Reed, R. R. The transcription factor Zfp423/OAZ is required for cerebellar development and CNS midline patterning. *Dev. Biol.* **307**, 43–52 (2007).
- Cheng, L. E. & Reed, R. R. Zfp423/OAZ participates in a developmental switch during olfactory neurogenesis. *Neuron* **54**, 547–557 (2007).
- Warming, S., Rachel, R. A., Jenkins, N. A. & Copeland, N. G. Zfp423 is required for normal cerebellar development. *Mol. Cell Biol.* **26**, 6913–6922 (2006).
- Kiernan, R. et al. Post-activation turn-off of NF- $\kappa$ B-dependent transcription is regulated by acetylation of p65. *J. Biol. Chem.* **278**, 2758–2766 (2003).
- Yeung, F. et al. Modulation of NF- $\kappa$ B-dependent transcription and cell survival by the SIRT1 deacetylase. *EMBO J.* **23**, 2369–2380 (2004).
- Spallanzani, R. G. et al. Distinct immunocyte-promoting and adipocyte-generating stromal components coordinate adipose tissue immune and metabolic tenors. *Sci. Immunol.* **4**, eaaw3658 (2019).
- Mahlakoiv, T. et al. Stromal cells maintain immune cell homeostasis in adipose tissue via production of interleukin-33. *Sci. Immunol.* **4**, eaax0416 (2019).
- Luo, X. et al. PARP-1 controls the adipogenic transcriptional program by PARylating C/EBP $\beta$  and modulating its transcriptional activity. *Mol. Cell* **65**, 260–271 (2017).
- Shan, B. et al. The metabolic ER stress sensor IRE1 $\alpha$  suppresses alternative activation of macrophages and impairs energy expenditure in obesity. *Nat. Immunol.* **18**, 519–529 (2017).
- Oh, D. Y. et al. GPR120 is an omega-3 fatty acid receptor mediating potent anti-inflammatory and insulin-sensitizing effects. *Cell* **142**, 687–698 (2010).
- Oh, D. Y. et al. A Gpr120-selective agonist improves insulin resistance and chronic inflammation in obese mice. *Nat. Med.* **20**, 942–947 (2014).
- Kim, D., Langmead, B. & Salzberg, S. L. HISAT: a fast spliced aligner with low memory requirements. *Nat. Methods* **12**, 357–360 (2015).
- Tarasov, A., Vilella, A. J., Cuppen, E., Nijman, I. J. & Prins, P. Sambamba: fast processing of NGS alignment formats. *Bioinformatics* **31**, 2032–2034 (2015).
- Liao, Y., Smyth, G. K. & Shi, W. featureCounts: an efficient general purpose program for assigning sequence reads to genomic features. *Bioinformatics* **30**, 923–930 (2014).

46. Frankish, A. et al. GENCODE reference annotation for the human and mouse genomes. *Nucleic Acids Res.* **47**, D766–D773 (2019).
47. Love, M. I., Huber, W. & Anders, S. Moderated estimation of fold change and dispersion for RNA-seq data with DESeq2. *Genome Biol.* **15**, 550 (2014).
48. Li, H. & Durbin, R. Fast and accurate short read alignment with Burrows–Wheeler transform. *Bioinformatics* **25**, 1754–1760 (2009).
49. Li, H. et al. The Sequence Alignment/Map format and SAMtools. *Bioinformatics* **25**, 2078–2079 (2009).
50. Quinlan, A. R. & Hall, I. M. BEDTools: a flexible suite of utilities for comparing genomic features. *Bioinformatics* **26**, 841–842 (2010).
51. Landt, S. G. et al. ChIP-seq guidelines and practices of the ENCODE and modENCODE consortia. *Genome Res.* **22**, 1813–1831 (2012).
52. Feng, J., Liu, T., Qin, B., Zhang, Y. & Liu, X. S. Identifying ChIP-seq enrichment using MACS. *Nat. Protoc.* **7**, 1728–1740 (2012).
53. McLean, C. Y. et al. GREAT improves functional interpretation of cis-regulatory regions. *Nat. Biotechnol.* **28**, 495–501 (2010).
54. Ramirez, F. et al. deepTools2: a next generation web server for deep-sequencing data analysis. *Nucleic Acids Res.* **44**, W160–W165 (2016).
55. Heinz, S. et al. Simple combinations of lineage-determining transcription factors prime cis-regulatory elements required for macrophage and B cell identities. *Mol. Cell* **38**, 576–589 (2010).
56. Heinz, S., Romanoski, C. E., Benner, C. & Glass, C. K. The selection and function of cell type-specific enhancers. *Nat. Rev. Mol. Cell Biol.* **16**, 144–154 (2015).

### Acknowledgements

The authors are grateful to P. Scherer and C. Kusminski for critical reading of the manuscript and members of the UTSW Touchstone Diabetes Center for useful discussions. The authors thank C. Lee, the UTSW Animal Resource Center, Metabolic Phenotyping Core, Pathology Core, Live Cell Imaging Core, Flow Cytometry Core, McDermott Sequencing Center and Proteomics Core, for excellent guidance and

assistance with experiments performed here. This study and/or personnel were supported in part by the NIH NIDDK F31DK113696 to C.H., NIDDK R01 DK104789, R56 DK119163 and R01 DK119163 to R.K.G., the American Heart Association postdoctoral fellowship 16POST26420136 to M.S., NIDDK R01 DK115477 to D.W.S., NIDDK R01 DK108773 and AHA 14SDG19880020 to D.O., American Diabetes Association 1-18-PMF-030 to V.A.P., NIH R03 DK101865 to O.T.G, the Cancer Prevention and Research Institute of Texas (RP150596) to S.D.B and V.S.M, NIH NIAAA K01AA024809 to L.J. and NIDDK PO1 DK088761 to J.K.E.

### Author contributions

B.S., M.S. and R.K.G. conceived the study and wrote the manuscript. B.S., M.S., D.O. and R.K.G. designed experiments. B.S., M.S., Q.Z., C.H., L.V., V.A.P. and Y.A.A. performed experiments and analysed the data. S.D.B., M.S. and V.S.M. designed and analysed ChIP-seq experiments. D.W.S., O.T.G, J.K.E. and L.J. provided key reagents.

### Competing interests

The authors declare that they have no competing interests.

### Additional information

**Extended data** is available for this paper at <https://doi.org/10.1038/s42255-020-00301-7>.

**Supplementary information** is available for this paper at <https://doi.org/10.1038/s42255-020-00301-7>.

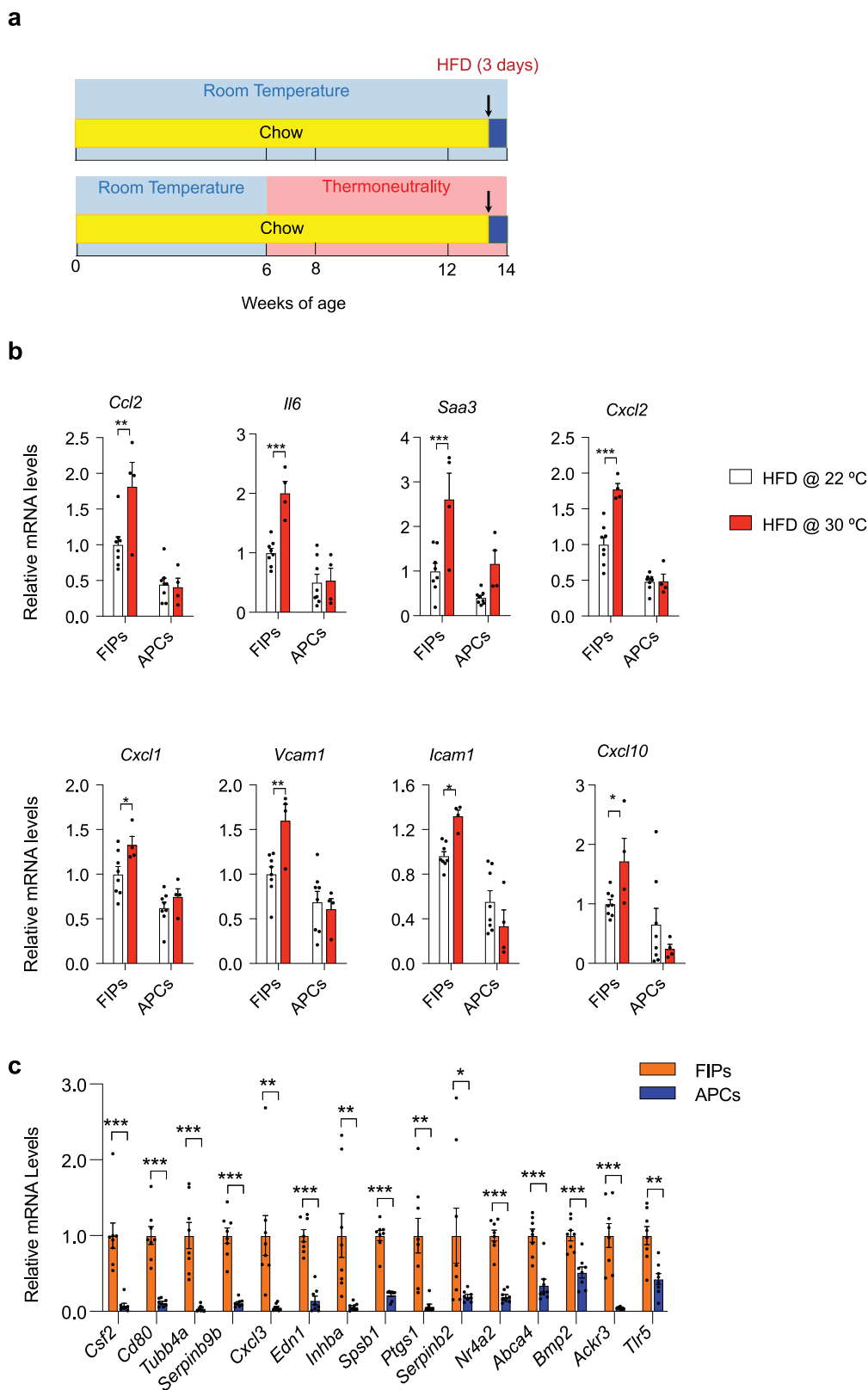
**Correspondence and requests for materials** should be addressed to R.K.G.

**Peer review information** Primary Handling Editor: Christoph Schmitt.

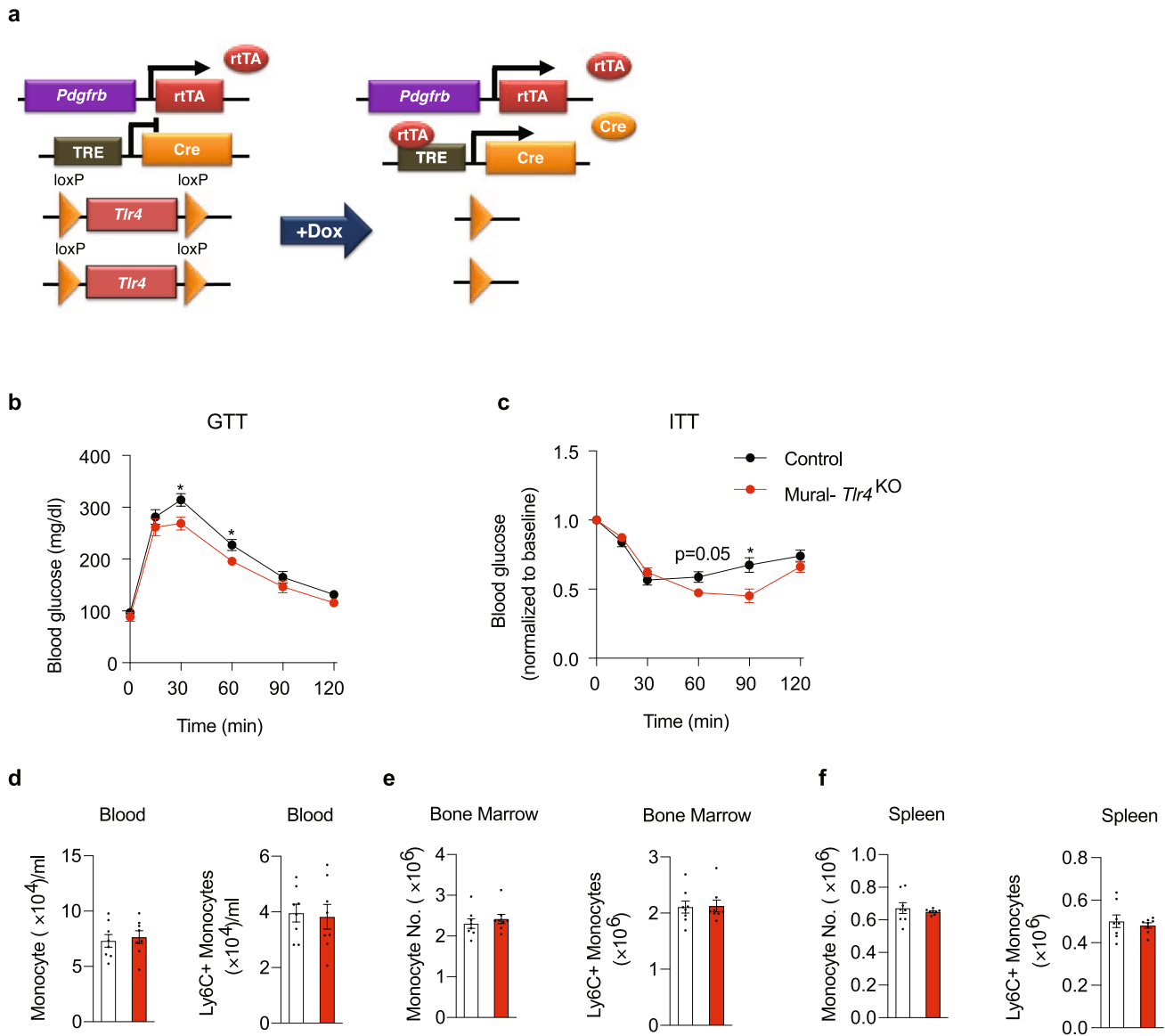
**Reprints and permissions information** is available at [www.nature.com/reprints](http://www.nature.com/reprints).

**Publisher's note** Springer Nature remains neutral with regard to jurisdictional claims in published maps and institutional affiliations.

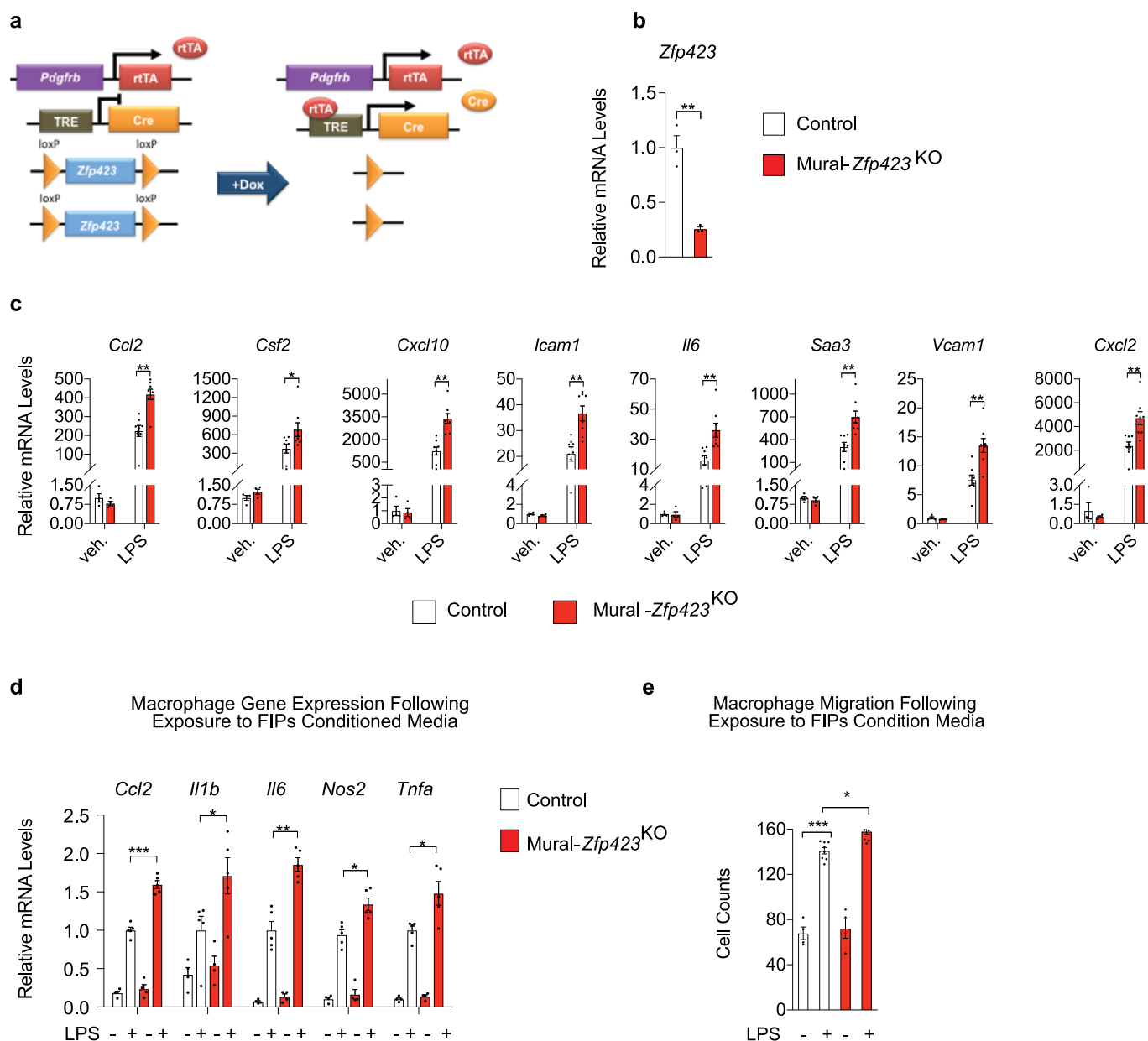
© The Author(s), under exclusive licence to Springer Nature Limited 2020



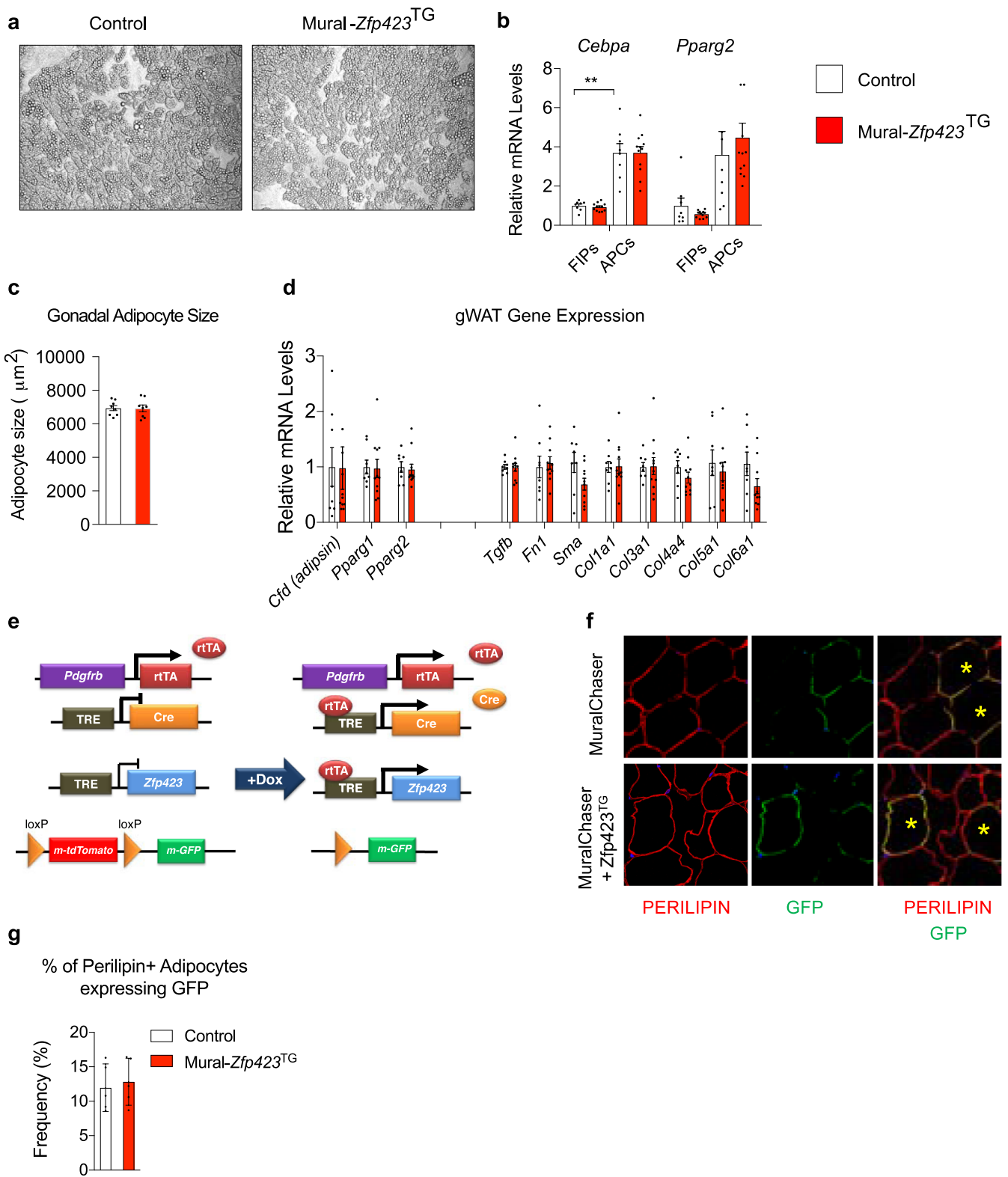
**Extended Data Fig. 1 | Thermoneutral housing amplifies the pro-inflammatory phenotype of FIPs.** **a**, Experimental design: 6 weeks-old male C57BL/6 mice were transferred to thermoneutral housing conditions (TN, 30 °C) or maintained at room temperature (RT, 22 °C) for two months. Then animals were fed HFD for 3 days prior to gene expression analysis of FIPs and APCs. **b**, mRNA levels of indicated genes in freshly isolated FIPs and APCs obtained following 3 days of HFD. For each experiment,  $n = 8$  for FIPs and APCs at 22 °C.  $n = 4$  for FIPs and APCs at 30 °C. Data presented were reproduced in two independent experiments. Bars represent mean  $\pm$  s.e.m., \* denotes  $p < 0.05$ , \*\* denotes  $p < 0.01$ , and \*\*\* denotes  $p < 0.001$  by two-way ANOVA. **c**, mRNA levels of TNF-signaling signature genes (see Supplementary Table 1) in freshly isolated FIPs ( $n=8$ ) and APCs ( $n=8$ ) obtained following 1 month of HFD at 30 °C. Bars represent mean  $\pm$  s.e.m., \* denotes  $p < 0.05$ , \*\* denotes  $p < 0.01$ , and \*\*\* denotes  $p < 0.001$  by unpaired two-tailed Student's t-test. Exact p values and numbers of repetitions can be found in Source Data Extended Data Figure 1.



**Extended Data Fig. 2 | Derivation of Mural-*Tlr4*<sup>KO</sup> mice and systemic phenotype following high fat diet feeding.** **a**, Mural-*Tlr4*<sup>KO</sup> (*Pdgfrb*<sup>rtTA</sup>; *TRE-Cre*; *Tlr4*<sup>loxP/loxP</sup>) mice were generated by breeding the *Pdgfrb*<sup>rtTA</sup> transgenic mice to animals expressing Cre recombinase under the control of the tetracycline-response element (*TRE-Cre*) and carrying floxed *Tlr4* alleles (*Tlr4*<sup>loxP/loxP</sup>). Littermates carrying only *Pdgfrb*<sup>rtTA</sup> and *Tlr4*<sup>loxP/loxP</sup> alleles (that is Cre-) were used as the control animals (Control). The addition of doxycycline (Dox) leads to inactivation of *Tlr4* in *Pdgfrb*-expressing cells. **b**, Intraperitoneal glucose tolerance tests (GTT) of RT-housed Control (n=9) and Mural-*Tlr4*<sup>KO</sup> (n=6) mice after HFD feeding. \* denotes  $p < 0.05$  by unpaired two-tailed Student's *t*-test. **c**, Intraperitoneal insulin tolerance tests (ITT) of RT-housed Control (n=9) and Mural-*Tlr4*<sup>KO</sup> (n=6) mice after HFD feeding. \* denotes  $p < 0.05$  by unpaired two-tailed Student's *t*-test. **d-f**, Levels of total monocytes and pro-inflammatory monocytes (LY6C+) in blood (**d**), bone marrow (**e**), and spleen (**f**) of Control (n=8) and Mural-*Tlr4*<sup>KO</sup> (n=8) mice after 5 months of HFD feeding. Bars represent mean  $\pm$  s.e.m. Exact *p* values can be found in Source Data Extended Data Figure 2. Data were reproduced two times in independent experiments.

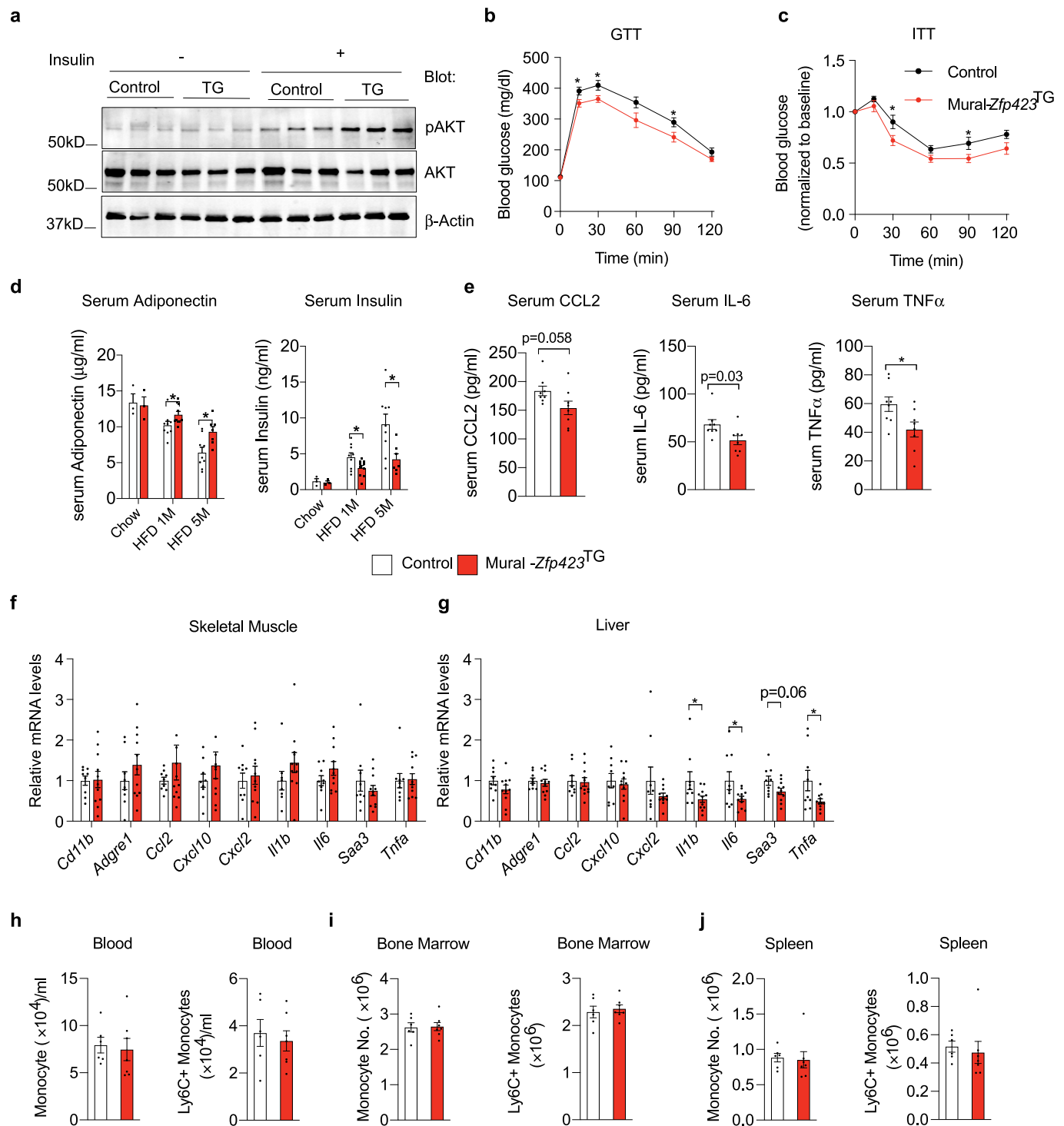


**Extended Data Fig. 3 | Inactivation of *Zfp423* exacerbates FIPs inflammatory responses.** **a**, Mural-*Zfp423*<sup>KO</sup> (*Pdgfrb*<sup>rtTA</sup>; *TRE-Cre*; *Zfp423*<sup>loxP/loxP</sup>) mice were generated by breeding the *Pdgfrb*<sup>rtTA</sup> transgenic mice to animals expressing Cre recombinase under the control of the tetracycline-response element (*TRE-Cre*) and carrying floxed *Zfp423* alleles (*Zfp423*<sup>loxP/loxP</sup>). Littermates carrying only *Pdgfrb*<sup>rtTA</sup> and *Zfp423*<sup>loxP/loxP</sup> alleles (that is Cre) were used as the control animals (Control). The addition of doxycycline (Dox) leads to inactivation of *Zfp423* in *Pdgfrb*-expressing cells. **b**, mRNA levels of *Zfp423* in FIPs of Control (n=3) and Mural-*Zfp423*<sup>KO</sup> (n=3) mice fed Dox-containing chow diet for 10 days. **c**, mRNA levels of indicated pro-inflammatory genes in indicated FIPs treated with vehicle (veh.) (n=4) or 100 ng/ml LPS (n=8) for 2 hours. **d**, mRNA levels of genes associated with macrophage activation in cultured BMDMs following exposure to indicated FIPs conditioned media (CM) for 1.5 hours. n=4 (for groups with vehicle treatment) or n=5 (for groups with LPS treatment) independent wells of macrophages examined per experiment. **e**, Macrophage migration following exposure to FIPs conditioned media (CM): cell counts of migrated macrophages following exposure to indicated CM for 3 hours. n=4 (for groups with vehicle treatment) or n=9 (for groups with LPS treatment) independent wells of macrophages examined per experiment. For panels **d**, **e** FIPs (isolated from pooled depots of 6-8 mice per genotype) were treated with vehicle or LPS (100 ng/ml) for 2 hours and then incubated in serum-free medium for an additional 24 hours to produce conditioned media. Experiments in this figure were independently repeated three times. Data in this figure are shown as the mean  $\pm$  s.e.m., \* $p$  < 0.05, \*\* $p$  < 0.01 or \*\*\* $p$  < 0.001 by two-tailed unpaired Student's *t*-test (**b**) or two-way ANOVA (**c-e**). Exact *p* values can be found in Source Data Extended Data Figure 3.

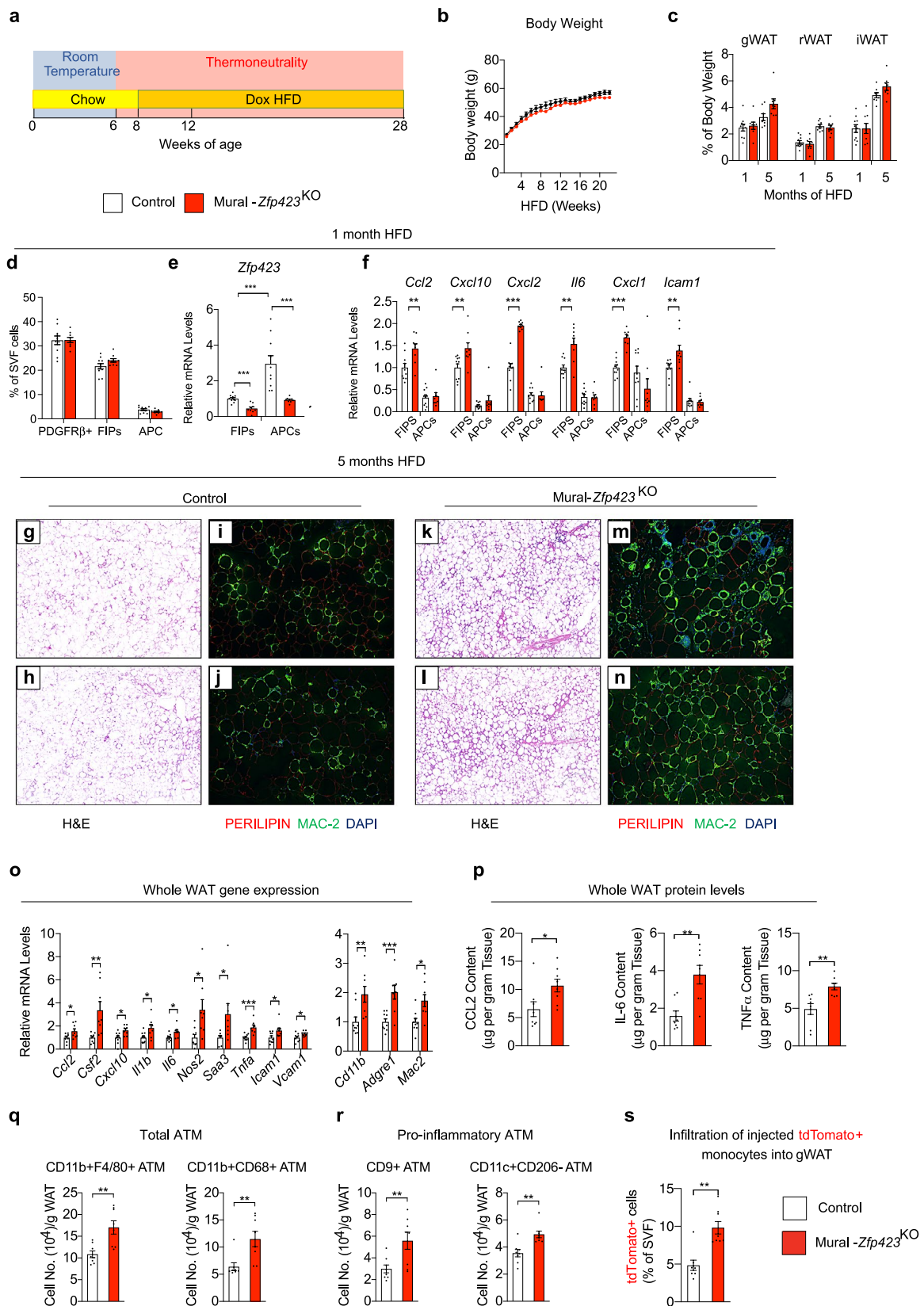


Extended Data Fig. 4 | See next page for caption.

**Extended Data Fig. 4 | Adipogenesis from PDGFR $\beta$ + progenitors is not impacted in Mural-*Zfp423*<sup>TG</sup> mice. **a**, Representative 20x magnification images of APCs from gonadal WAT of Control (pooled from 4 mice) and Mural-*Zfp423*<sup>TG</sup> (pooled from 4 mice) animals maintained for 8 days in growth media. No overt difference in the degree of spontaneous adipogenesis is observed. **b**, mRNA levels of key regulators of adipogenesis (*Cebpa* and *Pparg2*) in freshly isolated FIPs and APCs from gonadal WAT of Control (n=8) and Mural-*Zfp423*<sup>TG</sup> (n=12) mice after 1-month HFD feeding. **c**, Average adipocyte size within gonadal WAT sections of control (n=8) and Mural-*Zfp423*<sup>TG</sup> (n=8) mice after 5-month Dox-HFD feeding. **d**, mRNA levels of adipocyte-selective genes and fibrogenic genes in whole gonadal WAT of control (n=8) and Mural-*Zfp423*<sup>TG</sup> (n=11) mice after 5-month Dox-HFD feeding. In **b-d**, bars represent mean  $\pm$  s.e.m. \*\* denotes  $p < 0.01$  by one-way ANOVA (**b**). **e**, MuralChaser-*Zfp423*<sup>TG</sup> (*Pdgfrb*<sup>rtTA</sup>; *TRE-Cre*; *TRE-Zfp423*; *Rosa26R*<sup>mT/mG</sup>) mice were generated by reconstituting the *Rosa26R*<sup>mT/mG</sup> allele into the Mural-*Zfp423*<sup>TG</sup> background. The addition of doxycycline results in overexpression of *Zfp423* and indelible labeling of *Pdgfrb*-expressing cells with mGFP expression. **f**, Representative 63x magnification confocal immunofluorescence images of gonadal WAT sections from MuralChaser (*Pdgfrb*<sup>rtTA</sup>; *TRE-Cre*; *Rosa26R*<sup>mT/mG</sup>) and MuralChaser-*Zfp423*<sup>TG</sup> mice after HFD feeding. 8 weeks-old animals were maintained on doxycycline-containing HFD feed for 8 weeks. Sections were stained with anti-PERILIPIN (PERILIPIN; red) and anti-GFP (green) antibodies and counterstained with DAPI (blue; nuclei). Composite images were generated by digital overlay. **g**, Quantification of de novo adipogenesis: the frequency of GFP+ PERILIPIN+ cells observed by immunostaining was quantified by assaying ~ 3000-4000 adipocytes total from 5 mice per genotype. Bars represent mean  $\pm$  s.e.m. Exact  $p$  values can be found in Source Data Extended Data Figure 4. Data were reproduced two times in independent experiments.**

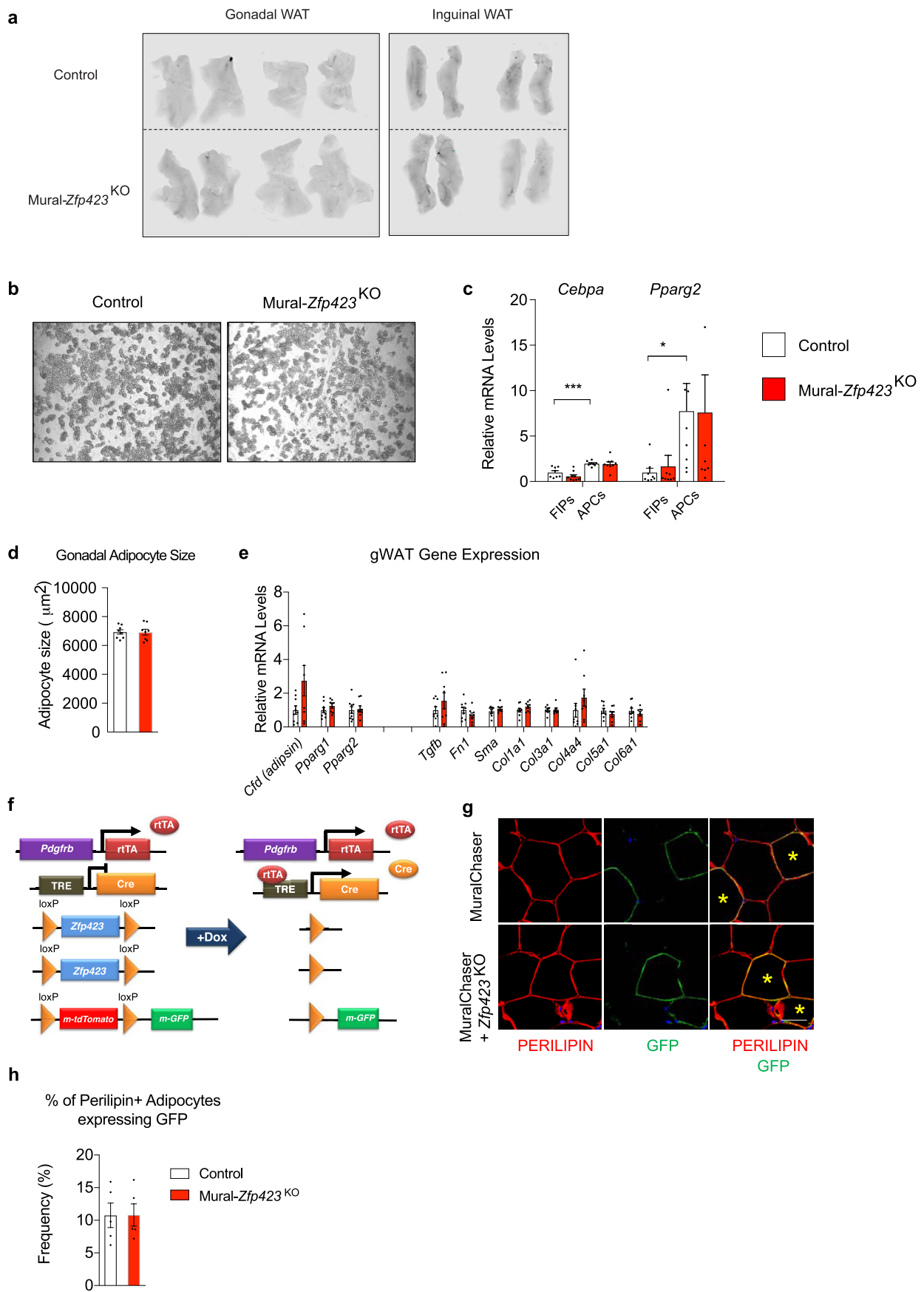


**Extended Data Fig. 5 | *Zfp423* overexpression in PDGFR $\beta$ + cells confers metabolic benefits in obesity.** **a**, Western blot of phosphorylated AKT (pAKT), total AKT, and  $\beta$ -Actin protein expression in tissue extracts of gonadal WAT from Control (n=3) and Mural-*Zfp423*<sup>TG</sup> (n=3) mice after 5-month HFD feeding. Tissues were collected before (- insulin) and after insulin stimulation (+ insulin). **b**, Intra-peritoneal glucose tolerance tests (GTT) of thermoneutral-housed Control (n=9) and Mural-*Zfp423*<sup>TG</sup> (n=11) mice after HFD feeding. \* denotes  $p < 0.05$  by unpaired two-tailed Student's t-test. **c**, Intra-peritoneal insulin tolerance tests (ITT) of thermoneutral-housed Control (n=9) and Mural-*Zfp423*<sup>TG</sup> (n=11) mice after HFD feeding. \* denotes  $p < 0.05$  by unpaired two-tailed Student's t-test. **d**, Levels of serum ADIPONECTIN and serum INSULIN (six-hour fasted) in Control and Mural-*Zfp423*<sup>TG</sup> mice maintained on doxycycline-containing chow diet or doxycycline-containing HFD for 1 month or 5 months. For control mice, n=3 of chow, n=9 of 1-month HFD, n=9 of 5-month HFD; for Mural-*Zfp423*<sup>TG</sup> mice, n=3 of chow, n=10 of 1-month HFD, n=7 of 5-month HFD. **e** analysed using flow cytometry Serum levels of indicated pro-inflammatory cytokines (CCL2, IL-6, TNF $\alpha$ ) in Control (n=8) and Mural-*Zfp423*<sup>TG</sup> (n=8) mice maintained on doxycycline-containing HFD for 5 months. **f**, mRNA levels of pro-inflammatory genes in skeletal muscle of Control (n=8) and Mural-*Zfp423*<sup>TG</sup> (n=8) mice after 5-months HFD feeding. **g**, mRNA levels of pro-inflammatory genes in livers of Control (n=8) and Mural-*Zfp423*<sup>TG</sup> (n=8) mice after 5-months HFD feeding. **h-j**, Levels of total monocytes and pro-inflammatory monocytes (LY6C+) in blood (**h**), bone marrow (**i**), and spleen (**j**) of Control (n=6) and Mural-*Zfp423*<sup>TG</sup> (n=7) mice after 5 months of HFD feeding. For panels **d-j**, bars represent mean  $\pm$  s.e.m., and \* denotes  $p < 0.05$  by unpaired two-tailed Student's t-test. Exact p values, numbers of repetitions, and uncropped western blots can be found in Source Data Extended Data Figure 5.



Extended Data Fig. 6 | See next page for caption.

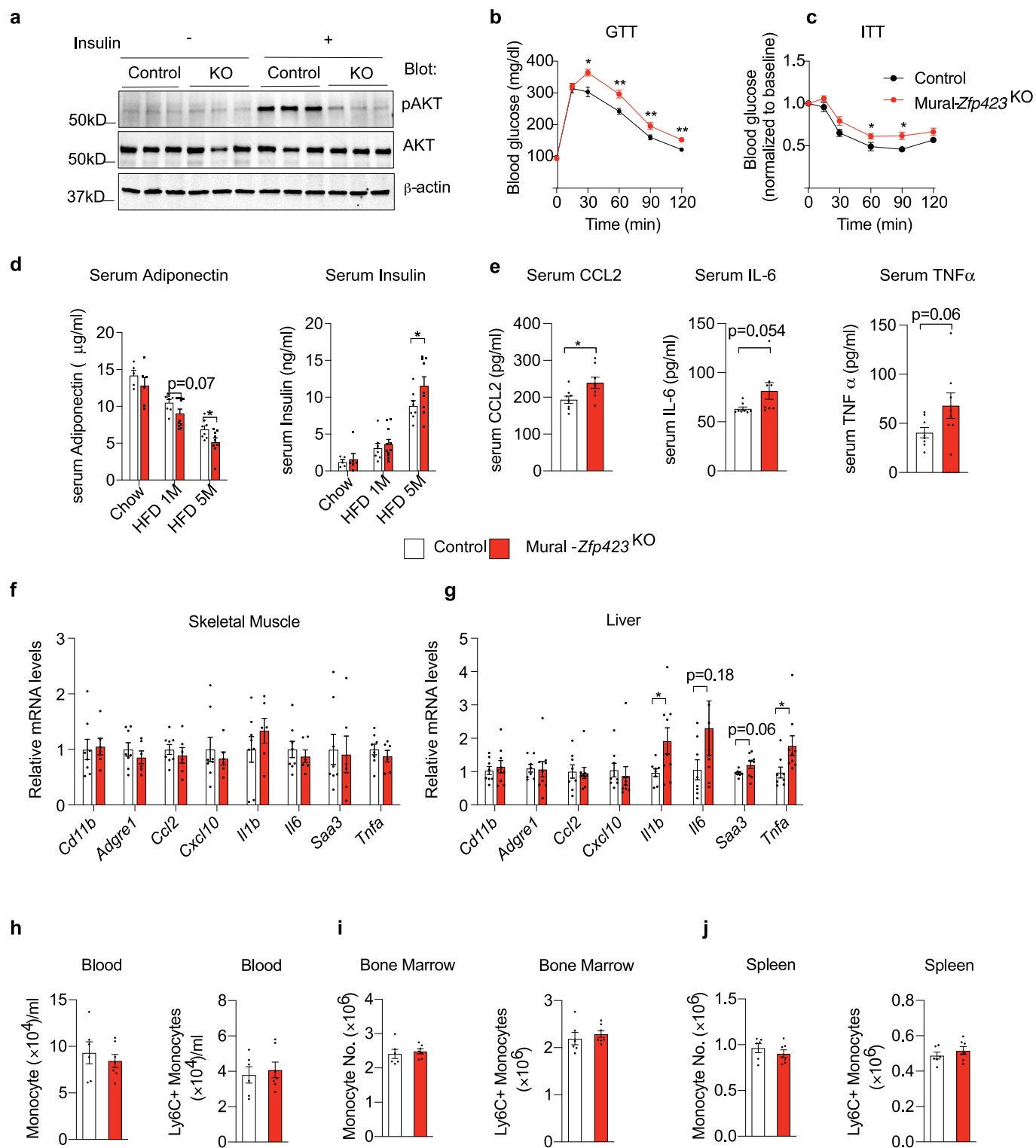
**Extended Data Fig. 6 | *Zfp423* inactivation in PDGFR $\beta$ + cells exacerbates chronic WAT inflammation.** **a**, Approach: 6 weeks-old mice were preconditioned at thermoneutrality for two weeks then switched to a doxycycline-containing HFD for indicated period. **b**, Control (n=8; black) and Mural-*Zfp423*<sup>KO</sup> (n=9; red) body weights following the onset of HFD feeding. **c**, WAT mass mice after 1 month (Control, n=10; Mural-*Zfp423*<sup>KO</sup>, n=8) and 5 months (Control, n=8; Mural-*Zfp423*<sup>KO</sup>, n=8) of HFD feeding. **d**, Frequency of total PDGFR $\beta$ + cells, FIPs, and APCs within gonadal WAT (gWAT) of Control (n=10) and Mural-*Zfp423*<sup>KO</sup> (n=9) mice after 1 month of HFD feeding. **e**, *Zfp423* mRNA levels within freshly isolated FIPs and APCs from gWAT of Control (n=10) and Mural-*Zfp423*<sup>KO</sup> (n=9) mice after 1 month of HFD feeding. **f**, Pro-inflammatory gene expression within freshly isolated FIPs and APCs from gWAT of Control (n=10) and Mural-*Zfp423*<sup>KO</sup> (n=9) mice after 1 month of HFD feeding. **g, h**, 4x magnification images of H&E stained gWAT sections from Control mice maintained on HFD for 5 months. **i, j**, 10x magnification images of PERILIPIN (red) and MAC-2 (green) expression within gWAT sections from Control mice maintained on HFD for 5 months. **k, l**, 4x magnification images of H&E stained gWAT sections from from Mural-*Zfp423*<sup>KO</sup> mice maintained on HFD for 5 months. **m, n**, 10x magnification images of PERILIPIN (red) and MAC-2 (green) expression within gWAT sections from Mural-*Zfp423*<sup>KO</sup> mice maintained on HFD for 5 months. **o**, Pro-inflammatory- and macrophage-selective gene expression in gWAT of Control (n=9) and Mural-*Zfp423*<sup>KO</sup> (n=8) mice after 5-months HFD feeding. **p**, Protein levels of indicated cytokines in gWAT of Control (n=8) and Mural-*Zfp423*<sup>KO</sup> (n=8) mice after 5-months HFD feeding. **q**, Frequency of total adipose tissue macrophages (ATMs) within gWAT of Control (n=8) and Mural-*Zfp423*<sup>KO</sup> (n=8) mice after 5 months of HFD-feeding. **r**, Frequency of pro-inflammatory ATMs within gWAT of Control (n=8) and Mural-*Zfp423*<sup>KO</sup> (n=8) mice after 5 months of HFD-feeding. **s**, Frequency of tdTomato+ macrophages within gWAT SVF of obese mice following injection of tdTomato+ monocytes. n=8 for Control; n=8 for Mural-*Zfp423*<sup>TG</sup>. Bars represent mean  $\pm$  s.e.m., \* $p$ <0.05, \*\* $p$ <0.01 or \*\*\* $p$ <0.001 by unpaired two-tailed Student's t-test (**o-s**) or one-way ANOVA (**e, f**). Exact  $p$  values and numbers of repetitions can be found in Source Extended Data Figure 6.



Extended Data Fig. 7 | See next page for caption.

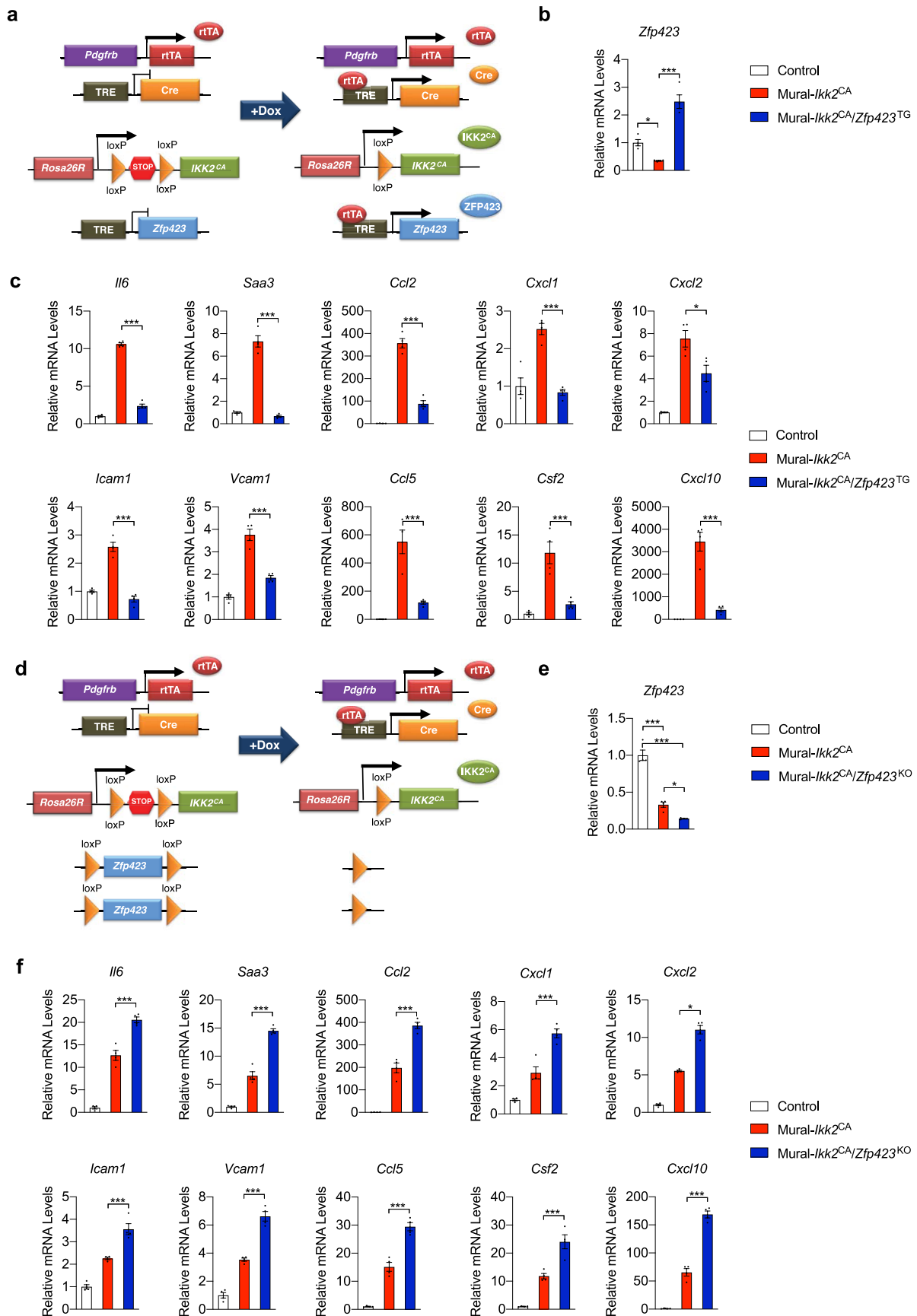
**Extended Data Fig. 7 | Vascular integrity and adipocyte differentiation from PDGFR $\beta$ + perivascular progenitors are not impacted in Mural-Zfp423<sup>KO</sup> mice.**

**a**, Representative images of gonadal and inguinal WAT depots of Control and Mural-Zfp423<sup>KO</sup> mice after Evans blue injection. Fixed tissues were imaged for Evans Blue auto fluorescence at 700 nm using a LI-COR Odyssey infrared imaging system. **b**, Representative 10x magnification images of APCs from gonadal WAT of Control (pooled from 4 mice) and Mural-Zfp423<sup>KO</sup> (pooled from 4 mice) animals maintained for 8 days in growth media. No overt difference in the degree of spontaneous adipogenesis is observed. **c**, mRNA levels of key regulators of adipogenesis (*Cebpa* and *Pparg2*) in freshly isolated FIPs and APCs from gonadal WAT of control (n=10) and Mural-Zfp423<sup>KO</sup> (n=9) mice after 1-month HFD feeding. Bars represent mean  $\pm$  s.e.m., \* denotes p<0.05, \*\*\* denotes p<0.001 by one-way ANOVA. **d**, Average adipocyte size within gonadal WAT sections of control (n=11) and Mural-Zfp423<sup>KO</sup> (n=8) mice after 5-month Dox-HFD feeding. **e**, mRNA levels of adipocyte-selective genes and fibrogenic genes in whole gonadal WAT of control (n=9) and Mural-Zfp423<sup>KO</sup> (n=8) mice after 5-month Dox-HFD feeding. **f**, MuralChaser-Zfp423<sup>KO</sup> (*Pdgfrb*<sup>rtTA</sup>; *TRE-Cre*; *Zfp423*<sup>loxP/loxP</sup>; *Rosa26R*<sup>mT/mG</sup>) mice were generated by reconstituting the *Rosa26R*<sup>mT/mG</sup> allele into the Mural-Zfp423<sup>KO</sup> background. The addition of doxycycline results in inactivation of *Zfp423* and indelible labeling of *Pdgfrb*-expressing cells with mGFP expression. **g**, Representative 63x magnification confocal immunofluorescence images of gonadal WAT sections from MuralChaser (*Pdgfrb*<sup>rtTA</sup>; *TRE-Cre*; *Rosa26R*<sup>mT/mG</sup>) and MuralChaser-Zfp423<sup>KO</sup> mice after HFD feeding. 8 weeks-old animals were administered doxycycline-containing chow diet for 7 days and then switched to HFD feed (without doxycycline) for another 8 weeks. Sections were stained with anti-PERILIPIN (PERILIPIN; red) and anti-GFP (green) antibodies and counterstained with DAPI (blue; nuclei). Composite images were generated by digital overlay. **h**, Quantification of *de novo* adipogenesis: the frequency of GFP+ PERILIPIN+ cells observed by immunostaining was quantified by assaying ~3000-4000 adipocytes total from 5 mice per genotype. Bars represent mean  $\pm$  s.e.m. Exact p values and numbers of repetitions can be found in Source Data Extended Data Figure 7.



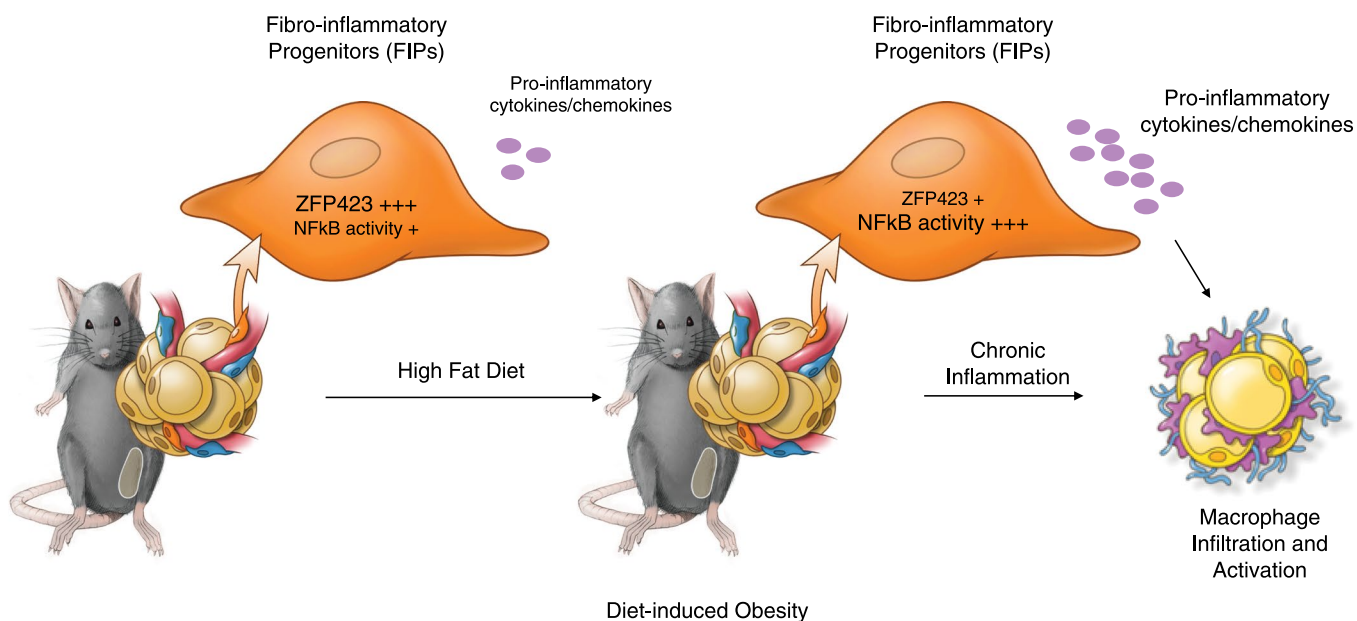
Extended Data Fig. 8 | See next page for caption.

**Extended Data Fig. 8 | Systemic consequences of inactivating mural cell *Zfp423* in obese mice housed at thermoneutrality.** **a**, Western blot of phosphorylated AKT (pAKT), total AKT, and  $\beta$ -actin protein expression in tissue extracts of gonadal WAT from Control (n=3) and Mural-*Zfp423*<sup>KO</sup> (n=3) mice after 5-month HFD feeding. Tissues were collected before (- insulin) and after insulin stimulation (+ insulin) of anesthetized animals. **b**, Intraperitoneal glucose tolerance tests (GTT) of thermoneutral-housed Control (n=12) and Mural-*Zfp423*<sup>KO</sup> (n=16) mice after HFD feeding. \* denotes  $p < 0.05$ , \*\* denotes  $p < 0.01$  by unpaired two-tailed Student's *t*-test. **c**, Intraperitoneal insulin tolerance tests (ITT) of thermoneutral-housed Control (n=8) and Mural-*Zfp423*<sup>KO</sup> (n=14) mice after HFD feeding. \* denotes  $p < 0.05$  by unpaired two-tailed Student's *t*-test. **d**, Serum levels of ADIPONECTIN (left) and INSULIN (six-hour fasting) (right) in Control and Mural-*Zfp423*<sup>KO</sup> mice maintained on doxycycline-containing chow diet or doxycycline-containing HFD for 1 month or 5 months. For control, n=5 of chow, n=8 of 1-month HFD, n=8 of 5-month HFD; for Mural-*Zfp423*<sup>KO</sup>, n=6 of chow, n=11 of 1-month HFD, n=9 of 5-month HFD. **e**, Serum levels of indicated pro-inflammatory cytokines in Control (n=8) and Mural-*Zfp423*<sup>KO</sup> (n=8) mice maintained on doxycycline-containing HFD for 5 months. **f**, mRNA levels of pro-inflammatory genes in skeletal muscle of Control (n=8) and Mural-*Zfp423*<sup>KO</sup> (n=6) mice after 5-months HFD feeding. **g**, mRNA levels of pro-inflammatory genes in livers of Control (n=8) and Mural-*Zfp423*<sup>KO</sup> (n=9) mice after 5-months HFD feeding. **h-j**, Levels of total monocytes and pro-inflammatory monocytes (LY6C+) in blood (**h**), bone marrow (**i**), and spleen (**j**) of Control (n=6) and Mural-*Zfp423*<sup>KO</sup> (n=7) mice after 5 months of HFD feeding. Bars represent mean  $\pm$  s.e.m. \* denotes  $p < 0.05$  by unpaired two-tailed Student's *t*-test (**d**, **e**, **g**). Exact p values, numbers of repetitions, and uncropped western blots can be found in Source Data Extended Data Figure 8.



Extended Data Fig. 9 | See next page for caption.

**Extended Data Fig. 9 | Modulating *Zfp423* expression impacts the activation of NF $\kappa$ B signaling in FIPs.** **a**, Mural-*Ikk2*<sup>CA</sup>/*Zfp423*<sup>TG</sup> (*Pdgfrb*<sup>flTA</sup>; *TRE-Cre*; *TRE-Zfp423*; *Rosa26R*<sup>lkk2CA</sup>) mice were generated by breeding the *Rosa26R*<sup>lkk2CA</sup> allele into the Mural-*Zfp423*<sup>TG</sup> background. The addition of doxycycline (Dox) leads to overexpression of *Zfp423* and simultaneous activation of constitutively active (CA) IKK2 in *Pdgfrb*-expressing cells. **b**, mRNA levels of *Zfp423* in cultured FIPs from Control (n=4), Mural-*Ikk2*<sup>CA</sup> (n=4), and Mural-*Ikk2*<sup>CA</sup>/*Zfp423*<sup>TG</sup> (n=4) mice following exposure to doxycycline (1  $\mu$ g/ml) *in vitro* for 1 day. **c**, mRNA levels of indicated pro-inflammatory genes in cultured FIPs from Control (n=4), Mural-*Ikk2*<sup>CA</sup> (n=4), and Mural-*Ikk2*<sup>CA</sup>/*Zfp423*<sup>TG</sup> (n=4) mice following exposure to doxycycline (1  $\mu$ g/ml) *in vitro* for 1 day. **d**, Mural-*Ikk2*<sup>CA</sup>/*Zfp423*<sup>KO</sup> (*Pdgfrb*<sup>flTA</sup>; *TRE-Cre*; *Zfp423*<sup>loxP/loxP</sup>; *Rosa26R*<sup>lkk2CA</sup>) mice were generated by breeding the *Rosa26R*<sup>lkk2CA</sup> allele into the Mural-*Zfp423*<sup>KO</sup> background. The addition of doxycycline (Dox) leads to inactivation of *Zfp423* and simultaneous activation of constitutively-active (CA) IKK2 in *Pdgfrb*-expressing cells. **e**, mRNA levels of *Zfp423* in cultured FIPs from Control (n=4), Mural-*Ikk2*<sup>CA</sup> (n=4), and Mural-*Ikk2*<sup>CA</sup>/*Zfp423*<sup>KO</sup> (n=4) mice following exposure to doxycycline (1  $\mu$ g/ml) *in vitro* for 1 day. **f**, mRNA levels of indicated pro-inflammatory genes in cultured FIPs from Control (n=4), Mural-*Ikk2*<sup>CA</sup> (n=4), and Mural-*Ikk2*<sup>CA</sup>/*Zfp423*<sup>KO</sup> (n=4) mice following exposure to doxycycline (1  $\mu$ g/ml) *in vitro* for 1 day. Experiments in this figure were independently repeated three times. Data in this figure are shown as the mean  $\pm$  s.e.m., \**p*<0.05 or \*\*\**p*<0.001 by one-way ANOVA. Exact *p* values can be found in Source Data Extended Data Figure 9.



**Extended Data Fig. 10 | Proposed Model: PDGFR $\beta$ + perivascular cells regulate WAT macrophage accumulation in obesity.** FIPs are a subpopulation of PDGFR $\beta$ + perivascular cells that are capable of exerting a pro-inflammatory phenotype. In lean (chow-fed) mice, the expression of ZFP423 in FIPs serves to moderate the activation of NF $\kappa$ B signaling and adipose tissue inflammation, through a molecular mechanism depicted in Fig. 8g. In response to high fat diet feeding, *Zfp423* expression is reduced, facilitating the activation of NF $\kappa$ B signaling in FIPs and the production of pro-inflammatory cytokines/chemokines required to drive the chronic macrophage accumulation and activation that occurs during prolonged high fat diet feeding.

## Reporting Summary

Nature Research wishes to improve the reproducibility of the work that we publish. This form provides structure for consistency and transparency in reporting. For further information on Nature Research policies, see [Authors & Referees](#) and the [Editorial Policy Checklist](#).

### Statistics

For all statistical analyses, confirm that the following items are present in the figure legend, table legend, main text, or Methods section.

n/a Confirmed

- The exact sample size ( $n$ ) for each experimental group/condition, given as a discrete number and unit of measurement
- A statement on whether measurements were taken from distinct samples or whether the same sample was measured repeatedly
- The statistical test(s) used AND whether they are one- or two-sided  
*Only common tests should be described solely by name; describe more complex techniques in the Methods section.*
- A description of all covariates tested
- A description of any assumptions or corrections, such as tests of normality and adjustment for multiple comparisons
- A full description of the statistical parameters including central tendency (e.g. means) or other basic estimates (e.g. regression coefficient) AND variation (e.g. standard deviation) or associated estimates of uncertainty (e.g. confidence intervals)
- For null hypothesis testing, the test statistic (e.g.  $F$ ,  $t$ ,  $r$ ) with confidence intervals, effect sizes, degrees of freedom and  $P$  value noted  
*Give  $P$  values as exact values whenever suitable.*
- For Bayesian analysis, information on the choice of priors and Markov chain Monte Carlo settings
- For hierarchical and complex designs, identification of the appropriate level for tests and full reporting of outcomes
- Estimates of effect sizes (e.g. Cohen's  $d$ , Pearson's  $r$ ), indicating how they were calculated

*Our web collection on [statistics for biologists](#) contains articles on many of the points above.*

### Software and code

Policy information about [availability of computer code](#)

#### Data collection

The cell sorting was performed by BD Biosciences FACSaria cytometer and the data were analyzed by FlowJo Version 10.6.1; The flow cytometry analysis were performed by BD Biosciences LSR Fortessa and the data were analyzed by FlowJo Version 10.6.1; The mass spectrum was performed by Orbitrap Fusion Lumos Mass Spectrometer (Thermo Electron); Ultimate 3000 RSLC-Nano liquid chromatography (Dionex); Concentrations of RNA and chromatin DNA were determined by Nanodrop 2000 (ThermoFisher). ChIP-sequencing reads and RNA-sequencing reads were generated at Illumina NextSeq 500 Mid Output platform;

#### Data analysis

FlowJo Version 10.6.1  
GraphPad Prism 8.0  
Homer Version 4.9  
deepTools version 2.5.0  
MACS version 2.1.0  
BEDTools version 2.26.0  
Sambamba version 0.6.6  
Samtools version 1.3  
BWA version 0.7.12  
GREAT (<http://great.stanford.edu/public/html/>)  
Proteome Discoverer version 2.2

For manuscripts utilizing custom algorithms or software that are central to the research but not yet described in published literature, software must be made available to editors/reviewers. We strongly encourage code deposition in a community repository (e.g. GitHub). See the Nature Research [guidelines for submitting code & software](#) for further information.

## Data

Policy information about [availability of data](#)

All manuscripts must include a [data availability statement](#). This statement should provide the following information, where applicable:

- Accession codes, unique identifiers, or web links for publicly available datasets
- A list of figures that have associated raw data
- A description of any restrictions on data availability

All animal models and reagents are freely available to investigators upon reasonable request. ChIP-seq data have been deposited to Gene Expression Omnibus (GEO Accession GSE134868). Mass spectrometry data has been deposited to MAAssIVE.

## Field-specific reporting

Please select the one below that is the best fit for your research. If you are not sure, read the appropriate sections before making your selection.

- Life sciences       Behavioural & social sciences       Ecological, evolutionary & environmental sciences

For a reference copy of the document with all sections, see [nature.com/documents/nr-reporting-summary-flat.pdf](https://www.nature.com/documents/nr-reporting-summary-flat.pdf)

## Life sciences study design

All studies must disclose on these points even when the disclosure is negative.

Sample size	Samples sizes were determined based on previous experience, literature standards, and pilot data. Additional details regarding sample size can be found in Source Data associated with each figure.
Data exclusions	No samples were excluded in this study.
Replication	Each experiment presented was independently reproduced > or = 2 times. Additional details regarding replication and sample size can be found Source Data associated with each figure
Randomization	No randomization was applied.
Blinding	RNA-seq, ChIP-seq and proteomics analysis were performed in a blinded fashion.

## Reporting for specific materials, systems and methods

We require information from authors about some types of materials, experimental systems and methods used in many studies. Here, indicate whether each material, system or method listed is relevant to your study. If you are not sure if a list item applies to your research, read the appropriate section before selecting a response.

### Materials & experimental systems

n/a	Involved in the study
<input type="checkbox"/>	<input checked="" type="checkbox"/> Antibodies
<input type="checkbox"/>	<input checked="" type="checkbox"/> Eukaryotic cell lines
<input checked="" type="checkbox"/>	<input type="checkbox"/> Palaeontology
<input type="checkbox"/>	<input checked="" type="checkbox"/> Animals and other organisms
<input checked="" type="checkbox"/>	<input type="checkbox"/> Human research participants
<input checked="" type="checkbox"/>	<input type="checkbox"/> Clinical data

### Methods

n/a	Involved in the study
<input type="checkbox"/>	<input checked="" type="checkbox"/> ChIP-seq
<input type="checkbox"/>	<input checked="" type="checkbox"/> Flow cytometry
<input checked="" type="checkbox"/>	<input type="checkbox"/> MRI-based neuroimaging

## Antibodies

Antibodies used

CD45-PerCP/Cyanine5.5; 1:400 for flow; Biolegend, clone 30-F11, #103132;  
 CD11b-Pacific Blue, 1:200 for flow, Biolegend, clone M1/70, #101224 ;  
 F4/80-PE, 1:200 for flow, Biolegend, clone BM8, #123110 ;  
 CD11c-APC, 1:200 for flow, Biolegend, clone N418, #117310 ;  
 CD206-FITC, 1:200 for flow, Biolegend, clone C068C2, #1471704;  
 CD45-PerCP/Cyanine5.5, 1:400 for flow, Biolegend, clone 30-F11, #103132;  
 CD31-PerCP/Cyanine 5.5,1:400 for flow, Biolegend, clone 390, #102420;  
 PDGFRb-PE, 1:75 for flow, Biolegend, clone APB5, #136006;  
 LY6C-APC, 1:400 for flow, Biolegend, clone HK1.4, #128016;  
 CD9-FITC, 1:400 for flow, Biolegend, clone MZ3, #124808;  
 CD68-APC, 1:200 for flow, Biolegend, clone FA-11, #137007;  
 CD68-FITC, 1:200 for flow, Biolegend, clone FA-11, #137005;

CD115-APC/Cy7, 1:200 for flow, Biolegend, clone AFS98, #135531;  
 anti-phospho-AKT, 1:1000 for WB, Cell Signaling Technology, #9271;  
 anti-AKT, 1:1000 for WB, Cell Signaling Technology, #2920;  
 anti-b-actin 1:5000 for WB, Sigma, #A1978;  
 anti-FLAG, 1:1000 for WB, Sigma, #F1804;  
 anti-p300, 1:1000 for WB, Cell Signaling Technology, #70088;  
 anti-Ac-p65, 1:1000 for WB, Cell Signaling Technology, #30455;  
 anti-p65, 1:1000 for WB, 1:100 for ChIP, Cell Signaling Technology, #8242;  
 anti-CHD4, 1:1000 for WB, 1:100 for ChIP, Cell Signaling Technology, #12011;  
 anti-MTA1, 1:1000 for WB, Cell Signaling Technology, #5647;  
 anti-HDAC1, 1:1000 for WB, Cell Signaling Technology, #5356;  
 anti-IkBa, 1:1000 for WB, Cell Signaling Technology, #4814;  
 anti-a-tubulin, 1:2000 for WB, Cell Signaling Technology, #3873;  
 guinea pig anti-PERILIPIN, 1:1000 for IFC, Fitzgerald #20R727  
 rabbit anti-MAC-2, 1:500 for IFC, Cedarlane, Clone M3/38, #CL8942AP;  
 chicken anti-GFP, 1:500 for IFC, Abcam, #ab13970;  
 goat anti-guinea pig Alexa flour 647, 1:200 for IFC, Invitrogen, #A21450;  
 goat anti-rat Alexa flour 488, 1:200 for IFC, Invitrogen, #A11006;  
 goat anti-chicken Alexa flour 488, 1:200 for IFC, Invitrogen, #A11039.

## Validation

All primary antibodies are commercially available and validated by the manufacturer.  
 CD45-PerCP/Cyanine5.5 was validated for flow cytometry in mouse splenocytes. (<https://www.biolegend.com/en-us/products/percp-cyanine5-5-anti-mouse-cd45-antibody-4264>)  
 CD11b-Pacific Blue was validated for flow cytometry in mouse bone marrow cells. (<https://www.biolegend.com/en-us/products/pacific-blue-anti-mouse-human-cd11b-antibody-3863>)  
 F4/80-PE was validated for flow cytometry in mouse peritoneal macrophages (<https://www.biolegend.com/en-us/products/pe-anti-mouse-f4-80-antibody-4068>);  
 CD11c-APC was validated for flow cytometry in mouse splenocytes (<https://www.biolegend.com/en-us/products/apc-anti-mouse-cd11c-antibody-1813>);  
 CD206-FITC was validated for flow cytometry in mouse peritoneal macrophages (<https://www.biolegend.com/en-us/products/fitc-anti-mouse-cd206-mmr-antibody-7318>);  
 CD31-PerCP/Cyanine 5.5 was validated for flow cytometry in mouse splenocytes (<https://www.biolegend.com/en-us/products/percp-cyanine5-5-anti-mouse-cd31-antibody-6668>);  
 PDGFRb-PE was validated for flow cytometry in mouse cell line NIH-3T3 (<https://www.biolegend.com/en-us/products/pe-anti-mouse-cd140b-antibody-6256>);  
 LY6C-APC was validated for flow cytometry in mouse bone marrow cells (<https://www.biolegend.com/en-us/products/apc-anti-mouse-ly-6c-antibody-6047>);  
 CD9-FITC was validated for flow cytometry in mouse bone marrow cells (<https://www.biolegend.com/en-us/products/fitc-anti-mouse-cd9-antibody-5565>);  
 CD68-APC was validated for flow cytometry in mouse peritoneal macrophages (<https://www.biolegend.com/en-us/products/apc-anti-mouse-cd68-antibody-6600>);  
 CD68-FITC was validated for flow cytometry in mouse peritoneal macrophages (<https://www.biolegend.com/en-us/products/fitc-anti-mouse-cd68-antibody-6599>);  
 CD115-APC/Cy7 was validated for flow cytometry in mouse peritoneal macrophages (<https://www.biolegend.com/en-us/products/apc-cyanine7-anti-mouse-cd115-csf-1r-antibody-13759>);  
 guinea pig anti-PERILIPIN was validated for IFC in mouse adipose tissue (<https://www.ncbi.nlm.nih.gov/pmc/articles/PMC4749445/>);  
 rabbit anti-MAC-2 was validated for IFC in mouse adipose tissue (<https://www.nature.com/articles/s41467-018-03196-x>);  
 chicken anti-GFP was validated for IFC in mouse adipose tissue (<https://www.ncbi.nlm.nih.gov/pmc/articles/PMC4749445/>);  
 anti-phospho-AKT was validated for WB in mouse cell line NIH/3T3 (<https://www.cellsignal.com/products/primary-antibodies/phospho-akt-ser473-antibody/9271>);  
 anti-AKT was validated for WB in mouse cell line NIH/3T3 (<https://www.cellsignal.com/products/primary-antibodies/akt-pan-40d4-mouse-mab/2920>);  
 anti-b-actin was validated for WB in various mouse cell lines (<https://www.sigmaaldrich.com/catalog/product/sigma/a1978?lang=en&region=US>);  
 anti-FLAG was validated for WB in various mouse cell lines (<https://pubmed.ncbi.nlm.nih.gov/31318316/>);  
 anti-p300 was validated for WB in various mouse cell lines ([https://www.cellsignal.com/products/primary-antibodies/p300-d1m7c-rabbit-mab/70088?site-search-type=Products&N=4294956287&Ntt=70088%3B&fromPage=plp&\\_requestid=430404](https://www.cellsignal.com/products/primary-antibodies/p300-d1m7c-rabbit-mab/70088?site-search-type=Products&N=4294956287&Ntt=70088%3B&fromPage=plp&_requestid=430404));  
 anti-Ac-p65 was validated for WB in mouse tissue (<https://pubmed.ncbi.nlm.nih.gov/27500833/>);  
 anti-p65 was validated for WB in mouse cell lines (<https://www.cellsignal.com/products/primary-antibodies/chd4-d4b7-rabbit-mab/12011>); was validated for ChIP in mouse tissue (<https://pubmed.ncbi.nlm.nih.gov/31807705/>);  
 anti-CHD4 was validated for WB in various mouse cell lines (<https://www.cellsignal.com/products/primary-antibodies/nf-kb-p65-d14e12-xp-rabbit-mab/8242>); was validated for ChIP in mouse cells (<https://pubmed.ncbi.nlm.nih.gov/32433961/>);  
 anti-MTA1 was validated for WB in mouse cells (<https://pubmed.ncbi.nlm.nih.gov/26943043/>);  
 anti-HDAC1 was validated for WB in mouse cell line NIH-3T3 ([https://www.cellsignal.com/products/primary-antibodies/hdac1-10e2-mouse-mab/5356?site-search-type=Products&N=4294956287&Ntt=%235356&fromPage=plp&\\_requestid=533292](https://www.cellsignal.com/products/primary-antibodies/hdac1-10e2-mouse-mab/5356?site-search-type=Products&N=4294956287&Ntt=%235356&fromPage=plp&_requestid=533292));  
 anti-IkBa was validated for WB in various mouse cell lines <https://www.cellsignal.com/products/primary-antibodies/ikba-l35a5-mouse-mab-amino-terminal-antigen/4814>;  
 anti-a-Tubulin was validated for WB in various mouse cells (<https://pubmed.ncbi.nlm.nih.gov/31969567/>);  
 goat anti-guinea pig Alexa flour 647 was validated for IF in mouse tissues (<https://www.thermofisher.com/antibody/product/Goat-anti-Guinea-Pig-IgG-H-L-Highly-Cross-Adsorbed-Secondary-Antibody-Polyclonal/A-21450>);  
 goat anti-rat Alexa flour 488 was validated for IF in mouse tissues (<https://www.thermofisher.com/antibody/product/Goat-anti-Rat-IgG-H-L-Cross-Adsorbed-Secondary-Antibody-Polyclonal/A-11006>);  
 goat anti-chicken Alexa flour 488 was validated for IF in mouse tissues (<https://www.thermofisher.com/antibody/product/Goat->

## Eukaryotic cell lines

Policy information about [cell lines](#)

Cell line source(s)	293/hTLR4A-MD2-CD14 cell; Phoenix cells.
Authentication	293/hTLR4A-MD2-CD14 cells were obtained from Invivogen (#293-htrl4md2cd14). Phoenix cell line was obtained from ATCC(#CRL-3213).
Mycoplasma contamination	Not tested
Commonly misidentified lines (See <a href="#">ICLAC</a> register)	None.

## Animals and other organisms

Policy information about [studies involving animals](#); [ARRIVE guidelines](#) recommended for reporting animal research

Laboratory animals	All mice used in this study were male on a C57BL/6J background. Mice ranging from 10-28 weeks age were used for all the experiments. The mice maintained on a 12hr light/dark cycle in a temperature-controlled environment (room temperature, 22°C; thermoneutrality, 30°C) with 40-60% humidity and given free access to water and food.
Wild animals	No wild animals included.
Field-collected samples	No field-collected samples included.
Ethics oversight	All animal experiments were performed according to procedures approved by the UTSW Institutional Animal Care and Use Committee.

Note that full information on the approval of the study protocol must also be provided in the manuscript.

## ChIP-seq

### Data deposition

- Confirm that both raw and final processed data have been deposited in a public database such as [GEO](#).
- Confirm that you have deposited or provided access to graph files (e.g. BED files) for the called peaks.

Data access links <i>May remain private before publication.</i>	ChIP-seq data have been deposited to Gene Expression Omnibus (GEO Accession GSE134868). <a href="https://www.ncbi.nlm.nih.gov/geo/query/acc.cgi?acc=GSE134868">https://www.ncbi.nlm.nih.gov/geo/query/acc.cgi?acc=GSE134868</a>
Files in database submission	FASTQ WT_input (GSM3974296) WT_p65 (GSM3974297) TG_input (GSM3974298) TG_p65 (GSM3974299) c1_chd4(GSM4566244) c1_input(GSM4566245) tg1_chd4(GSM4566246) tg1_input(GSM4566247)
Genome browser session (e.g. <a href="#">UCSC</a> )	UCSC

### Methodology

Replicates	8 samples were sequenced: p65 ChIP: p65 ChIP from control FIPs (WT_p65), 5% input DNA from control FIPs (WT_input), p65 ChIP from Mural-Zfp423TG FIPs (TG_p65), 5% input DNA from Mural-Zfp423TG FIPs (TG_input); CHD4 ChIP: CHD4 ChIP from control FIPs (c1_chd4), 5% input DNA from control FIPs (c1_input), CHD4 ChIP from Mural-Zfp423TG FIPs (tg1_chd4), 5% input DNA from Mural-Zfp423TG FIPs (tg1_input)
Sequencing depth	WT_input (GSM3974296) 55409738 reads, sequence length 76, single end WT_p65 (GSM3974297) 73499358 reads, sequence length 76, single end TG_input (GSM3974298) 66250941 reads, sequence length 76, single end TG_p65 (GSM3974299) 71918166 reads, sequence length 76, single end c1_chd4(GSM4566244) 42186418 reads, sequence length 76, single end

	c1_input(GSM4566245) 63516457 reads, sequence length 76, single end tg1_chd4(GSM4566246) 41542781 reads, sequence length 76, single end tg1_input(GSM4566247) 57746560 reads, sequence length 76, single end
Antibodies	anti-p65 antibody, Cell signalling technology, #8242; anti-CHD4 antibody, Abcam, #ab70469
Peak calling parameters	Relaxed peaks were called using MACS version 2.1.0 57 with a p-value of 1x10 <sup>-2</sup> . 5% input samples were used as peak calling controls. The Refseq genomic annotation of mm10 was downloaded from the UCSC genome browser and used as the reference of genome-wide TSSs.
Data quality	Library complexity was measured using BEDTools version 2.26.0 55 and meets ENCODE data quality standards. Number of peaks with fold change greater than 5 and qvalue (which is the adjusted pvalue) less than .05 are: C1_chd4 peaks: 22142 tg1_chd4 peaks: 35661 wt_p65 peaks: 3962 tg_p65 peaks: 29
Software	Homer Version 4.9 deepTools version 2.5.0 MACS version 2.1.0 BEDTools version 2.26.0 Sambamba version 0.6.6 Samtools version 1.3 BWA version 0.7.12

## Flow Cytometry

### Plots

Confirm that:

- The axis labels state the marker and fluorochrome used (e.g. CD4-FITC).
- The axis scales are clearly visible. Include numbers along axes only for bottom left plot of group (a 'group' is an analysis of identical markers).
- All plots are contour plots with outliers or pseudocolor plots.
- A numerical value for number of cells or percentage (with statistics) is provided.

### Methodology

Sample preparation	For sorting FIPs and APCs, minced gonadal white fat depots were incubated for 1 hr in digestion buffer (1xHank's Balanced Salted Solution, 1.5% bovine serum albumin and 1 mg/ml Collagenase D [Roche, #11088882001]) at 37°C within a shaking water bath. The digested mixture was sequentially filtered through a 100 µm cell strainer and then a 40 µm cell strainer. The red blood cells in SVFs were lysed by short incubation in 1 ml 1xRBC lysis buffer (eBioscience, #00-4300-54) and the SVF cells were then resuspended in blocking buffer (2% FBS/PBS containing anti-mouse CD16/CD32 Fc Block 1:200). For FACS isolation of FIPs and APCs, primary antibodies were added to the cells in blocking buffer for 15 min while incubating at 4°C. The cells were then washed once and resuspended in 2% FBS/PBS before sorting. FACS was performed using a BD Biosciences FACSAria cytometer at the Flow Cytometry Core Facility at UT Southwestern. For sorting circulating monocytes, leukocyte pools from the blood of 10-week-old Rosa26RmTmG mice were subjected to erythrocyte lysis prior to staining with flow antibodies. Then, CD45+CD11b+CD115+ circulating monocytes were sorted out by a BD Biosciences FACSAria cytometer at the Flow Cytometry Core Facility at UT Southwestern. For the analysis of adipose tissue macrophages, isolated SVF cells were incubated with flow antibodies for 1hr at 4°C. After one wash with 2% FBS/PBS, cells were fixed by incubation with BD Cytofix (BD Biosciences, #554655) for > 30 min. Flow cytometry analysis was performed using a BD Biosciences LSR Fortessa.
Instrument	BD Biosciences FACSAria cytometer for sorting; BD Biosciences LSR Fortessa for flow analysis.
Software	FlowJo (version 10.6.1)
Cell population abundance	All sorted populations were confirmed as highly pure by post-sorts (>95%)
Gating strategy	For sorting FIPs and APCs from the stromal vascular fraction of digested gonadal white adipose tissue. Upon selection of live cells/single cells from stromal vascular cells (pregated on FSC-A/SSC-A, FSC-A/FSC-H and SSC-A/SSC-H singlet gate), PDGFRb+ cells are separated from CD45+ (hematopoietic) and CD31+ (endothelial) lineage cells and then further subdivided on the basis of LY6C and CD9 expression. LY6C+ PDGFRb+ CD45- CD31- cells represent FIPs. LY6C- CD9- PDGFRb+ CD45- CD31- cells represent APCs. For sorting circulating monocytes, Upon selection of live cells/single cells from blood leukocyte pools, CD45+ cells were segregated on the basis of CD11b+ and CD115+ expression. For analyzing adipose tissue macrophages from the stromal vascular fraction of digested gonadal white adipose tissue. Upon selection of live cells/single cells from gonadal WAT stromal vascular fraction (pregated on FSC-A/SSC-A, FSC-A/FSC-H and SSC-A/SSC-H singlet gate), CD45+ cells were segregated on the basis of CD11b and F4/80 (or CD68) expression. Adipose tissue

macrophages, defined as CD11b+ F4/80+ cells, were then separated on the basis of CD11c and CD206, or CD9 expression. Pro-inflammatory macrophages were defined as CD11c+ CD206-, or CD9+.

Tick this box to confirm that a figure exemplifying the gating strategy is provided in the Supplementary Information.